ELSEVIER

CrossMark

Virtual Special Issue
CORE-II

An assessment of Antarctic Circumpolar Current and Southern Ocean meridional overturning circulation during 1958–2007 in a suite of interannual CORE-II simulations

Riccardo Farneti [a,*], Stephanie M. Downes [b], Stephen M. Griffies [c], Simon J. Marsland [d], Erik Behrens [e], Mats Bentsen [f], Daohua Bi [d], Arne Biastoch [e], Claus Böning [e], Alexandra Bozec [g], Vittorio M. Canuto [h], Eric Chassignet [g], Gokhan Danabasoglu [i], Sergey Danilov [j], Nikolay Diansky [k], Helge Drange [l], Pier Giuseppe Fogli [m], Anatoly Gusev [k], Robert W. Hallberg [c], Armando Howard [h,s], Mehmet Ilicak [f], Thomas Jung [j], Maxwell Kelley [h], William G. Large [i], Anthony Leboissetier [h,n], Matthew Long [i], Jianhua Lu [g], Simona Masina [m,o], Akhilesh Mishra [g], Antonio Navarra [m,o], A.J. George Nurser [p], Lavinia Patara [e], Bonita L. Samuels [c], Dmitry Sidorenko [j], Hiroyuki Tsujino [q], Petteri Uotila [d,r], Qiang Wang [j], Steve G. Yeager [i]

[a] International Centre for Theoretical Physics (ICTP), Trieste, Italy
[b] Research School of Earth Sciences and ARC Centre of Excellence for Climate System Science, Australian National University (ANU), ACT, Australia
[c] NOAA Geophysical Fluid Dynamics Laboratory (GFDL), Princeton, NJ, USA
[d] Centre for Australian Weather and Climate Research, a partnership between CSIRO and the Bureau of Meteorology, Aspendale, Australia
[e] GEOMAR Helmholtz Centre for Ocean Research Kiel, Germany
[f] Uni Research Ltd. Bergen, Norway
[g] Center for Ocean-Atmospheric Prediction Studies (COAPS), Florida State University, Tallahassee, USA
[h] NASA Goddard Institute for Space Studies (GISS), New York, NY, USA
[i] National Center for Atmospheric Research (NCAR), Boulder, CO, USA
[j] Alfred Wegener Institute (AWI), Helmholtz Centre for Polar and Marine Research, Bremerhaven, Germany
[k] Institute of Numerical Mathematics, Russian Academy of Sciences, Moscow, Russia
[l] University of Bergen, Bergen, Norway
[m] Centro Euro-Mediterraneo sui Cambiamenti Climatici (CMCC), Bologna, Italy
[n] Trinnovim LLC, New York, New York, USA
[o] Istituto Nazionale di Geofisica e Vulcanologia (INGV), Bologna, Italy
[p] National Oceanography Centre Southampton (NOCS), Southampton, UK
[q] Meteorological Research Institute (MRI), Japan Meteorological Agency, Tsukuba, Japan
[r] Finnish Meteorological Institute, Helsinki, Finland
[s] Medgar Evers College of CUNY, New York, NY, USA

A R T I C L E   I N F O

A B S T R A C T

In the framework of the second phase of the Coordinated Ocean-ice Reference Experiments (CORE-II), we present an analysis of the representation of the Antarctic Circumpolar Current (ACC) and Southern Ocean meridional overturning circulation (MOC) in a suite of seventeen global ocean–sea ice models. We focus on the mean, variability and trends of both the ACC and MOC over the 1958–2007 period, and discuss their relationship with the surface forcing. We aim to quantify the degree of eddy saturation and eddy compensation in the models participating in CORE-II, and compare our results with available observations, previous fine-resolution numerical studies and theoretical constraints. Most models show weak ACC transport sensitivity to changes in forcing during the past five decades, and they can be considered to be in an eddy saturated regime. Larger contrasts arise when considering MOC trends, with a majority of models exhibiting significant strengthening of the MOC during the late 20th and early 21st century. Only a few models show a relatively small sensitivity to forcing changes, responding with an intensified eddy-induced circulation that provides

* Corresponding author. Tel.: +390402240307.
  E-mail address: rfarneti@ictp.it (R. Farneti).

some degree of eddy compensation, while still showing considerable decadal trends. Both ACC and MOC interannual variabilities are largely controlled by the Southern Annular Mode (SAM). Based on these results, models are clustered into two groups. Models with constant or two-dimensional (horizontal) specification of the eddy-induced advection coefficient κ show larger ocean interior decadal trends, larger ACC transport decadal trends and no eddy compensation in the MOC. Eddy-permitting models or models with a three-dimensional time varying κ show smaller changes in isopycnal slopes and associated ACC trends, and partial eddy compensation. As previously argued, a constant in time or space κ is responsible for a poor representation of mesoscale eddy effects and cannot properly simulate the sensitivity of the ACC and MOC to changing surface forcing. Evidence is given for a larger sensitivity of the MOC as compared to the ACC transport, even when approaching eddy saturation. Future process studies designed for disentangling the role of momentum and buoyancy forcing in driving the ACC and MOC are proposed.

1. Introduction

The Southern Ocean's grip on past, present and future global climate has been long recognized (Toggweiler and Samuels, 1995; Russell et al., 2006; Watson and Naveira-Garabato, 2006; Toggweiler et al., 2006; Kuhlbrodt et al., 2007; Toggweiler and Russell, 2008; Marshall and Speer, 2012, to cite a few). The Southern Ocean has a primary influence on the evolution of the Earth's climate and ecosystems. In this region of strongly tilted isopycnals, intermediate, deep, and bottom waters upwell and interact with the atmosphere, exchanging physical and chemical properties (Rintoul and Naveira-Garabato, 2013). Thanks to the large regions of upper ocean water mass formation in the Southern Ocean, this region is responsible for about 40% of the oceanic uptake of anthropogenic carbon dioxide from the atmosphere, and accounts for about 70% of the excess heat that is transferred from the atmosphere into the ocean (Frölicher et al., 2015). The unblocked region circling Antarctica permits the development of the Antarctic Circumpolar Current (ACC), responsible for inter-basin exchanges and the development of a global meridional overturning circulation (MOC). The ACC and its zonal channel, blocking the transport of warm salty water of northern origins, isolate Antarctica and the ocean around it.

The meridional density gradient and associated tilted isopycnals that largely control the strength of the ACC also play an important role in the Southern Ocean branch of the global MOC, as southward flowing deep water upwells along the steeply sloped isopycnals associated with the ACC. In a simplified zonally-averaged framework, water sinking in the North Atlantic flows southward as North Atlantic deep water (NADW). Reaching Southern Ocean latitudes, some of the NADW transforms into upper circumpolar deep water (UCDW), which upwells nearly adiabatically along the slanted density surfaces within the ACC belt. Upon outcropping, air–sea buoyancy exchanges and diapycnal mixing converts UCDW into Antarctic Intermediate Water (AAIW) and SubAntarctic Mode Water (SAMW) that flows equatorward and closes the Upper Cell of the Southern Ocean overturning as its surface branch. Another portion of the poleward-flowing NADW is transformed into lower circumpolar deep water (LCDW) that, denser than UCDW, upwells further south close to the Antarctic coast. Here, cooling from air–sea fluxes and salinification from brine rejection transforms LCDW into AABW. AABW sinks and is exported equatorwards as the deep branch of the Lower Cell of the Southern Ocean overturning (Marshall and Speer, 2012; Rintoul and Naveira-Garabato, 2013; Sloyan and Rintoul, 2001; Speer et al., 2000). A schematic representing the Southern Ocean MOC in both depth- and density-space is given in Fig. 16 (to be discussed further in Section 4), where the main water masses are also shown.

Southern Ocean dynamics – and the focus here will be on the ACC transport and the upper branch of the MOC – is believed to be controlled to different extents by both momentum and buoyancy forcing (e.g. Gnanadesikan and Hallberg, 2000; Bryden and Cunningham, 2003; Marshall and Radko, 2003; Olbers et al., 2004; Marshall

and Radko, 2006; Hogg, 2010; Morrison et al., 2011; Rintoul and Naveira-Garabato, 2013). However, most of the attention so far, both from the theoretical and modeling community, has been devoted to the role of the wind stress, and especially on the effects of past and future changes (Abernathey et al., 2011; Allison et al., 2010; 2011; Farneti et al., 2010; Gent and Danabasoglu, 2011; Jones et al., 2011; Meredith and Hogg, 2006; Munday et al., 2013; Sijp and England, 2004; Toggweiler et al., 2006). The strong westerly winds that overlie the Southern Ocean play a major role in driving both the overturning circulation and the large horizontal transport of the ACC. These winds have strengthened in recent decades, at least partly due to anthropogenic processes (Marshall, 2003b; Thompson et al., 2011; Thompson and Solomon, 2002). Not only have the westerly winds increased their magnitude but they have also shifted polewards, inducing a significant reorganization of the large-scale circulation, modifying the position of the main fronts and subduction rates (Downes et al., 2011a).

Recently, the observationally based study of Böning et al. (2008) concluded that the ACC transport and associated isopycnal tilt have been largely unaffected by the poleward shift and intensification of the westerlies over the past few decades. The results from Böning et al. (2008), and previous modeling studies (Hallberg and Gnanadesikan, 2006; Meredith and Hogg, 2006), ignited a new line of research with fine and coarse resolution ocean models, emphasizing the primary role of mesoscale eddies in setting the Southern Ocean response to the changes in forcing (Farneti et al., 2010; Gent and Danabasoglu, 2011; Morrison and Hogg, 2013; Munday et al., 2013). In fact, the limited sensitivity of the ACC transport to wind perturbations is achieved through the response of the mesoscale eddy field. Strengthening winds increase the tilt of the isopycnals and the baroclinicity of the ACC, generating a store of available potential energy. The potential energy is then removed by baroclinic instability, spawning mesoscale eddies and increasing the eddy kinetic energy (EKE), resulting in a flattening of the isopycnals. The ACC transport is thus insensitive to decadal changes in winds (Meredith et al., 2012), which do not influence the mean transport but rather feed directly into the mesoscale circulation, and is said to be in the *eddy saturation* regime, as first discussed by Straub (1993).

An eddy saturated state, or equivalently a relatively small change in isopycnal tilt within the ACC, was originally also associated with an insensitivity of the MOC to forcing changes (Böning et al., 2008; Farneti et al., 2010). The Southern Ocean MOC is in fact a balance between a wind-driven circulation and an opposing eddy-induced transport. In the Southern Ocean, winds drive a northward Ekman flow generating an Eulerian-mean circulation and steepening of the isopycnals. Baroclinic instability is again responsible for generating eddies that push the isopycnals down, reducing their slope, and feeding an eddy-induced overturning that is thus opposing the wind-driven cell. This is the basis for the residual-mean theory applied to the Southern Ocean MOC (Andrews and McIntyre, 1976; Marshall and Radko, 2003; McIntosh and McDougall, 1996; Olbers et al., 2004).

Stronger winds imply an anomalous Eulerian-mean cell, and a larger isopycnal tilt favors the generation of eddies and the strengthening of the eddy-induced cell. The final state would be a balance between the two opposing circulations and the process regulating the strength of the total, or residual, MOC is called *eddy compensation* (Hallberg and Gnanadesikan, 2006). However, the extent to which eddies can compensate for changes in the wind-driven overturning is still not known. Evidence is building for partial eddy compensation even in the presence of total eddy saturation (Abernathey et al., 2011; Munday et al., 2013; Viebahn and Eden, 2010), as the two are governed by dynamical mechanisms occurring at different depths (Meredith et al., 2012; Morrison and Hogg, 2013).

Owing to fine-resolution Southern Ocean experiments, such as the seminal paper of Hallberg and Gnanadesikan (2006), several studies have assessed the response of different mesoscale eddy parameterizations to idealized changes in forcing and the fidelity of their numerical implementation in coarse-resolution models (Eden et al., 2009; Farneti and Gent, 2011; Gent and Danabasoglu, 2011; Hofmann and Maqueda, 2011; Kuhlbrodt et al., 2012). At the same time, several new ideas have been put forward on how to specify a closure for the effect of mesoscale eddies (Canuto and Dubovikov, 2006; Cessi, 2008; Eden and Greatbatch, 2008; Ferrari et al., 2010; Jansen and Held, 2014; Marshall and Adcroft, 2010).

We analyse here the representation of the ACC and Southern Ocean MOC Upper Cell as simulated by seventeen global ocean–sea ice models participating in the Coordinated Ocean–sea ice Reference Experiments phase II (CORE-II; Danabasoglu et al., 2014). We focus on the Upper Cell of the MOC for several reasons:

– For its climatic importance, as it is the Upper Cell that is mostly responsible for the Southern Ocean uptake of anthropogenic carbon dioxide from the atmosphere, the upwelling of fertilizing nutrients and the uptake of excess heat that is transferred from the atmosphere into the ocean which is currently slowing the rate of global warming (Marshall and Speer, 2012; Rintoul and Naveira-Garabato, 2013).
– Because the Upper Cell has received much theoretical attention in the last decades, also due to the reasons mentioned above, with the development of conceptual frameworks for the balance between wind, buoyancy and eddy forcing on setting the overturning circulation (Marshall and Radko, 2003; 2006; Olbers and Visbeck, 2005).
– Given the recognized importance of mesoscale eddies in setting the net upper branch of the Southern Ocean MOC, we test here the sensitivity of the parameterizations of unresolved fluxes, which have recently evolved and improved (Canuto and Dubovikov, 2006; Danabasoglu and Marshall, 2007; Eden and Greatbatch, 2008; Eden et al., 2009; Gent and Danabasoglu, 2011; Hofmann and Maqueda, 2011).

An aim of CORE-II studies is to define a benchmark for the capability of global ocean–sea ice models and present a comprehensive overview of ocean climate models with respect to observations, theoretical and modeling studies for several regions and topics. A few CORE-II papers have preceded this study (Danabasoglu et al., 2014; Griffies et al., 2014), and more will follow. In particular, the Southern Ocean has already been the subject of a CORE-II intercomparison analysis (Downes et al., 2015), where the attention was devoted to Southern Ocean water masses and sea ice evolution during 1988–2007.

The goal of this paper is to analyse the evolution of both the ACC transport and Southern Ocean MOC during the CORE-II period. We focus on the mean state and variability over the period 1958–2007 of the CORE-II simulations, and we compare solutions from fine and coarse-resolution models, where most models include different flavors of the parameterization for mesoscale eddies proposed by Gent and McWilliams (1990) and Gent et al. (1995).

A focus is given on the efficiency of mesoscale eddies, parameterized or permitted, in counteracting the observed forcing changes responsible for driving both the ACC and MOC. We quantify the degree of eddy saturation and eddy compensation in the models participating in CORE-II, and compare our results with available observations, previous fine-resolution numerical studies and theoretical constraints. Westerly winds overlying the Southern Ocean region have experienced changes over the past decades (Marshall, 2003b; Thompson and Solomon, 2002), and these trends are reflected in the CORE-II forcing. However, both the observed strengthening and latitudinal shift of winds remain much smaller than those used in previous modeling studies, where sensitivities were tested for very large anomalies (Abernathey et al., 2011; Farneti et al., 2010; Gent and Danabasoglu, 2011; Morrison and Hogg, 2013; Munday et al., 2013; Viebahn and Eden, 2010). We thus test here the response of ocean–sea ice models to observe realistic forcing changes responsible for driving both the ACC and Southern Ocean MOC during years 1958–2007.

After briefly introducing in Section 2 the models used and the CORE-II surface forcing, we divide the paper into two main parts: Section 3 is devoted to the eddy saturation of the ACC whereas Section 4 deals with the eddy compensation of the MOC. We summarize our results in Section 5 and conclude in Section 6. The definition and details for the computation of the MOC in depth and density space are given in Appendix A. Relevant characteristics of the ocean–sea ice models and details of their parameterization of eddy fluxes are given in Appendix B.

2. Ocean–sea ice models, CORE-II simulations and forcing

We present in this paper results from seventeen models, most of which have been described in Appendix A of Danabasoglu et al. (2014), and some of their basic properties are listed in Table 1. We include in our study three additional models not previously described in Danabasoglu et al. (2014): GFDL-MOM025 and KIEL025, which are finer-resolution versions of ocean models used in previous CORE-II studies (Danabasoglu et al., 2014; Griffies et al., 2014), and FSU2, a revised version of the HYCOM model. GFDL-MOM025 and KIEL025 models have a horizontal resolution of 1/4°, and derive from the GFDL-MOM and KIEL models, respectively. Adding two eddy-permitting models in a Southern Ocean intercomparison study is particularly useful, since the region of study is strongly affected by eddy dynamics in both its climatology and variability. Also, although not eddy-resolving, both models lack a parameterization of the eddy-induced advective transport. We do not expect eddy-permitting models to resolve all mesoscale activity and at all latitudes; however, they provide us with eddy fluxes naturally arising from the flow that can be compared with coarser models that include different flavors of parameterizations of the eddy-induced advective transport. More details are provided in Appendix B.

The model contributions also differ with respect to their vertical discretization from depth, to isopycnal, hybrid, mass and terrain following coordinate ocean models. In a region of the World Ocean such as the Southern Ocean where air–sea interactions, generation of dense bottom waters, isopycnal and diapycnal mixing and water mass transformation take place, the vertical representation of these processes is likely to be a key ingredient in the simulation of the mean state and variability.

The ocean models are forced with CORE-II atmospheric data sets from year 1948 to 2007 (Large and Yeager, 2009), and they are run for five repeating cycles of the 60-year forcing. Only the last cycle is analyzed as a hindcast simulation, with the previous 4 cycles regarded as a spin-up period and a useful record for the characterization of biases, drifts and stability of the oceanic properties and circulation. As discussed in both Danabasoglu et al. (2014) and Griffies et al. (2014), the atmospheric forcing goes from year 2007 back to 1948

Table 1

Summary of the ocean models. The table includes the participating group name, the ocean model name and its version, the vertical coordinate and number of layers/levels in parentheses, the horizontal resolution, the time scale of surface salinity restoring (given in days over a 50 m length scale), the eddy-induced advection coefficient (κ) with its value and space-time characteristics in parentheses, the along-isopycnal neutral diffusion coefficient (A_I) and the maximum neutral slope used for tapering off the neutral physics fluxes (S_{max}). Both κ and A_I are given in units of m^2 s^{-1}.

Group	Ocean model	Vertical	Horiz. res.	time scale	κ	A_I	S_{max}
1. ACCESS	MOM 4p1	z^* (50)	1°	150	(2D; time-dependent) $100 \leq \kappa \leq 600$	600	1/200[e]
2. AWI	FESOM	z (46)	1°	300	(3D; time-dependent) $50 \leq \kappa \leq 1500$	$=\kappa$	1/20
3. BERGEN	MICOM	ρ_2 (51)	1°	300	(3D; time-dependent) $100 \leq \kappa \leq 1500$	$=\kappa$	–
4. CMCC	NEMO 3.3	z (46)	1°	365	(2D; time-dependent) $0 \leq \kappa \leq 5000$	1000[d]	1/100
5. FSU	HYCOM 2.2.21	Hybrid (32)	1°	1460	(2D; fixed)[c] $0.05 \times \Delta^3$	$=\kappa$	–
6. FSU2	HYCOM 2.2.74	Hybrid (32)	0.72°	1460[a]	(2D; fixed)[c] $0.02 \times \Delta^3$	$=\kappa$	–
7. GFDL-GOLD	GOLD	ρ_2 (59)	1°	50	(2D; time-dependent) $10 \leq \kappa \leq 900$	$=\kappa$	–
8. GFDL-MOM	MOM 4p1	z^* (50)	1°	300	(2D; time-dependent) $100 \leq \kappa \leq 600$	600	1/200[e]
9. GFDL-MOM025	MOM 5	z^* (50)	0.25°	300	–	–	–
10. GISS	Model E2-R	Mass (32)	1°	1250	(3D; time-dependent) $\kappa \propto$ EKE(z)$^{1/2}$	$=\kappa$	–
11. ICTP	MOM 4p1	z^* (30)	2°	275[b]	(2D; time-dependent) $800 \leq \kappa \leq 1400$	800	1/200[e]
12. INMOM	INMOM	Terrain-following (40)	1° × 0.5°	365	0	100	8/1000
13. KIEL	NEMO 3.1.1	z (46)	0.5°	1500[b]	(2D; time-dependent) $0 \leq \kappa \leq 1000$	600[d]	1/100
14. KIEL025	NEMO 3.4.1	z (46)	0.25°	300[b]	–	300[d]	1/100
15. MRI	MRI.COM 3	z (50)	1° × 0.5°	365	(1D; fixed) $100 \leq \kappa \leq 235$	1000	1/1000
16. NCAR	POP 2	z (60)	1°	1450	(3D; time-dependent) $300 \leq \kappa \leq 3000$	$=\kappa$	3/10
17. NOCS	NEMO 3.4	z (75)	1°	300	(2D; time-dependent) $0 \leq \kappa \leq 5000$	1000[d]	1/100

[a] In FSU2, surface salinity restoring in the Southern Ocean has a piston velocity of 6 months.

[b] Models not restoring under sea-ice.

[c] In FSU and FSU2, interface height smoothing, corresponding to Gent and McWilliams (1990), has a mixing coefficient determined by the grid spacing Δ (in m) times a constant velocity scale in m s^{-1}.

[d] In CMCC, KIEL, KIEL025 and NOCS, neutral diffusivity is scaled according to the grid spacing, with 1000, 600, 300 and 1000 m^2 s^{-1} the value at the Equator, respectively, and decreasing with latitude.

[e] ACCESS, GFDL-MOM and ICTP have S_{max} only applied to neutral diffusion. The eddy advective transport uses the Ferrari et al. (2010) streamfunction that has no S_{max}.

at the end of each cycle, generating an inconsistency between the forcing and the oceanic state. Because of this jump, solutions from the first few years of any forcing cycle should not be used in any analysis as they are affected by the forcing transition from 2007 back to 1948. This unavoidable deficiency of the CORE protocol is partially alleviated here by ignoring the first decade in the analysis of mean states and trends. Hence, we will be computing time-means and trends over the five decades corresponding to the period 1958–2007, unless otherwise stated.

Air–sea fluxes in ocean-ice models are determined by prescribed non-interactive atmosphere states. Related to this approach is the need to introduce an ad hoc surface salinity restoring. Sea surface salinity (SSS) restoring is used by all contributing models in order to avoid spurious drifts (for a comprehensive description on salinity restoring in CORE-II simulations see Appendix B and C in Danabasoglu et al., 2014). The SSS restoring time scale differs for each model and depends on the physical and numerical nature of the ocean model. In contrast, there is no restoring applied to sea surface temperature (SST). The sensitivity of the ocean integrations to the choice of salinity restoring was already presented in Griffies et al. (2009), where the magnitude of transport and stability for different indices was shown to be highly dependent on the chosen time scale. Danabasoglu et al. (2014) reinforce the point showing the dependency of the strength of the Atlantic meridional overturning circulation (AMOC) upon the strength of the SSS restoring time scale. Of course, the same argument is valid for the strength and stability of the ACC transport. Surface restoring is thus chosen by each modeling group in order to generate a reasonably stable ACC with a transport within observational values. A *too strong* restoring usually weakens the ACC baroclinic transport that, through geostrophy, is tied to the density field of the upper Southern Ocean. A *too weak* restoring usually increases the ACC transport at the expense of a possible drift in the temperature-salinity properties and of the ACC transport itself (see for example Griffies et al., 2009). Hence, the value used by the models for the SSS restoring time scale (given in Table 1) is to be regarded as an ad hoc solution without physical basis. However, we will show that there is no correlation between restoring time scales and trends in ACC transport and MOC, so that the value chosen for SSS restoring time scale by each model is not impacting our results.

2.1. The surface forcing

As described in Danabasoglu et al. (2014), wind stress is not directly applied to force the models. Instead, wind speed, corrected from National Center for Environmental Prediction (NCEP) reanalysis data (see Section 3.1 of Large and Yeager, 2009), are passed to the ocean–sea ice models, which convert the forcing to wind stress by using common bulk formulae and the simulated ocean surface currents (for a comprehensive description see Large and Yeager, 2009). As a result the computed wind stress, being also impacted by sea-ice cover, is not exactly the same for each model, although variations are usually minor in a large-scale sense.

The multi model mean (MMM) evolution of zonal-mean zonal wind stress over the Southern Ocean, as computed by the CORE-II simulations used in this study, is shown in Fig. 1. An intensification and poleward shift of the westerlies is evident throughout the 60-year period. The white line in Fig. 1 represents the latitudinal position of the peak zonal wind stress, highlighting the shift towards higher latitudes. We also note that both strength and position seem to have stabilized in the final 10–15 years of the observational record. The evolution of the magnitude of peak zonal wind stress, which is certainly a crude index for the overall westerlies, is shown in Fig. 2a, where values go from 0.125 N/m^2 during the second decade (1958–1967) to 0.16 N/m^2 during the last decade (1998–2007). Peak wind stress has indeed strengthened within the CORE-II interannual forcing period, with an averaged strengthening of ~30% between the last and second decade (Fig. 2b). As previously noted, winds have also shifted polewards, and this is reflected in Fig. 2c, where the latitude of peak wind stress is shown to shift southward by ~2° between the last and second decade. Both the monotonic increase in magnitude and southward shift in latitude appear to be sustained in the first 40–50 years, whereas from the mid-1990s there seems to be a stabilization of the westerlies, or at least a reduction in the rate of strengthening.

There is also a large component of interannual variability in addition to long-term trends. Wind changes in the Southern Hemisphere are well represented by the Southern Annular Mode (SAM), which is the principal mode of variability of the extratropical atmospheric circulation. The SAM is computed as the difference in normalized zonal mean sea level pressure at 40 °S and 65 °S (Marshall, 2003a). The mode has a zonally symmetric or annular structure, with syn-
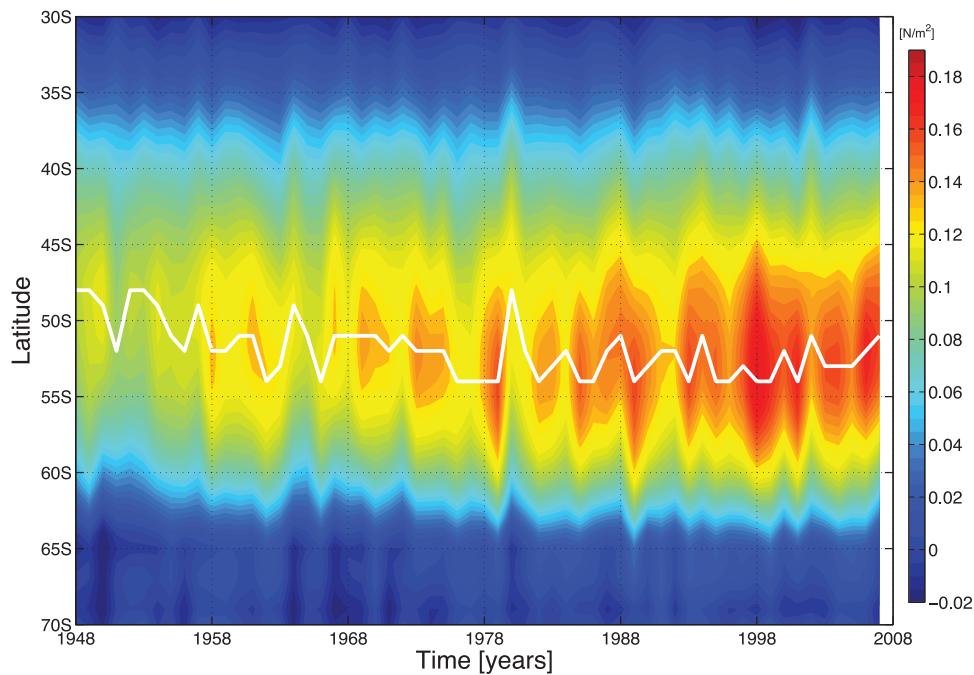
Fig. 1. Time series of the multi model mean (MMM) zonal-mean zonal wind stress (in N m^{-2}). Shown here are Southern Ocean latitudes (30°S to 70°S) for the entire 60-year period. The white line represents the latitude of the peak zonal wind stress .

chronous anomalies of opposite signs in Antarctica and the midlat-itudes, and is considered to be the most significant forcing of intraseasonal to decadal climate variability in the Southern Hemisphere (Visbeck, 2009). Over the past 60 years, a clear upward trend in the SAM index has been observed, and is well represented in the CORE-II forcings (see Fig. 14 and discussions in Section 3.3 and 4.4). The SAM tendency towards a positive phase, with pressures over Antarctica relatively low compared to those in the midlatitudes, has been sustained until the 1990s, when the trend seems to have diminished, with the index remaining in a positive state. Hence, although winds have been shown to strengthen and shift polewards across the entire Southern Ocean over the last 60 years, the trend has weakened considerably from the 1990s onwards.

Due to the paucity of station data, significant uncertainties exist in NCEP reanalysis data south of 30 °S. In particular, trends in the SAM in the last decades have been shown to be partly spurious when compared to station data (Marshall, 2003a; Visbeck, 2009), and trends in the SAM index computed through sea level pressure data reveal significant errors, especially when comparing periods before and after the advent of satellite measurements, which is roughly straddling the CORE-II 60-year period. However, the magnitude and direction of NCEP vector winds have undergone a correction or adjustment in CORE data sets based on comparison with observations, mainly in the form of satellite products (Large and Yeager, 2009). The wind adjustments improve the agreement with ship and satellite based climatologies, result in a better balanced global heat and freshwater budgets, and produce more realistic oceanic heat and freshwater transports compared to non-adjusted NCEP winds (see also Cerovecki et al., 2011).

The time mean (of the full record 1948–2007) zonal-mean zonal wind stress, as computed by the models, is shown in Fig. 3a. Most models agree on the magnitude and latitudinal distribution of the wind stress, with some significant differences. The peak zonal wind stress, between 50 ° and 55 °S, shows a spread among models. Not all models use the same bulk formulae, and differences are also due to the ocean interaction (i.e., ocean surface currents) with NCEP winds. Perhaps more prominent is the spread in easterly wind stresses (south of 65 °S), which is believed to be the result of sea-ice influenc-

ing the position and strength of surface fluxes in that region (Downes et al., 2015).

The INMOM simulation is an outlier, with a much larger westerly wind stress (Fig. 3a). Differences between INMOM wind stresses and the CORE-II ensemble are ubiquitous, with the largest discrepancies in tropical regions and the Southern Ocean. Indeed, INMOM has used a different bulk formula for momentum transfer than the one recommended by the CORE-II experimental protocol (Griffies et al., 2009; Large and Yeager, 2009). Most importantly, and in order to improve the simulation of sea-ice characteristics, a value of 1 m s^{-1} was added to the CORE-II wind speeds prior to the wind stress calculation explaining the larger surface stress values, which will be shown to impact the mean state and trends in the Southern Ocean. Anomalies, computed as the last minus the first decade, are also shown in Fig. 3b as thin black lines for all models and as gray lines for the MMM. The thin black line standing out from the ensemble refers to the INMOM anomalies.

Buoyancy forcing is also an important player in sustaining a vigorous ACC transport and MOC in the Southern Ocean. Surface buoyancy forcing has already been extensively analyzed in the case of water mass transformation and sea-ice during 1988–2007 in CORE-II simulations (Downes et al., 2015). Regarding the ACC and the MOC, we are more interested in the evolution of the surface forcing, or trend, over the 60-year period of the CORE-II forcing. Surface buoyancy forcing in the Southern Ocean has experienced significant changes during 1948–2007, with comparable trends observed only in the tropical regions (not shown). The biggest contribution to buoyancy trends has come from surface heat fluxes, although freshwater fluxes near the Antarctic coast have implied significant modifications to the net buoyancy changes there. Decadal trends in net surface heat fluxes are shown in Fig. 4. What is evident from Fig. 4 is that all models reproduce a buoyancy gain trend over the Southern Ocean region up to 62–65 °S, polewards of which trends become negative in some models, implying buoyancy loss from the heat fluxes. It is also notable that the spread among models is larger than in the case of the surface momentum stress, because model's SSTs are taken into account in bulk formulas. Differences in sea ice cover also contribute to differences in surface buoyancy forcing. An extensive analysis of sea ice
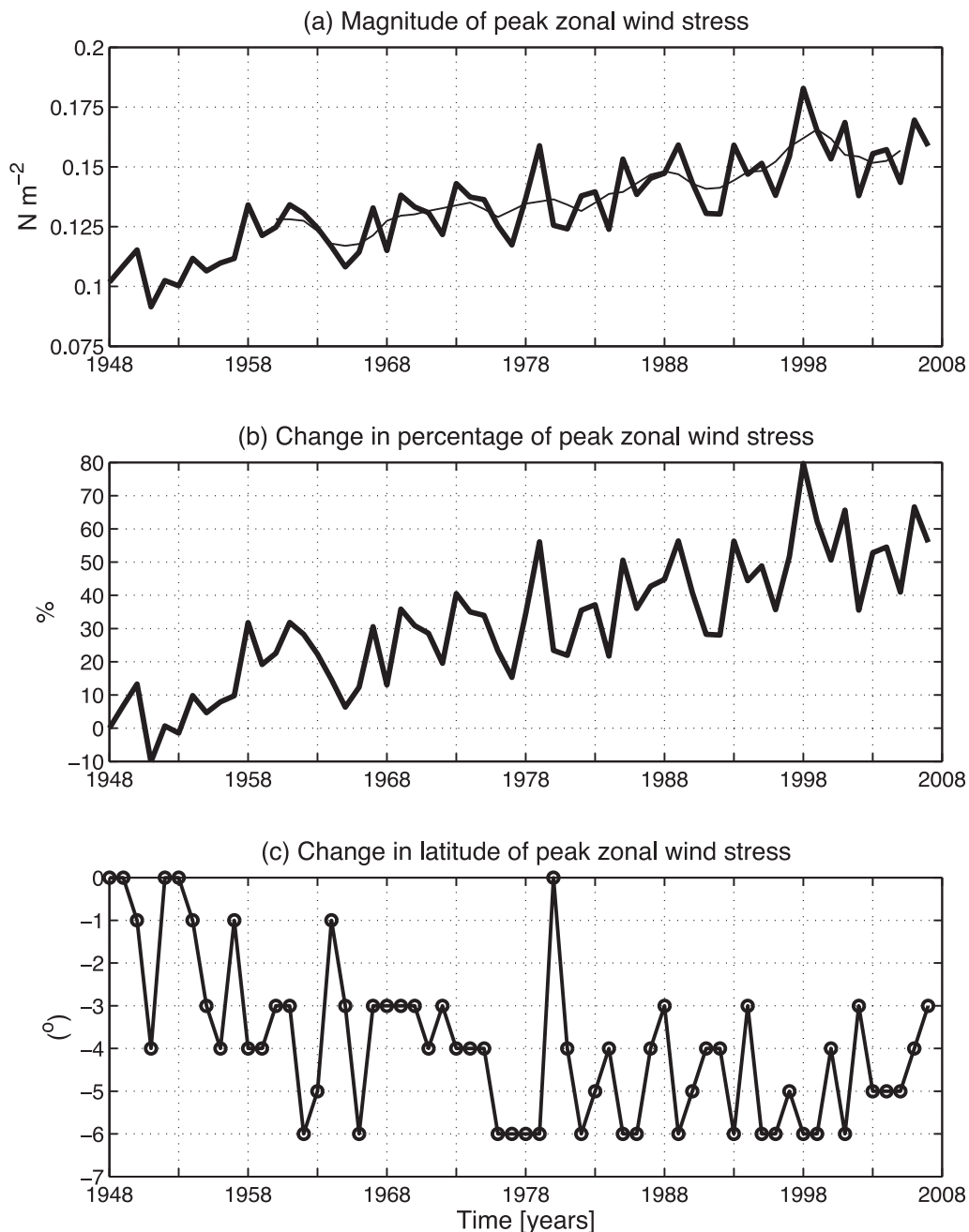
Fig. 2. Changes in zonal-mean zonal wind stress in the CORE-II multi model mean (MMM). (a) Time series of magnitude of peak zonal-mean zonal wind stress (thick line; in N m^{-2}), and its 10-year running mean for 1958–2007 (thin line), showing the overall strengthening of the westerlies from 1948 to 2007. (b) Change, in percentage, of the peak zonal-mean zonal wind stress relative to 1948. (c) Change, relative to 1948, in the latitude of the peak zonal-mean zonal wind stress. Negative values indicate a southward displacement of the peak.

properties in models participating in CORE-II can be found in Downes et al. (2015).

Variability in the upper limb of the MOC is believed to be largely dominated by wind forcing (e.g. Treguier et al., 2010), although recent studies have also highlighted the role of buoyancy flux changes and suggested a linear increase in the upper MOC with buoyancy gain (Morrison et al., 2011). The abyssal Antarctic Bottom Water (AABW) cell is instead largely controlled by surface buoyancy forcing in polar latitudes. Changes in heat fluxes influence the rate of AABW formation and the strength of the lower limb of the MOC (Rintoul and Naveira-Garabato, 2013), resulting in an increase of the abyssal overturning with a greater surface negative buoyancy flux. We note that CORE-II simulations disagree on the sign and magnitude of surface heat flux trend poleward of 65 °S (Fig. 4).

3. The Antarctic Circumpolar Current

The evolution over the five CORE-II cycles of the vertically-integrated annual-mean mass transport through Drake Passage for the seventeen models is given in Figs. 5 and 6. We consider the Drake Passage transport, and its response to changes in forcing, as representative of the large-scale features of the ACC. Integrating models for 300 years is not enough for equilibration of the high-latitudes and especially in the Southern Ocean, where low-frequency adjustment to local and remote forcing and deep bottom water formation processes likely require longer integrations. Most models, however, show a stabilization of the ACC transport after the first two to three cycles, and five cycles seem necessary for the characterization of the ACC evolution during the period 1948–2007. However, some models have
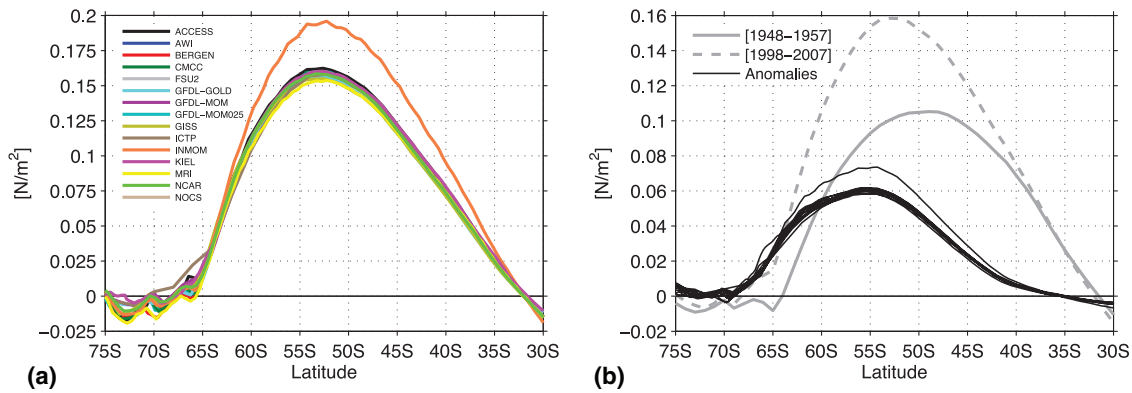
Fig. 3. Zonal-mean zonal wind stress for the participating ocean-ice models (data from FSU and KIEL025 are missing). (a) Time-mean during years 1948–2007, and (b) first decade (1948–1957, gray line) and last decade (1998–2007, dashed gray line) for the multi model mean (MMM), showing the strengthening and poleward shift. Also shown in (b) are the anomalies (last decade minus first decade, thin black lines) for all models. The INMOM model, because of a different momentum bulk formula and the addition of 1 m s^{-1} to the CORE-II winds, stands out from the other models.
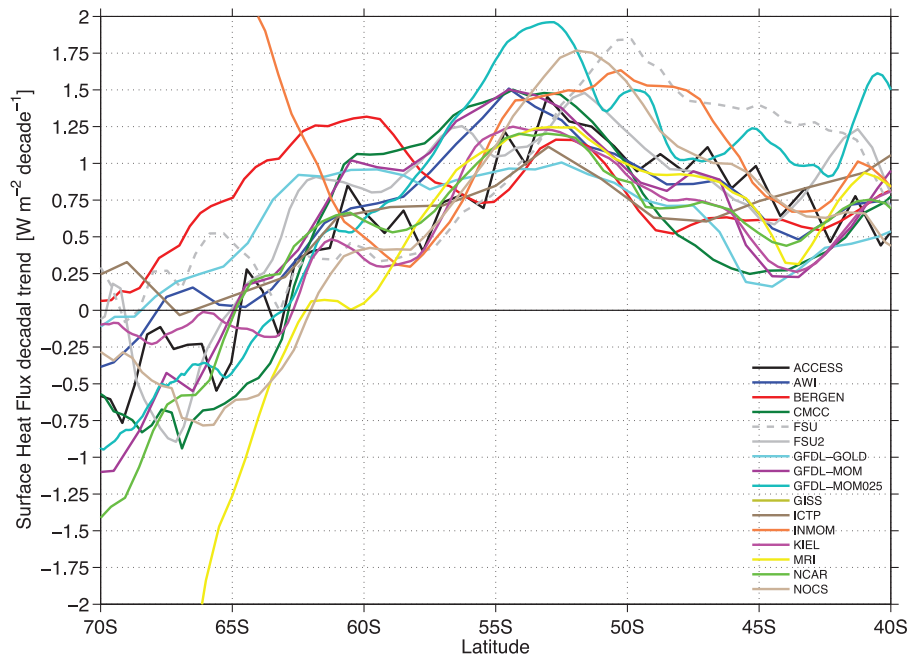
Fig. 4. Linear decadal trends for the zonally averaged surface heat flux (W m^{-2}/decade) for simulation years 1948–2007 in the fifth cycle (data from KIEL025 are missing). We show only those latitudes in the Southern Ocean. A positive sign indicates heat entering the ocean, thus adding buoyancy. INMOM trends go out of range poleward of ∼64°S and MRI trends go out of range poleward of ∼66°S.

not reached an equilibrium after the fifth cycle, and significant trends exist.

The FSU solution seems incoherent with the forcing, showing no sign of cycling through the forcing data, and with a general upward trend reaching transports up to 200 Sv (1 Sv ≡ 10^9 kg/s). GFDL-MOM025 also has an upward trend and would probably require a longer integration before reaching an equilibrium state. The INMOM model, despite its large transport (up to 280 Sv), seems stabilized after the third cycle. In MRI, the transport experiences an unstable behavior during the cycle, with the transport sharply increasing towards the end of the forcing period. The MRI model exhibits intense convection associated with the formation of a large open ocean Weddell Sea Polynya, resulting in an intensification of the MOC (Hirabara et al., 2012). See Marsland and Wolff (2001) for a detailed discussion of the interaction between ocean vertical stability and surface buoyancy fluxes that can result in the manifestation of such polynya in this region. Such intense and sudden convection alters the baroclinicity in the ACC region by freshening and cooling bottom waters, leading to an increase in the ACC transport. This burst

of convection is present throughout a 1500-year-long integration (Tsujino et al., 2011), thus pointing to a forcing related behavior rather than a spin-up issue in MRI.

The ACC transport in ICTP, KIEL and KIEL025 is relatively weak compared to the other CORE-II simulations, with a decreasing trend in the transport. In the case of the ICTP model, integrated for 10 cycles, the trend is more evident after the sixth cycle (not shown). The reason for both the weak mean value and the downward trend is due to a bottom water drift during the 300-year integration. In fact, and contrary to the MRI case, bottom water is getting warmer in all three models and AABW formation is diminishing. The Southern Ocean is thermodynamically adjusting to the loss of dense water by decreasing the meridional density gradient throughout the water column, causing the ACC to slow down (not shown). Hence, even if the upper vertical density structure does not differ significantly from the other models (see Fig. 7 in Downes et al. (2015) and Fig. 12 of this study), the bottom density structure and its drift are negatively impacting the stability of the ACC. This was also the case in Treguier et al. (2010), where a poor representation of AABW
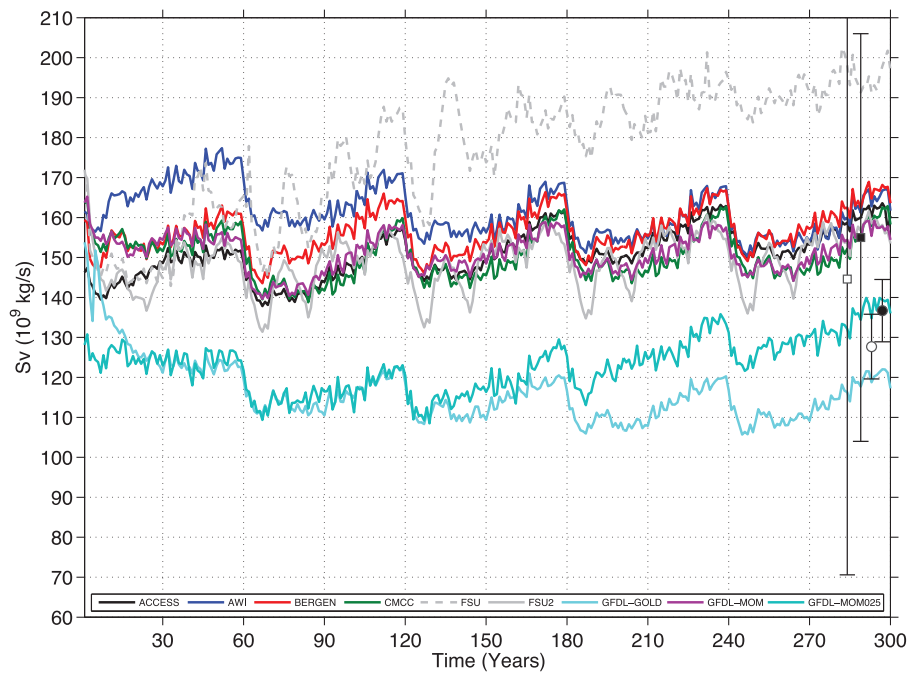
Fig. 5. Time series for the annual-mean vertically integrated mass transport (in Sv; 1 Sv ≡ 10⁹ kg/s) through the Drake Passage for the entire length of the simulation (300 years; five repeated cycles) for models ACCESS, AWI, BERGEN, CMCC, FSU, FSU2, GFDL-GOLD, GFDL-MOM and GFDL-MOM025. Also included are observational estimates from Cunningham et al. (2003) (black circle; 136.7 ± 7.8 Sv), Chidichimo et al. (2014) (white circle; 127.7 ± 8.1 Sv), the CMIP5 multi-model mean from Meijers et al. (2012) (black square; 155 ± 51 Sv), and the CMIP3 multi-model mean from Sen Gupta et al. (2009) (white square; 144.6 ± 74 Sv).
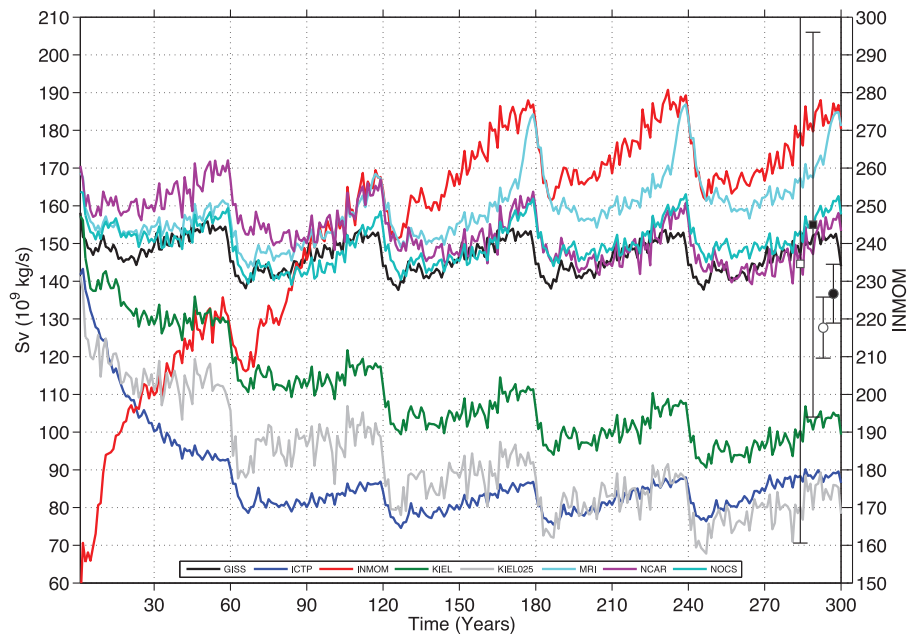

Fig. 6. As in Fig. 5 but for models GISS, ICTP, INMOM, KIEL, KIEL025, MRI, NCAR and NOCS. Note the different vertical axis for INMOM.

formation was found to be the cause for their ACC drift. The absence of surface salinity restoring under sea-ice seems the most robust factor explaining the drift in bottom water formation and ACC downward drift in ICTP, KIEL and KIEL025. The time scale chosen for SSS restoring is probably not the cause as this is five times stronger in KIEL025 compared to KIEL (see Table 1). The Southern Ocean response is thus very sensitive to surface forcing and details of how surface fluxes are treated, both affecting water mass formation near the Antarctic coast and setting a time scale for reaching a Southern Ocean equilibrated state.

Figs. 5 and 6 also include recent observational estimates for the ACC transport (Chidichimo et al., 2014; Cunningham et al., 2003) and the Coupled Model Intercomparison Project (CMIP) Phases 3 and 5 multi-model mean values as reported in Sen Gupta et al. (2009) and Meijers et al. (2012), respectively, with corresponding standard deviations. CMIP results encompass a large spread in ACC transport values, although the standard deviation in CMIP5 is considerably reduced compared to CMIP3. Besides ICTP, KIEL and KIEL025, all CORE-II simulations fall within CMIP5 estimates. The multi-model mean CMIP5 transport for the period 1976–2006 is 155 ± 51 Sv (black square), and

Table 2
Mean mass transport through the Drake Passage (in Sv) over the period 1958–2007, where MMM is the multi-model mean (MMM* refers to a MMM computed excluding FSU and INMOM). Several observational estimates are also included: Cunningham et al. (2003) for the period 1993–2000, Koshlyakov et al. (2007) for year 2005, Renault et al. (2011) for year 2006 and Chidichimo et al. (2014) for the period 2007–2011. Multi-model means for the period 1976–2006 from CMIP3 (Sen Gupta et al., 2009) and CMIP5 (Meijers et al., 2012) coupled models are also given. For a proper comparison, the CORE-II ACC means and MMM over the same period are also reported. Also listed for each model are the transport changes in % (computed for the last decade and relative to year 1958), the decadal trend and correlation with the SAM index in the second, third and fourth columns, respectively.

Model	Mean (Sv) 1976–2006	Mean (Sv) 1958–2007	Change (%)	Trend (Sv decade^{-1})	Corr. SAM
1. ACCESS	159	156 ± 4.2	5.2	2.74	0.82
2. AWI	160	158 ± 4.7	5.8	2.65	0.79
3. BERGEN	163	160 ± 4.8	6.8	2.65	0.85
4. CMCC	154	151 ± 5.4	6.9	3.11	0.74
5. FSU	195	193 ± 4.0	2.8	1.68	0.60
6. FSU2	156	153 ± 4.8	6.9	2.99	0.69
7. GFDL-GOLD	117	114 ± 4.6	7.6	2.86	0.84
8. GFDL-MOM	154	152 ± 4.2	5.3	2.70	0.85
9. GFDL-MOM025	134	132 ± 4.1	7.1	2.46	0.81
10. GISS	149	147 ± 3.9	5.4	2.32	0.71
11. ICTP	88	86 ± 3.3	7.9	2.05	0.83
12. INMOM	268	264 ± 7.2	8.7	4.67	0.84
13. KIEL	101	99 ± 4.0	5.8	2.18	0.82
14. KIEL025	82	80 ± 4.1	7.2	1.95	0.74
15. MRI	169	166 ± 7.1	8.4	4.26	0.64
16. NCAR	149	147 ± 5.1	6.1	2.79	0.78
17. NOCS	154	152 ± 4.6	6.1	2.71	0.76
MMM	150.3 ± 42.7	147.6 ± 42	6.47 ± 1.42	2.76 ± 0.75	0.77
MMM*	139.3 ± 28.6	136.8 ± 28	6.56 ± 0.98	2.70 ± 0.55	0.78
CMIP5 (Meijers et al., 2012)	155 ± 51				
CMIP3 (Sen Gupta et al., 2009)	144.6 ± 74.1				
Chidichimo et al. (2014)	127.7 ± 8.1				
Renault et al. (2011)	136.3				
Mazloff et al. (2010)	153 ± 5				
Koshlyakov et al. (2007)	130				
Cunningham et al. (2003)	136.7 ± 7.8				

the ACC for ACCESS, AWI, BERGEN, CMCC, GFDL-MOM, FSU2, GISS, NCAR and NOCS lies very close to this value (see Table 2). Both observed values (white and black circles) are weaker than CMIP estimates, with the most recent estimate of Chidichimo et al. (2014) being 127.7 ± 8.1. GFDL-GOLD as well as GFDL-MOM025, although not fully equilibrated, are approaching the observed transports.

In Table 2 the mean ACC transport value, over the period 1958–2007, is provided from all individual models and the multi model mean (MMM). The ACC mean over the 1976–2006 period is also given in Table 2 for a better comparison with some recent observed transports, CMIP ensemble estimates and products based on data assimilation. In general, both CORE-II and CMIP ocean models seem to overestimate the observed ACC transport, although large uncertainties exist in observational estimates (e.g. Griesel et al., 2012). The ACC transport mean and standard deviation in CORE-II and 23 CMIP5 models analyzed in Meijers et al. (2012) are very similar. Excluding the FSU and INMOM models, with 'too-large' transports (MMM*), reduces the difference with the observed transports, and now the MMM* lies closer to the most recent observations of Chidichimo et al. (2014). It should also be noted that the MMM CORE-II ACC transport is reduced because of the weak transports modelled by ICTP, KIEL and KIEL025.

The time-mean baroclinic ACC transport is determined by the meridional density field through thermal wind balance. Fig. 7 shows the time mean ACC transport against the meridional density difference ($\Delta\rho$), computed as the difference between the averaged potential density, referenced to 2000 db, within 65–60 °S and 45–40 °S, and vertically averaged between 0 and 1500 m. Unsurprisingly, the correlation (again excluding the outlier INMOM) is significant (0.81), as seen in CMIP models with different flavors of mesoscale parameterizations (Kuhlbrodt et al., 2012; Meijers et al., 2012). A consistent relationship between SSS restoring time scale and $\Delta\rho$ could not be

established, but models with an eddy-induced advection coefficient κ that is fixed in time or absent (FSU, FSU2, INMOM and MRI) show considerably larger values of $\Delta\rho$.

3.1. The ACC during the 5th cycle

The evolution of the Drake Passage transport during the fifth cycle is shown in Fig. 8. Together with the CORE-II time series, we include again the observational estimates for the period 1993–2000 (Cunningham et al., 2003) and 2007–2011 (Chidichimo et al., 2014). As previously discussed, INMOM has the largest transport (note the different vertical scale), MRI shows a sharp increase in transport from the 1990s due to the opening of a large polynya, and FSU also has a strong transport which cannot be considered to be equilibrated given the low repeatability over the five cycles (see Fig. 5). GFDL-MOM025 matches the observed estimate for the period 1993–2000, but this is likely to be fortuitous since the ACC is experiencing a trend towards higher values (Fig. 5). During the period 2007–2011 Chidichimo et al. (2014) report a 9 Sv decrease in ACC transport with respect to the estimates of Cunningham et al. (2003) in the previous decade. The change, exceeding twice the standard error of the mean estimates of Chidichimo et al. (2014), suggests a significant interannual variability in the Drake Passage transport. Our CORE-II simulations finish in year 2007, so that a comparison with the observed variability is not possible. However, we note that most models show a flattening and a sign of decreasing trend in transport at the end of the cycle, although it is hard to distinguish the evolution of the last years relative to internal variability during the 60-year period.

As suggested in Section 2.1, the interannual variability of the Drake Passage transport in CORE-II simulations will be shown to be dominated by momentum forcing. The above does not necessarily imply that the mean transports are significantly correlated with the
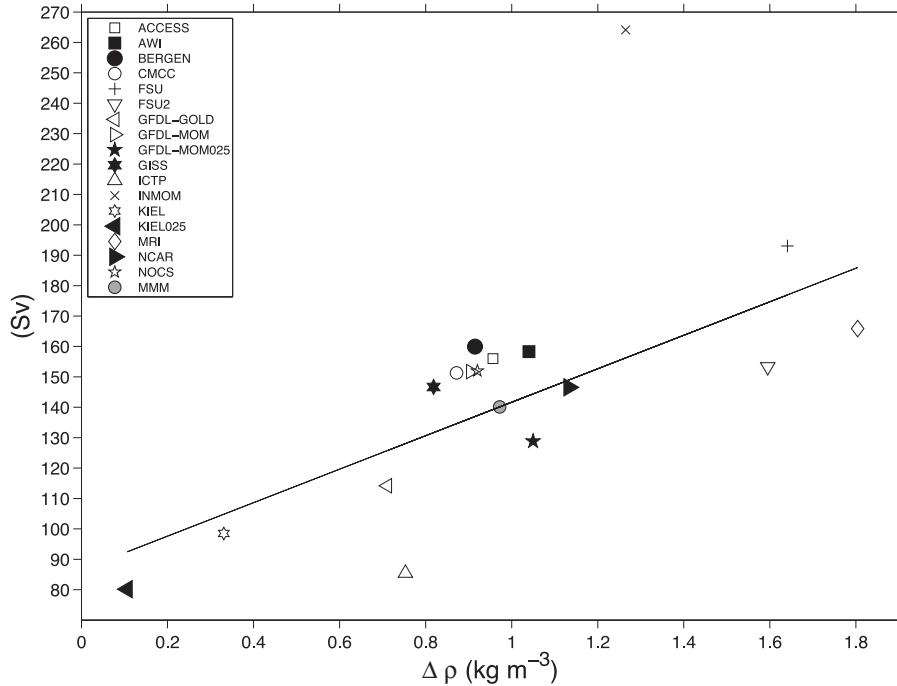
Fig. 7. The time mean Drake Passage transport (in Sv) against the upper-ocean meridional potential density difference $\Delta\rho$ (referenced to 2000 db; in kg m^{-3}) across the ACC. $\Delta\rho$ is defined as the difference between the potential density averaged within 65–60°S and 45–40°S, and vertically averaged between 0 and 1500 m. The correlation coefficient, excluding the INMOM model, is 0.78.
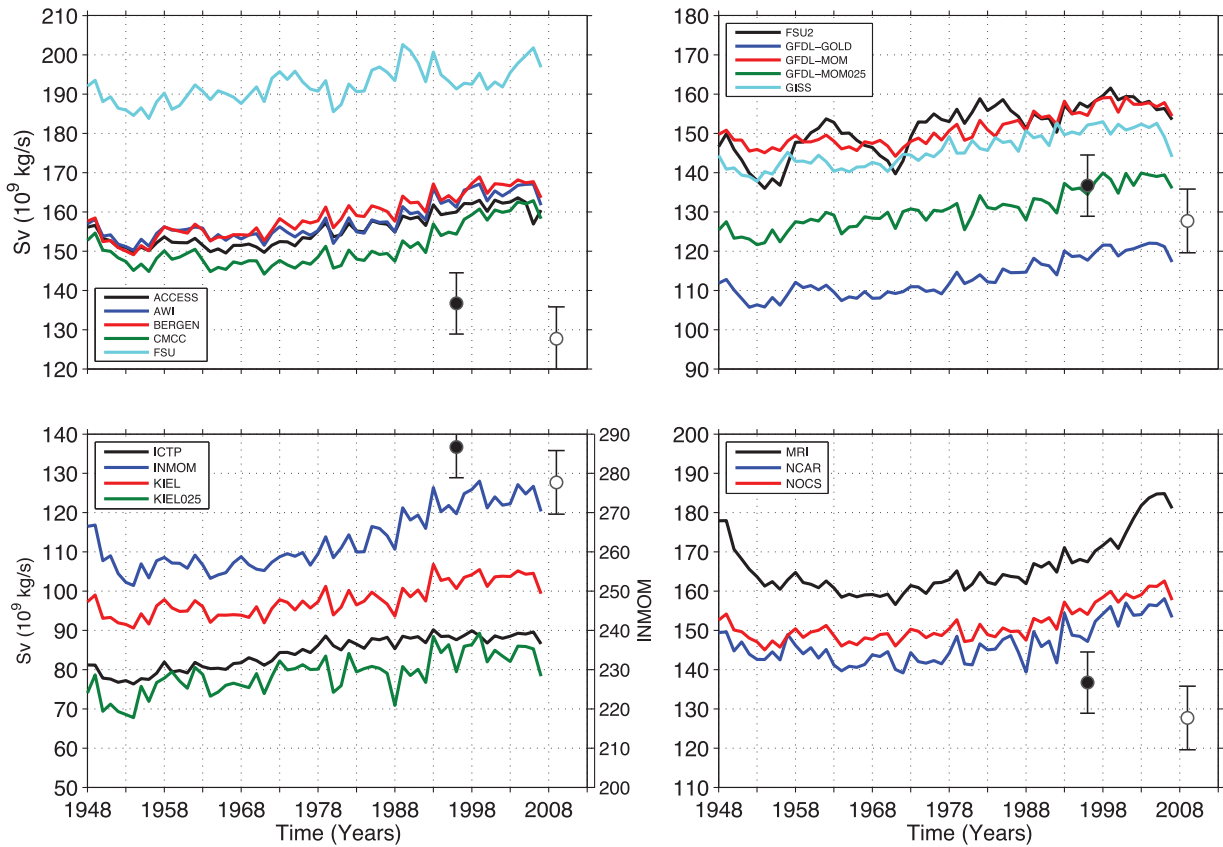

Fig. 8. Time series for the annual-mean vertically integrated mass transport (in Sv) through the Drake Passage for the fifth cycle. Note the different vertical scales on each subplot, though with the same 90 Sv range, thus allowing for direct comparisons of fluctuations. Also note the unique scale for the INMOM simulation. Also included are observational estimates from Cunningham et al. (2003) (black circle; 136.7 ± 7.8 Sv for the period 1993–2000) and Chidichimo et al. (2014) (white circle; 127.7 ± 8.1 Sv for the period 2007–2011). Observations are plotted at the mid point of their respective time ranges.
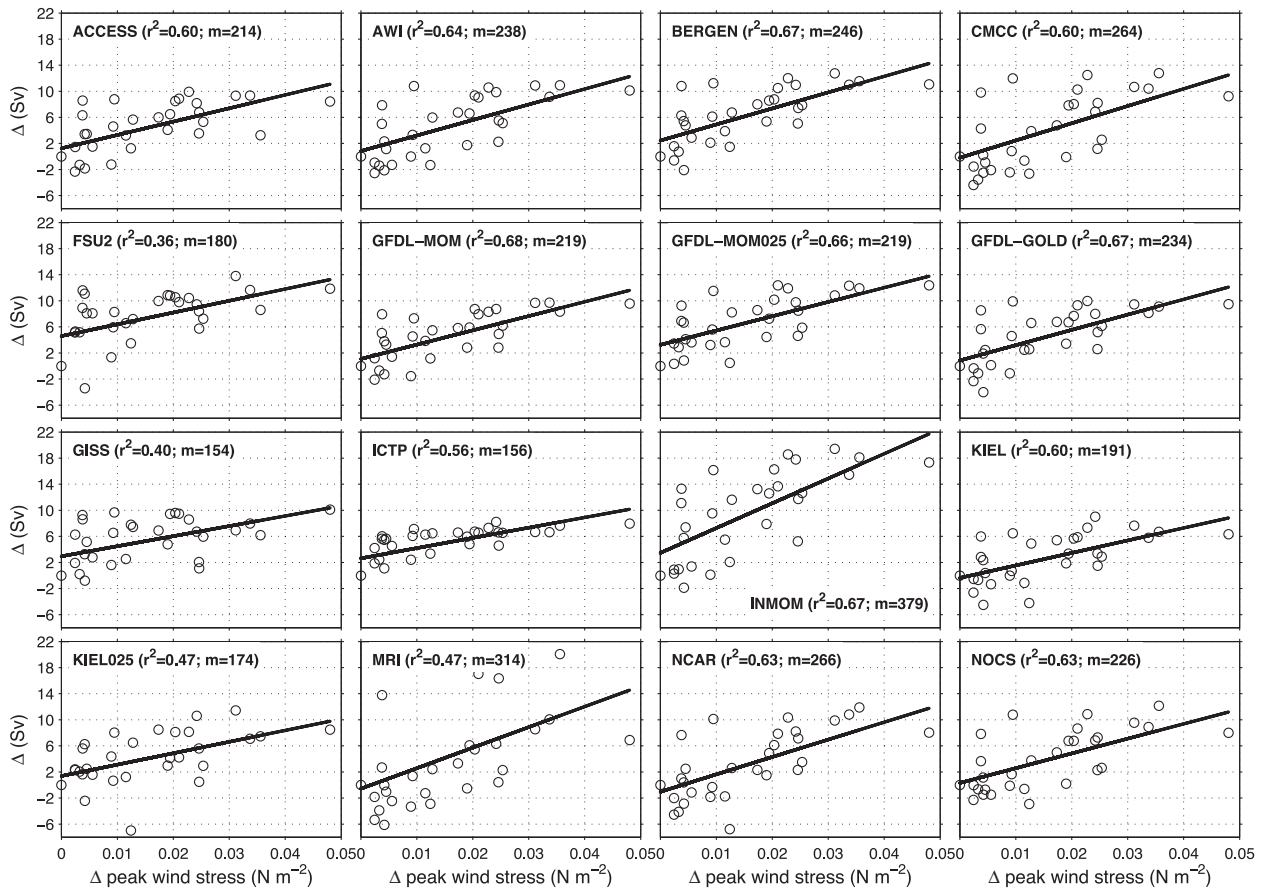
Fig. 9. Scatterplots for annual changes in Drake Passage transport (in Sv) vs changes in peak wind stress (τ; in N m^{-2}). The period analyzed is the last five decades, from 1958 to 2007, and changes are relative to year 1958. A linear regression is shown relating yearly changes in ACC transport and changes in peak wind stress, along with the coefficient of determination (r^2) and slope (m).

strength of the wind stress, as also described in Meijers et al. (2012) and Downes and Hogg (2013) in the case of CMIP5 coupled models. In fact, the steeply sloped isopycnals partly responsible for the sharp meridional density gradient in the Southern Ocean are the result of both momentum and buoyancy forcing. Similarly, the treatment of buoyancy forcing – and the SSS restoring time scale certainly plays a major role in the case of CORE-II simulations – will also determine the ACC transport. For example, Griffies et al. (2009) showed the dependence of the Drake Passage transport strength and stability upon details of salinity restoring (their Fig. 27), and tests with the ICTP model confirmed a strong relationship between SSS restoring time scale and ACC strength (not shown).

Downes and Hogg (2013) analyzed the Southern Ocean mean response to a severe climate change scenario in thirteen CMIP5 climate models, concluding that changes in ACC strength are correlated with surface heat and freshwater flux changes. Here, we focus on variability of the transport during the 1958–2007 period. The ACC experiences a strengthening over the last 4–5 decades, reaching a value around 10 Sv higher than at year 1958 for most models (Fig. 8). Exceptions are again the INMOM and MRI models, with much larger variations in transport ($\sim$ +20 Sv), and FSU which presents larger interannual fluctuations. In order to quantify individual variations in ACC strength, we look at the transport averaged during the last decade (1998–2007) relative to year 1958. Despite the large difference in mean ACC transports, all models show a strengthening that is < 9% (see Table 2), with an overall increase in zonal wind stress of around 30% for the same period (see Fig. 2b). Since most modelled ACCs are strengthening by a similar amount ($\sim$10 Sv), models with a weaker mean transport will of course result in larger percentage variations

compared to 1958, as is the case for GFDL-GOLD, KIEL, KIEL025, ICTP and to some extent GFDL-MOM025.

Regardless of the individual change in ACC magnitude, all models are characterized by similar interannual anomalies during the CORE forcing period, with coincident peaks and troughs. The interannual correlation between different models indicates that the anomalies are largely determined by atmospheric forcing. A measure of the relationship between ACC and wind stress is presented in Fig. 9, where annual ACC anomalies are plotted against annual anomalies in peak wind stress for the period 1958–2007 and relative to 1958. All models show high correlations with changes in wind stress, with higher slopes coincident with larger variations in transports (e.g., INMOM and MRI).

Looking at Fig. 8, the overall evolution of most ACCs follows 3 steps: a relatively stable period up to the 1970s, followed by a substantial increase in transport until the late 1990s and finally a flattening (or perhaps a downward trend as reported by the observations) up to the end of the cycle. Trends are consistent with and follow anomalies in the overlying wind stress driving the circulation, as shown in Fig. 1 and Fig. 2. The 10-year running mean zonal-mean peak zonal wind stresses in Fig. 2a exemplify the trend followed by the momentum flux during the CORE period, with a sharp strengthening of the winds in the 1980s and 1990s followed by a weakening in the 2000s.

3.2. Trends over years 1958–2007

Future climate forcing scenarios have shown ACC decadal trends over the 21st century ranging from -5.76 Sv/decade to 1.58 Sv/decade
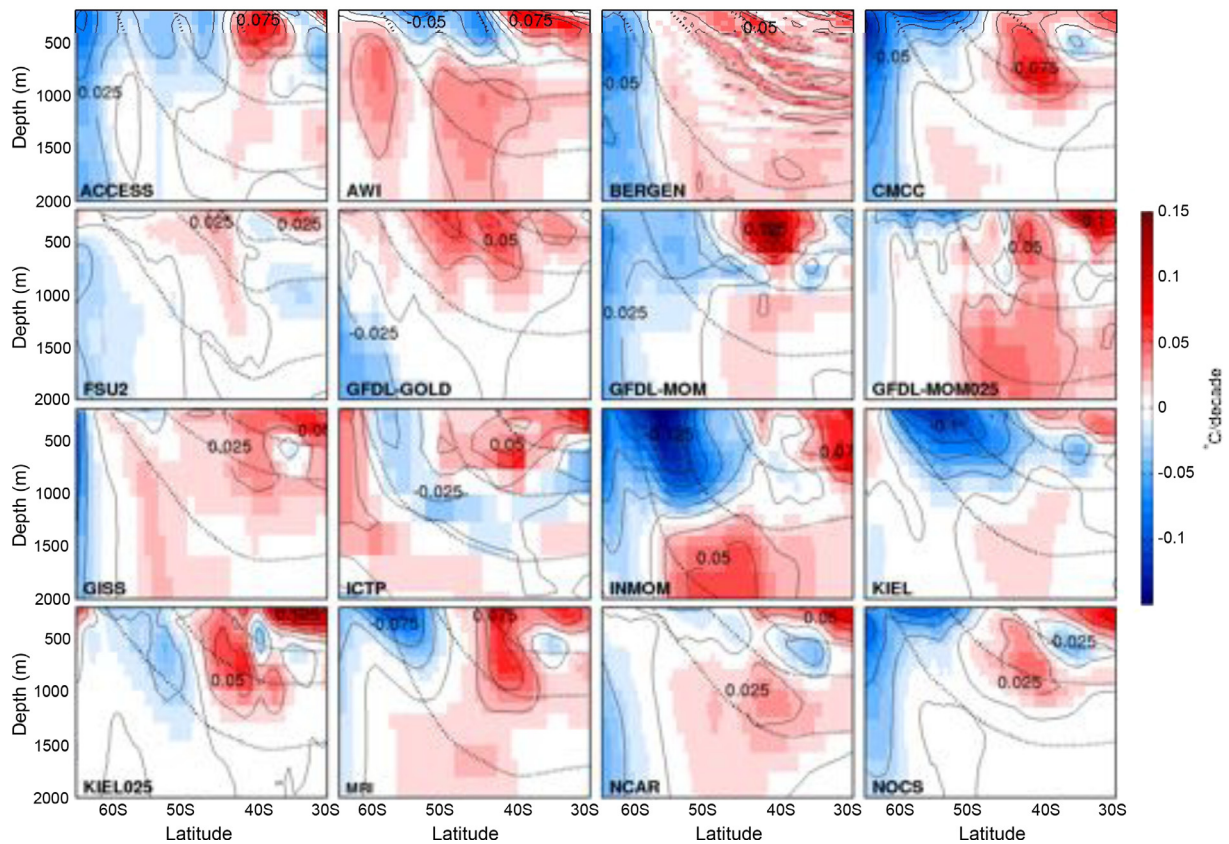
Fig. 10. Linear decadal trend (°C/decade) in zonal mean temperature for the years 1958-2007, computed over the fifth CORE-II cycle. In order to highlight interior changes, the top 100 m are omitted. Contour interval is 0.025 °C/decade (solid lines). Also included are the 35.75, 36.25 and 36.75 kg/m^3 time-mean potential densities referenced to 2000 db (dotted lines).

in CMIP3 coupled models (Wang et al., 2011). Despite the strengthening and poleward displacement of the westerly winds, decelerations of the ACC are attributed to (i) the poleward expansion of the subtropical gyres causing the narrowing, equatorward shift and reduction in ACC transport, and to (ii) the increased surface buoyancy responsible for a reduction in meridional density gradients across the ACC (Meijers et al., 2012; Wang et al., 2011). Individual ACC decadal trends in CORE-II simulations are given in Table 2, with values ranging from 1.68 to 4.67 Sv/decade. Changes in wind stress, surface buoyancy or their combination have not resulted so far in a slow down of the ACC in any of the ocean models.

Consistent with previous results (see Fig. 8), models with a constant or absent eddy-induced coefficient κ (FSU2, INMOM and MRI) have the largest trends (2.99, 4.67 and 4.26 Sv/decade, respectively), whereas eddy-permitting models and models with time-dependent three-dimensional κ (AWI, BERGEN, GFDL-MOM025, GISS, KIEL025 and NCAR) show weaker trends (2.65, 2.65, 2.46, 2.32, 1.95 and 2.89 Sv/decade, respectively). Both ICTP and KIEL have been shown to undergo a significant ACC transport weakening during the 300 years of integration, and this behavior partially explains their weak decadal trends during 1958–2007. FSU, due to the intense transport reduction simulated over the last two decades (Fig. 8), shows the weakest decadal trend. FSU was shown to suffer from a strong drift (Fig. 5), which results in a poor simulation of Southern Ocean dynamics. The improved version of FSU2 and its stronger SSS restoring in the Southern Ocean produce an ACC transport that is more consistent through the forcing cycles, has a much reduced interior trend, and simulates a more realistic MOC both in the Atlantic and Southern Ocean (not shown). For these reasons we will show only results from FSU2 in the following analyses.

ACC trends are related – through thermal wind – to the structure of the upper-ocean interior and we now discuss the temperature, salinity and density trends in the CORE-II simulations. As discussed in Downes et al. (2015), models have a cool and fresh bias south of 50 °S, and warm and saline biases north of 50 °S. Different SSS restoring time scales, restoring under sea-ice or not, and the methodology chosen for the runoff discharging might also partially offset the effects of CORE-II based surface momentum and buoyancy forcing on the upper Southern Ocean stratification during the CORE-II cycle. Fig. 10 shows temperature decadal trends for the upper 2000 m, zonally averaged and with the top 100 m removed so as to highlight interior changes. North of the ACC core (~50 °S), a warming is evident for all models, whereas south of 60 °S most models show a cooling penetrating deep into the column. The cooling trend was also pointed out in Downes et al. (2015), where the trend in the 200–700 m averaged temperature was shown to be localized mostly in the Indian and Pacific sectors. The simulations, although surface trends are not shown in Fig. 10, bear good resemblance, in both structure and magnitude, to observed trends in the Southern Ocean (Bintanja et al., 2013; Böning et al., 2008; Gille, 2002; IPCC, 2013). Despite the overall warming from surface heat fluxes, surface-intensified cooling and freshening of the upper layers have recently been observed polewards of 60 °S (Bintanja et al., 2013). Bintanja et al. (2013) explained the cool and fresh surface layers via basal melting of Antarctic ice shelves, leading to sea-ice growth. CORE-II simulations have no specified melt water scenario. Instead, the melt is constant in time and distributed uniformly around Antarctica.

Models participating in CORE-II do not faithfully reproduce sea-ice trends over the 1988–2007 period (Downes et al., 2015), and many physical mechanisms and biases could be responsible for
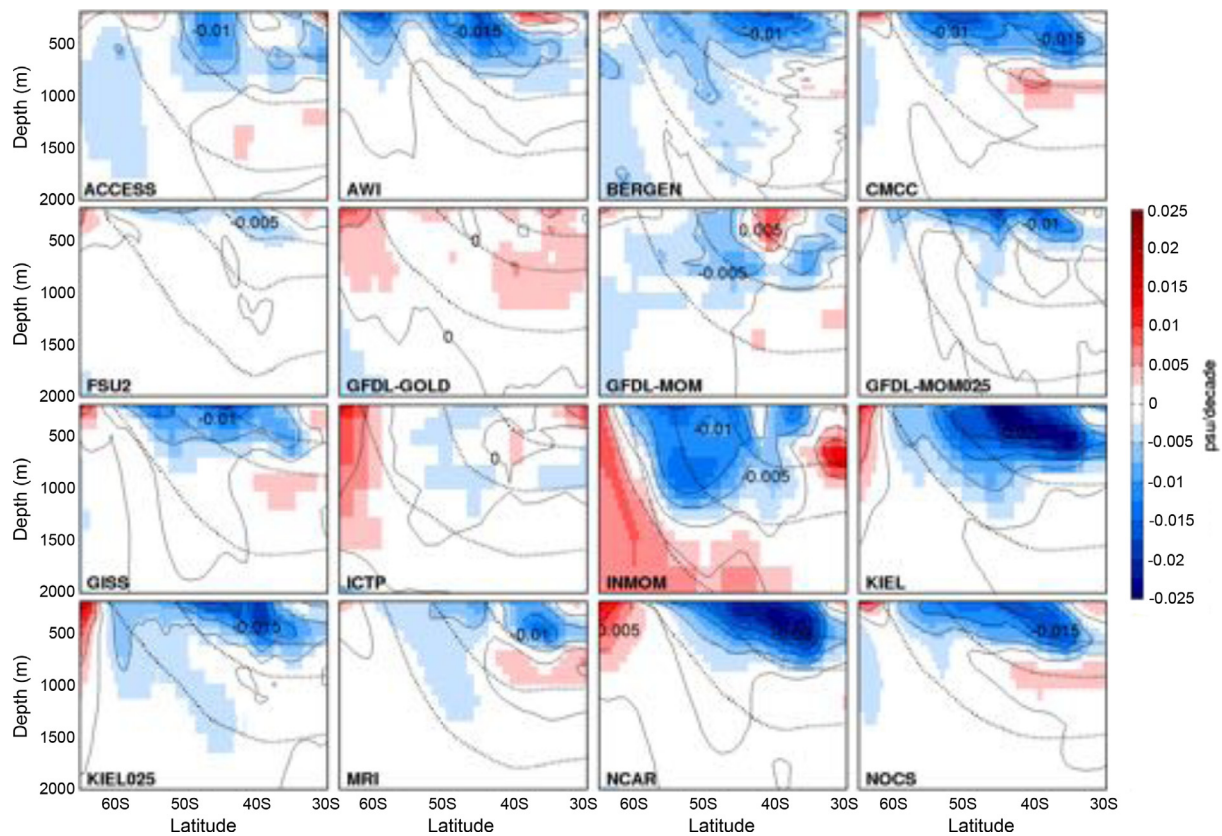
Fig. 11. Linear decadal trend (p.s.u./decade) in zonal mean salinity for the years 1958–2007, computed over the fifth CORE-II cycle. In order to highlight interior changes, the top 100 m are omitted. Contour interval is 0.005 p.s.u./decade (solid lines). Also included are the 35.75, 36.25 and 36.75 kg/m^3 time-mean time-mean potential densities referenced to 2000 db (dotted lines).

counteracting and offsetting the role of the upper ocean in sea-ice concentration increase. Positive SAM trends, and especially its poleward migration and associated increased atmospheric cooling around Antarctica, could also explain the strong cooling south of the ACC affecting the upper 2000 m in many models (Thompson et al., 2011). The observed subsurface warming north of 50 °S is well captured by the models, especially in the case where stirring across the ACC through isopycnal eddy fluxes is better represented (AWI, BERGEN, GFDL-GOLD, GFDL-MOM025, GISS, NCAR), with trends of ~0.05 °C decade^{-1} below the depth of 1000 m, as previously observed (Bintanja et al., 2013; Böning et al., 2008).

Zonal-mean salinity trends are more coherent across models (Fig. 11), with all models but GFDL-GOLD simulating a freshening of the surface layers across the ACC. In fact, a wedge of fresh thermocline waters is seen slanting down along isopycnals (~45 °S and down to ~750 m), as also reported in the observations of Curry et al. (2003). The freshening is consistent with the increase in surface freshwater flux and poleward shift in the westerlies during the second half of the twentieth century. A positive trend in subsurface salinity polewards of 60 °S is also simulated by the majority of models, most likely due to brine rejection as sea ice forms.

The general warming and freshening trends, caused by both momentum and buoyancy forcing, affect the upper-ocean structure and result in density trends as shown in Fig. 12. More than the quasi-uniform freshening over the bulk of the ACC, it is the heating that seems to dominate over the density trend. Models simulating a warming north of the ACC and cooling south of the ACC will strengthen the meridional density gradient across the ACC, resulting in a larger strengthening of its transport.

To some extent, all models project an increase in upper-ocean meridional density gradient, and the relationship between the ACC

transport and $\Delta\rho$ still holds when trends are considered (Fig. 13). Fig. 12 also shows, as in Böning et al. (2008), the downward migration of isopycnals during the period considered. Although changes in isopycnal slopes are certainly minimal compared to previous idealized studies (Farneti et al., 2010; Farneti and Gent, 2011; Gent and Danabasoglu, 2011), some models have experienced a steepening in the tilt of isopycnals across the ACC latitudes (~45–60 °S). This steepening is evident when comparing the trends for $\sigma_2 = 36.75$–36.50 in the case of ACCESS, CMCC, GFDL-MOM, INMOM, KIEL, MRI and NOCS. Other CORE-II simulations, instead, only present a general subsidence of isopycnal surfaces, as found in Böning et al. (2008), due to a buoyancy gain reaching below 1000 m (AWI, BERGEN, GFDL-GOLD, GFDL-MOM025, GISS, KIEL025 and NCAR).

3.3. The ACC and the SAM

Previous studies have analyzed the correlation between the ACC transport and SAM, with eddy-permitting models (~1/4°) showing a linear relationship between the two and an acceleration of the ACC when the SAM is in its positive phase (Dufour et al., 2012; Sen Gupta and England, 2006; Treguier et al., 2010). ACC transport anomalies, in the MMM and for individual members during the 1958–2007 period, are plotted in Fig. 14 together with the SAM index, computed as the difference in normalized zonal mean annual-mean sea level pressure at 40°S and 65 °S. The correlation coefficient between the SAM and the MMM series is 0.77, which is higher than previous estimates (~0.46) with transient simulations (Treguier et al., 2010) or reanalysis data sets (Yang et al., 2007). A possible explanation for the higher correlation is the inclusion of an ensemble of seventeen models, whereas previous studies have reported on single realizations which, as seen
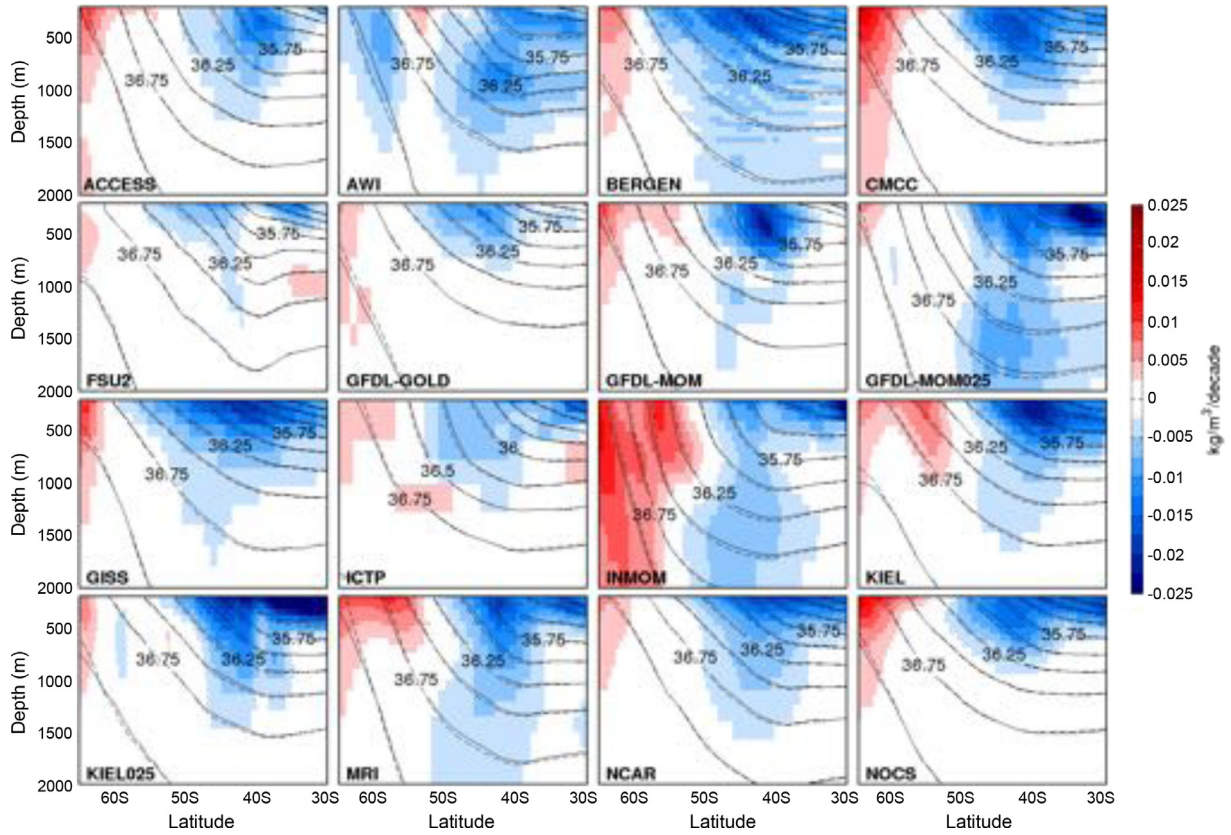
Fig. 12. Linear decadal trend (kg/m^3/decade) in zonal mean potential density referenced to 2000 db (σ_2) for the years 1958–2007, computed over the fifth CORE-II cycle. Black contours show the migration of isopycnal surfaces over the five decades considered: solid (dashed) lines are potential densities obtained by subtracting (adding) the linear trends over two and a half decades from (to) the time-mean values. In order to highlight interior changes, the top 100 m are omitted. Contour interval is 0.003 kg/m^3.
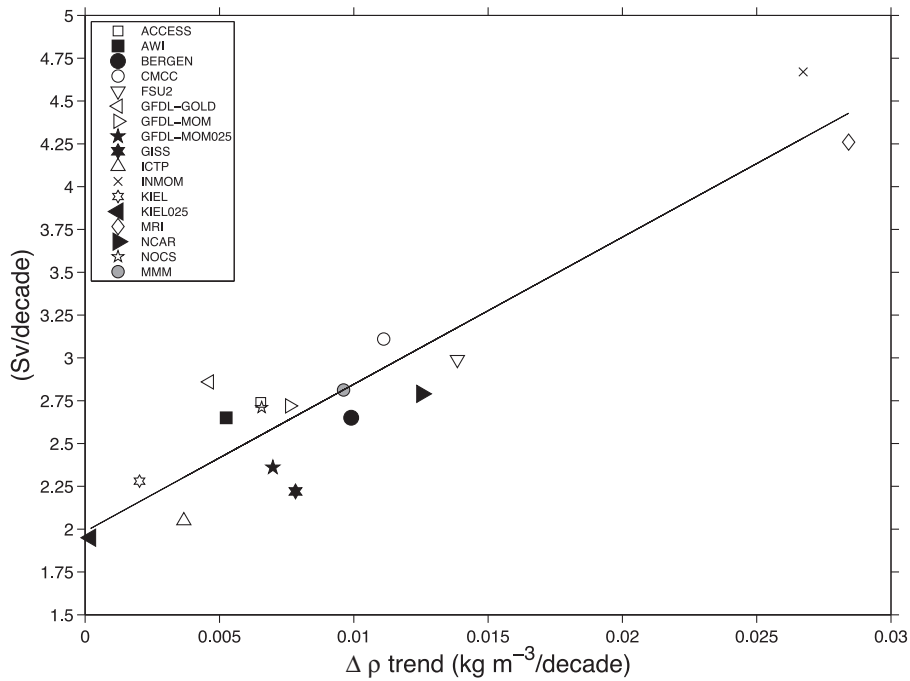

Fig. 13. As in Fig. 7 but for trends in ACC and upper-ocean meridional potential density gradient (referenced to 2000 db) computed over the last 50 years (1958–2007). The correlation coefficient is 0.79. Eddy-permitting models and models with a three-dimensional κ are plotted with black filled symbols.
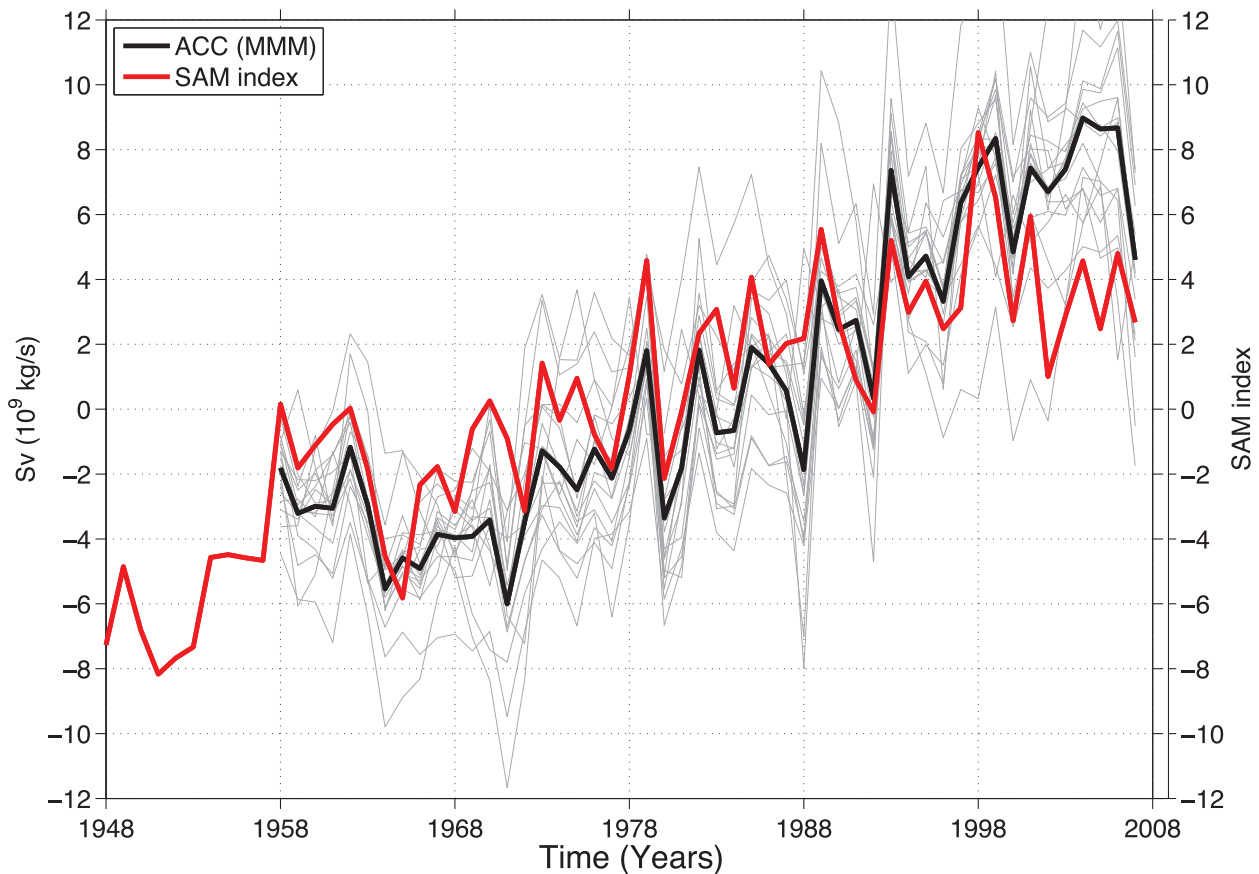
Fig. 14. The multi-model-mean (MMM) Drake Passage transport anomalies (with respect to the 1958–2007 mean; in Sv) are shown by the black line, gray lines refer to individual models transport anomalies, and the SAM index is shown by the red line (right axis). The MMM-SAM correlation is 0.77, with values ranging from 0.69 (FSU2) to 0.85 (BERGEN and GFDL-MOM). (For interpretation of the references to colour in this figure legend, the reader is referred to the web version of this article.)

from the individual CORE members (gray lines in Fig. 14), can vary substantially and result in different correlations with the SAM.

Other than MMM results, individual correlations are also useful in evaluating different model responses to SAM forcing. Table 2 reports the correlations between annual-mean anomalies in ACC transports and the annual-mean SAM index. FSU2 and MRI present correlations of 0.69 and 0.64, respectively. In contrast, all other models have correlations higher than 0.7, with correlations > 0.8 achieved by eight models (ACCESS, BERGEN, GFDL-GOLD, GFDL-MOM, GFDL-MOM025, ICTP, INMOM and KIEL). There is no obvious clustering of correlations into models of similar resolution, details of the parameterization or other physical characteristics. These high correlations suggest that the modelled ACC is dominated by momentum flux changes, and that SAM anomalies do accelerate the ACC transport on the interannual time scale.

4. The Southern Ocean meridional overturning circulation

The total, or residual, MOC can be written as a combination of the Eulerian-mean MOC, $\overline{\Psi}$, and the overturning circulation associated with eddies, Ψ^* (e.g. Marshall and Radko, 2003). Most of the models participating in CORE-II use a parameterization for mesoscale eddies (see Table 1 and Appendix B) and two streamfunctions are readily computed: one for the resolved (Eulerian mean) flow and one for the parameterized eddy-induced component. The sum of the two overturning streamfunctions is the residual circulation in each model, $\Psi_{\mathrm{res}} = \overline{\Psi} + \Psi^*$ (see also Appendix A).

Fig. 15 shows the time-mean Ψ_{res} in depth space in the CORE-II simulations. A surface clockwise circulation is visible in all models, ranging from 24 to 28 Sv and reaching depths between 2000

and 4000 m. This is the wind-driven Deacon Cell (Döös and Webb, 1994; Speer et al., 2000), and its strength is given by the surface wind stress, hence the very similar time-mean magnitude. Only INMOM has a stronger Deacon Cell, of about 40 Sv, due to the stronger wind stress forcing in the model and the lack of a parameterization for mesoscale eddies (see discussion in Section 2.1). Larger variations are present in the strength of the anti-clockwise Lower Cell, from 20 Sv in GFDL-GOLD to non-existing in GFDL-MOM025, KIEL and KIEL025. A schematic of the main Southern Ocean cells in depth-space is given in Fig. 16a.

The Deacon Cell is mostly an artifact of the zonal and vertical integration at fixed depth, and does not reflect any real cross-isopycnal flow. Indeed, a depth-space representation of the meridional overturning streamfunction is not the most suitable characterization of the Southern Ocean overturning circulation, which is more properly described when net transports are computed in potential density space, resulting in a better characterization of water mass transports (Ballarotta et al., 2013; Döös and Webb, 1994; Farneti et al., 2010; Hallberg and Gnanadesikan, 2006; Treguier et al., 2007). Unlike the streamwise-averaged model of Marshall and Radko (2003), where the contribution of stationary eddies to the MOC is eliminated, our zonally-averaged decomposition is only identifying an Eulerian zonal mean component $\overline{\Psi}$ and a transient eddy-induced circulation Ψ^*, neglecting the important role of standing eddies. In fact, previous studies have shown that the stationary eddy term can be larger than the transient eddy term in a zonally-averaged analysis of the Southern Ocean (Hallberg and Gnanadesikan, 2001; Volkov et al., 2010), and that the standing-eddy part only vanishes when zonal integration is performed along depth-dependent horizontal isolines of time-mean buoyancy or time-mean streamlines (Viebahn and Eden,
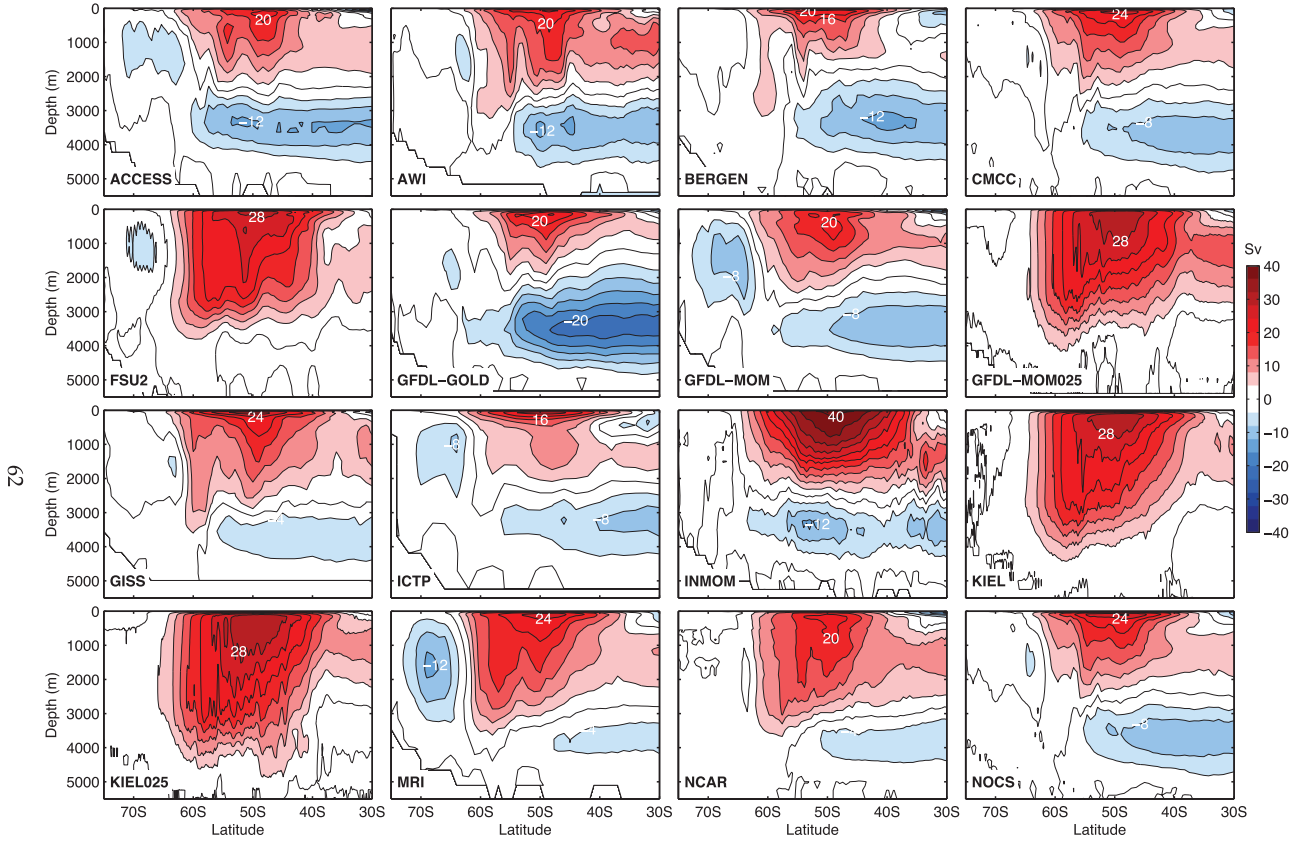
Fig. 15. The residual meridional overturning circulation (in Sv) in depth space, $\Psi_{res}(y, z)$, including, when present, the contribution from mesoscale and submesoscale parameterizations. GFDL-MOM025 and KIEL025 do not use a parameterization for mesoscale eddy-induced velocity. The residual overturning circulation in ACCESS, GFDL-MOM, GFDL-MOM025 and NCAR includes a submesoscale component. Shown is the climatological value for each model, computed as the time mean between years 1958 and 2007. Contour interval is 4 Sv and positive values denote clockwise circulations.

2012), rather than along latitude circles. The available data sets do not allow us to attempt a proper decomposition into transient and standing eddy components, and density-space Ψ_{res} will include both wind-driven and stationary eddy components. Details on the computation of the streamfunction in depth and density space are given in Appendix A.

The MOC in density-space, $\Psi_{res}(y, \sigma)$, is shown in Fig. 17, where now three main stacked cells, shown by the schematics of Fig. 16b, that can be ascribed to individual water masses are clearly visible. At the surface, the wind-driven Subtropical Cell, spreading as far south as 40 °S, transforms light subtropical waters into SAMW. Models generally produce a Subtropical Cell of 12–18 Sv, comparing well with previous estimates (Ballarotta et al., 2013; Hallberg and Gnanadesikan, 2006; Sallée et al., 2013). Below the Subtropical Cell, the Upper Cell is now depicted by the large clockwise circulation extending poleward to 60 °S. The maximum strength of the Upper Cell varies considerably across models: from 5–7 Sv in the isopycnal models (BERGEN, GFDL-GOLD) to 18 Sv (ACCESS, GFDL-MOM, KIEL). Time-mean maximum values for the Upper Cell are given in Table 3. CORE-II simulations of the Upper Cell fall within the range (12 ± 12 Sv across 32 °S) given by the Southern Ocean State Estimate of Mazloff et al. (2010).

In the densest layers, the anti-clockwise Lower Cell also varies greatly across models, from vigorous cells as in the case of AWI, BERGEN, CMCC, GFDL-GOLD and NOCS ($\sim$10 Sv, $\sim$10 Sv, $\sim$8 Sv, $\sim$15 Sv and $\sim$8 Sv, respectively) to vanishing transports in a few other models (GFDL-MOM025, FSU2, KIEL, KIEL025). Weak bottom overturning cells in the KIEL and KIEL025 models may be associated with spurious mixing due to an inadequately represented bottom water spreading. The reason for this was traced to an ineffective bottom boundary

Table 3
Residual meridional overturning circulation of the Upper Cell, Ψ_{res} (Sv). Given are the time-mean maximum values computed over the 1958–2007 period, their trends and correlations with the SAM index over the same period.

Model	Mean (Sv)	Trend (Sv decade^{-1})	Corr. SAM
1. ACCESS	18.2	2.0	0.79
2. AWI	12.8	1.5	0.44
3. BERGEN	4.8	1.5	0.65
4. CMCC	13.2	2.0	0.79
5. FSU2	9.7	3.0	0.74
6. GFDL-GOLD	7.3	1.5	0.54
7. GFDL-MOM	18.5	2.5	0.77
8. GFDL-MOM025	15.6	1.0	0.65
9. GISS	14.3	2.0	0.51
10. ICTP	12.5	3.0	0.80
11. INMOM	–	–	–
12. KIEL	18.7	2.0	0.80
13. KIEL025	16.1	1.5	0.66
14. MRI	16.7	3.0	0.94
15. NCAR	10.5	1.5	0.44
16. NOCS	11.3	2.0	0.81
MMM	13.3	2.0	0.83

layer parameterization in combination with the partial bottom cell formulation in the KIEL models. It is difficult to relate the strength of the Lower Cell to a single process. Indeed, the Lower Cell requires a proper characterization of near-shore and coastal processes, representation of downslope flows, sea-ice dynamics, topographic interactions and diapycnal mixing (Heuzé et al., 2013; Ito and Marshall, 2008; Saenko et al., 2012).
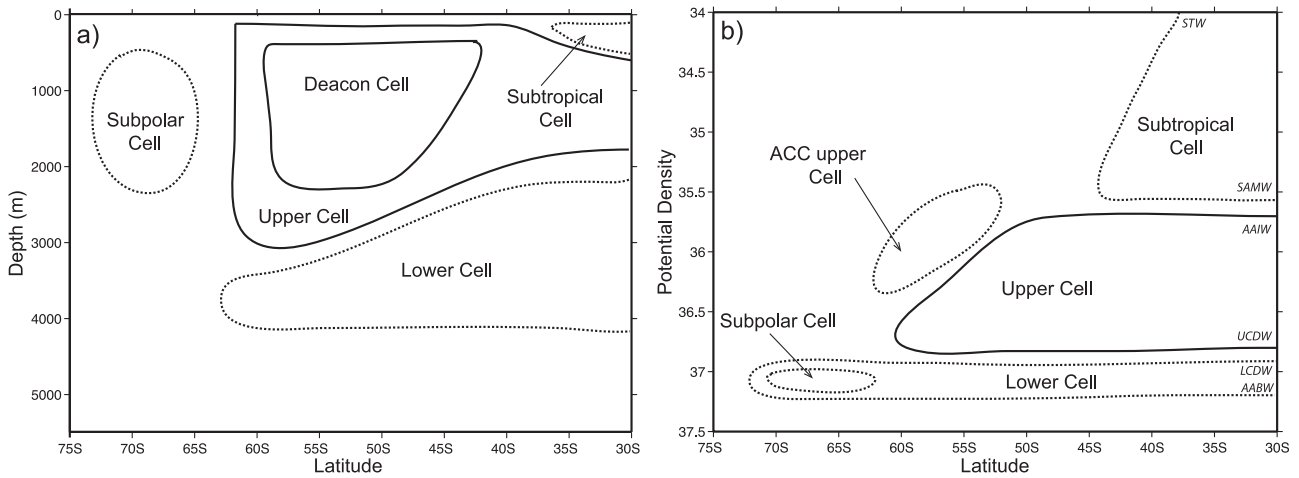
Fig. 16. Schematic showing the names and direction of flow of the main MOC cells in the Southern Ocean, as simulated by models participating in CORE-II. Solid lines are for clockwise and dotted lines for anti-clockwise circulations. (a) The cells in depth-space showing the clockwise Deacon and Upper Cells, and the anti-clockwise Lower, Subtropical and Subpolar Cells. (b) The cells in density-space, where the Deacon Cell has disappeared but an ACC anti-clockwise Upper Cell recirculates surface waters. The Subpolar Cell (a local recirculation partly fed by the Weddell and Ross Seas subpolar gyres, which in density representation is mapped into the Lower Cell) and the ACC Upper Cell (resulting from the streamfunction calculation in density classes at constant latitudes) are only present in some of the CORE-II simulations. Water masses are shown in the density-space schematic. SubTropical Waters (STW) are mostly transformed into Sub-Antarctic Mode Water (SAMW) within the Subtropical cell. The Upper Cell is made of Upper Circumpolar Deep Water (UCDW) being transformed into Antarctic Intermediate Water (AAIW). Lower Circumpolar Deep Water (LCDW) is converted into Antarctic Bottom Waters (AABW) in the Lower Cell.
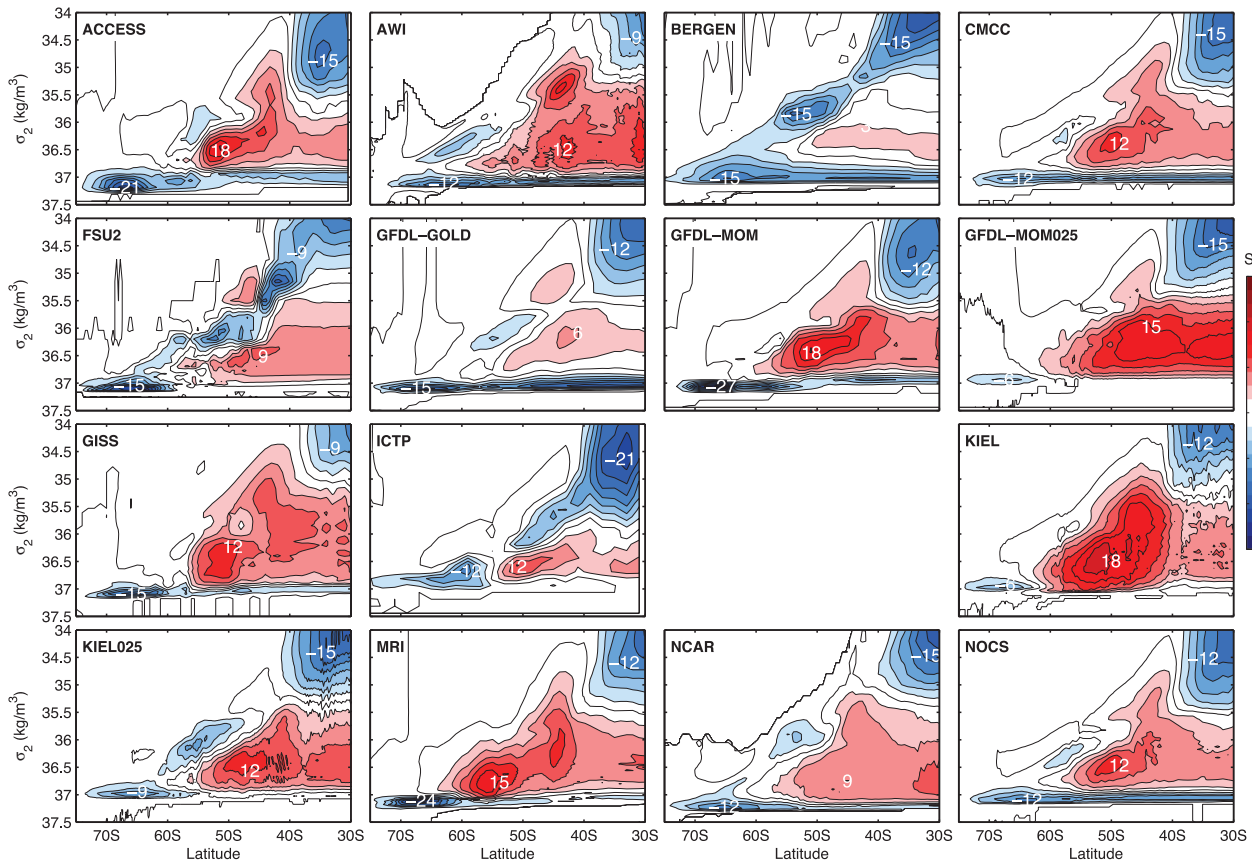

Fig. 17. As in Fig. 15 but in potential density space, $\Psi_{res}(y, \sigma)$, where the potential density coordinate is referenced to 2000 db (σ_2). The streamfunction in density-space was not provided for INMOM. Contour interval is 3 Sv and positive values imply a clockwise circulation.

Weak bottom overturning circulations were already identified in CORE-II simulations (Downes et al., 2015), and more generally in the context of coarse-resolution coupled models (Downes et al., 2011b; Sallée et al., 2013). Consistently, few CORE-II simulations of the Lower Cell fall within the range of 13 ± 6 Sv and 26.9 ± 7.6 Sv across 32 °S given by the Southern Ocean State Estimate of Mazloff et al. (2010)

and Talley (2008), respectively. In general, models tend to exhibit stronger Upper Cells and weaker Lower Cells than those estimated from observations. This feature is generated by NADW mostly forming UCDW that is eventually transformed into AAIW/SAMW, whereas the formation of LCDW and subsequent transformation into AABW is extremely weak. Observations indicate the opposite preference for
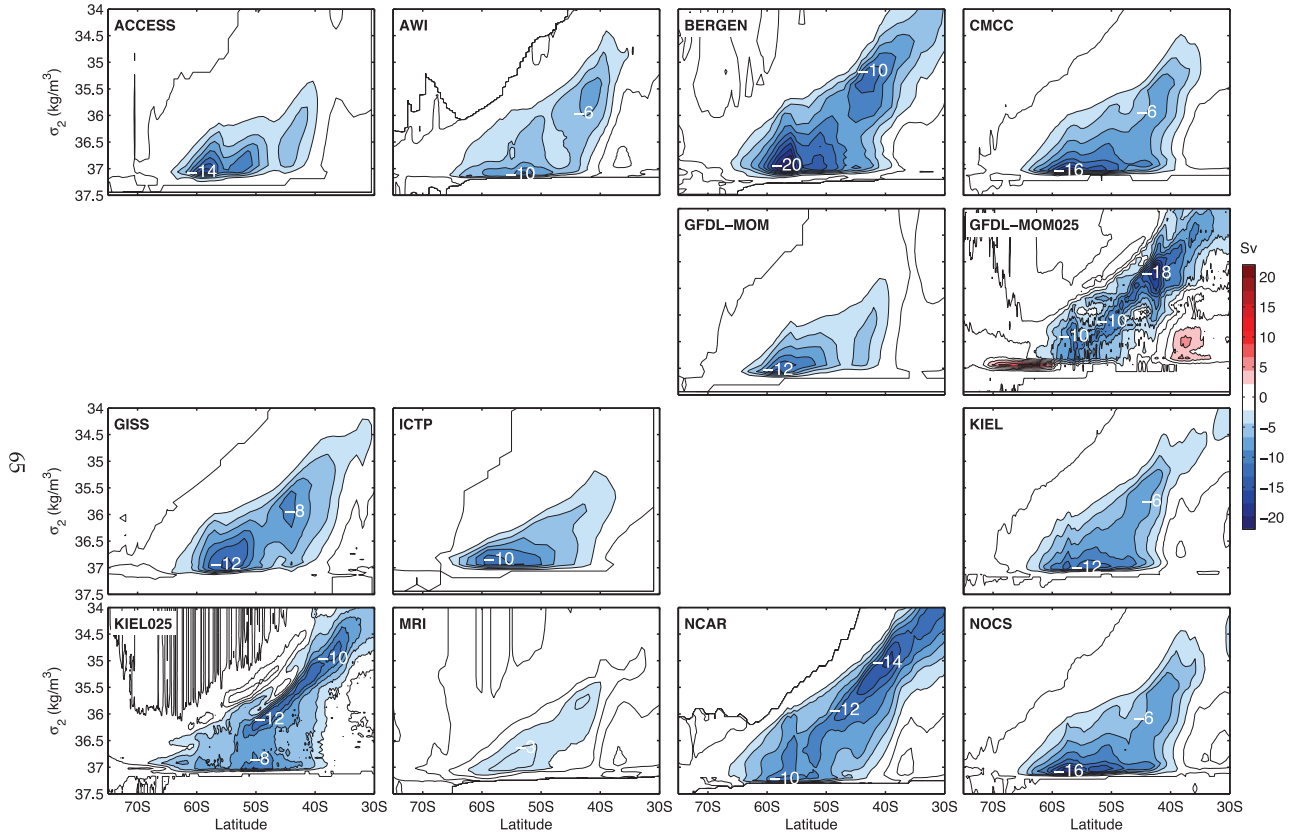
Fig. 18. The parameterized eddy-induced component of the meridional overturning circulation as a function of potential density referenced to 2000 db. The GFDL-MOM025 and KIEL025 models do not employ a parameterization for mesoscale eddy-induced velocities and the eddy-induced component of the meridional overturning circulation is extracted from the flow ($\Psi^* = \Psi_{\mathrm{res}} - \overline{\Psi}$). Contour interval is 2 Sv.

poleward flowing deep waters, i.e. most upwells south of the ACC belt contributing to the formation of bottom waters (Talley, 2008). We refer the reader to Downes et al. (2015) for an analysis of water mass properties and formation processes in CORE-II models.

Two more cells are present in some models, and both are fed by surface waters. The first is a Subpolar Cell, extending latitudinally from the Upper Cell to the Antarctic continent and between 37 and 37.25 kg m^{-3}, varying from a range of 21–27 Sv in ACCESS, GFDL-MOM and MRI to the weaker transports of GFDL-MOM025, KIEL, KIEL025 (∼6–9 Sv). The second one is roughly above the Upper Cell, centered around the ACC belt (50–65 °S), which is absent in GFDL-MOM, GFDL-MOM025, GISS, KIEL and MRI (see also Fig. 16b). This anti-clockwise upper ocean cell was identified in previous modeling studies (Dufour et al., 2012; Hallberg and Gnanadesikan, 2006; Treguier et al., 2007), and was shown to become stronger and larger when refining the horizontal resolution of the model. This is clearly the case for the KIEL and KIEL025 time-mean MOC, but the same argument does not seem to apply to the GFDL-MOM and GFDL-MOM025 streamfunctions. Treguier et al. (2007) offer an explanation for this cell, comparing its existence to the Deacon Cell, and argue that it is an artifact of the calculation in density classes at constant latitudes. As suggested in Treguier et al. (2007), integrating along streamlines, rather than zonal-averaging, would provide a more realistic picture of upper-ocean processes in the Southern Ocean.

4.1. The mesoscale and submesoscale eddy-induced meridional overturning circulation

We now look at the separate contribution from the eddy-induced overturning, Ψ^*, as shown in density-space in Fig. 18. Ψ^* was not available for all models either because (i) they are eddy-permitting

models and choose to not use a parameterization of mesoscale eddy-induced advective transport (GFDL-MOM025, KIEL025), (ii) some do not provide this diagnostic (FSU2, GFDL-GOLD) or (iii) because some do not use any parameterization for the eddy-induced advective fluxes (INMOM). We briefly introduce the mesoscale parameterizations of models participating in CORE-II in Appendix B.

We compute the density-space eddy-induced fluxes for the two eddy-permitting models, as described in Appendix A, simply by subtracting the Eulerian zonal mean component from the residual overturning ($\Psi^* = \Psi_{\mathrm{res}} - \overline{\Psi}$). Again, and consistently with our coarse-resolution models parameterizing eddy fluxes, we are not separating the contribution from standing eddies. An output with a frequency of 30 days, such as the one available in this study, has been shown to be sufficient for describing the transient eddies contribution to the eddy-induced streamfunction (see Appendix A and Ballarotta et al., 2013).

The eddy-induced circulation, spanning the latitudes 35–65 °S, partially compensates for the clockwise wind-driven circulation. The strength of Ψ^* varies from 3 Sv in MRI to 20 Sv in the isopycnal BERGEN model, and this can be largely explained by the formulation of the parameterization for mesoscale eddies and the chosen parameters (see Appendix B and Table 1 for a list of main parameters). As discussed later in Section 4.2, a three-dimensional specification for the eddy-induced advection coefficient κ or a two-dimensional κ with large upper limits will produce a larger Ψ^*.

When looking at Ψ^* in density-space, substantial differences stand out in CORE-II simulations. Starting from the two eddy-permitting models (GFDL-MOM025 and KIEL025), Ψ^* is dominated by an anti-clockwise cell, between 35 °S and 60 °S, opposing the mean clockwise Upper Cell. Within this major cell, two maxima can be identified. One extends between 30 °S and 50 °S, is near the
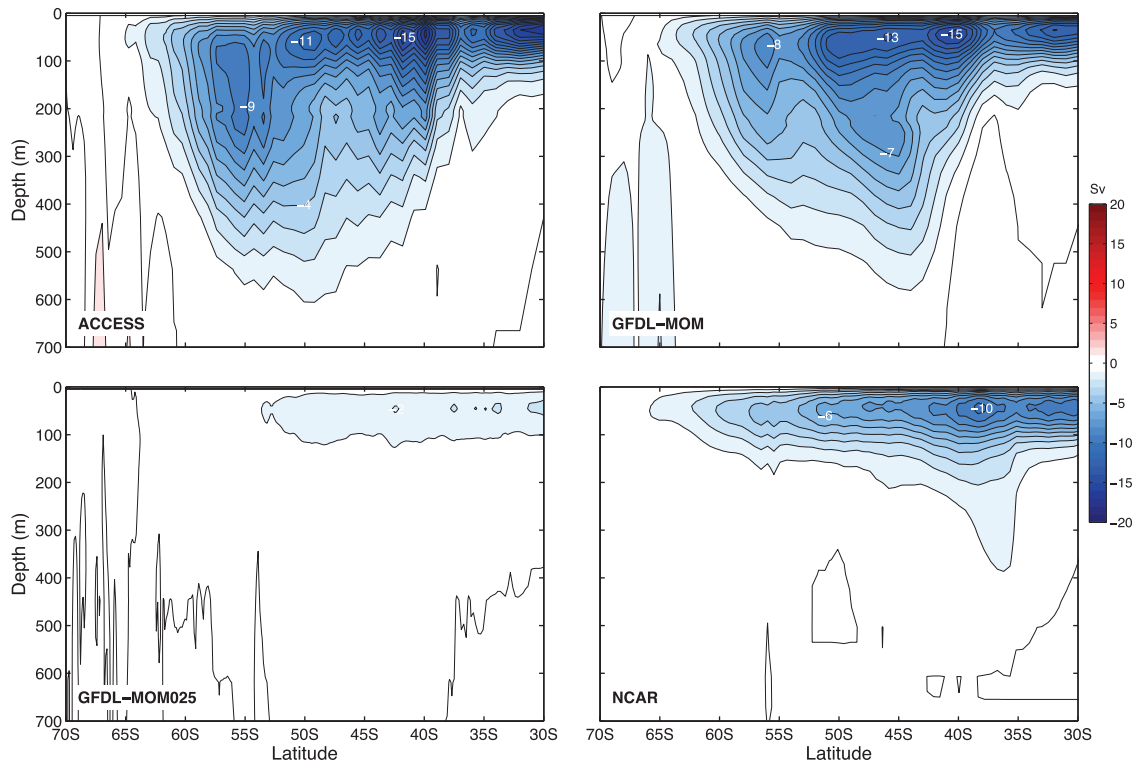
Fig. 19. The parameterized submesoscale component of the meridional overturning circulation in depth space. The submesoscale parameterization is present in ACCESS, GFDL-MOM, GFDL-MOM025 and NCAR only. Panels show only the top 800 m, as the circulation is localized in the surface mixed layers. Shown is the climatological value for each model, computed as the time mean between years 1958 and 2007. Contour interval is 1 Sv.

surface, and reaches values of 12 and 18 Sv in KIEL025 and GFDL-MOM025, respectively. The other maximum is a denser circulation, attained within the ACC latitudes (~60–50 °S), of about 10 Sv. NCAR (with a three-dimensional formulation for κ) and BERGEN (an isopycnal model) also reproduce the time-mean features observed in the eddy-permitting models, with similar magnitudes and structures. Two more models have a three-dimensional κ (AWI and GISS), but their time-mean Ψ^* is much weaker and more similar to the rest of the CORE-II simulations, which generally show a vigorous deep maximum (at $\sigma_2 = 37$ kg m^{-3}) but a much weaker surface eddy-induced circulation. The surface portion of the Ψ^* cell, compensating for most of the Eulerian-mean clockwise cell transporting NADW southward, becomes quite small in models using a constant or depth-independent diffusivity for the mesoscale parameterization, as can be observed in ICTP and MRI, and to some extent in GFDL-MOM and AC-CESS.

In the case of the eddy-permitting model GFDL-MOM025, two more clock-wise cells are identified. The first one lies between 40 °S and 30 °S, whereas the second one is in the sub-polar regions (60–70 °S). Both cells are present in previous fine-resolution models (Ballarotta et al., 2013; Dufour et al., 2012; Farneti et al., 2010), and their absence in KIEL025 might be due to the relatively low temporal sampling (30 days).

A few models (ACCESS, GFDL-GOLD, GFDL-MOM, GFDL-MOM025 and NCAR) also include a parameterization for the restratification effects of submesoscale mixed layer eddies (MLE) of Fox-Kemper et al. (2011); 2008) . More details on the MLE parameterization are given in Appendix B. Submesoscale MLE tend to restratify the upper ocean when frontal instabilities develop, slumping isopycnals through eddy buoyancy fluxes (Fox-Kemper et al., 2008). As the parameterization is formulated in terms of an overturning streamfunction, Ψ^*_{mle}, we can show the separate MLE contribution to the parameterized transport (Fig. 19; data from GFDL-GOLD is not available). Parameters such as the mixed layer depth and the buoyancy horizontal gradient will

affect the strength and vertical penetration of the MLE overturning. ACCESS, GFDL-MOM and NCAR use the same MLE parameters (see Eq. (17)), but their resulting Ψ^*_{mle} differ, particularly in the depth extension. ACCESS and GFDL-MOM, of similar resolution, produce very similar Ψ^*_{mle}, both in terms of magnitude and vertical extent. However, NCAR shows a much weaker and shallower submesoscale contribution. This can be partly explained by their respective mixed layer depths, being deeper than observed in ACCESS and GFDL-MOM and shallower than observed in the NCAR model (Downes et al., 2015).

A different explanation is needed for the time-mean Ψ^*_{mle} in GFDL-MOM025. The numerical implementation of the MLE parameterization differs in GFDL-MOM025, as unphysical solutions and instabilities were discovered after substantial testing of the scheme. As problems were exacerbated at fine resolution, the numerical scheme was reformulated and parameters were changed in order to reduce the overall impacts of MLE. More details can be found in Appendix B9. Except for GFDL-MOM025, Fig. 19 shows that Ψ^*_{mle} submesoscale restratification parameterization scheme does contribute significantly to the net overturning in the upper layers.

4.2. The eddy-induced advection coefficient

The importance of a time-varying and vertically-dependent κ has been the subject of recent studies (Bryan et al., 2014; Gent and Danabasoglu, 2011; Hofmann and Maqueda, 2011; Kuhlbrodt et al., 2012; Viebahn and Eden, 2010). However, to date, most global ocean models are far from implementing a fully spatially and time-varying κ in their GM-like parameterizations [see tables in Farneti and Gent, 2011; Kuhlbrodt et al., 2012], resulting in major drawbacks particularly in the representation of Southern Ocean responses to climate change, heat uptake and its impact on the carbon cycle (Farneti and Gent, 2011; Kuhlbrodt et al., 2012; Meredith et al., 2012).

The time-mean κ in the Southern Ocean is given in Fig. 20. The value of κ at 300 m depth is given for those models that parameter-
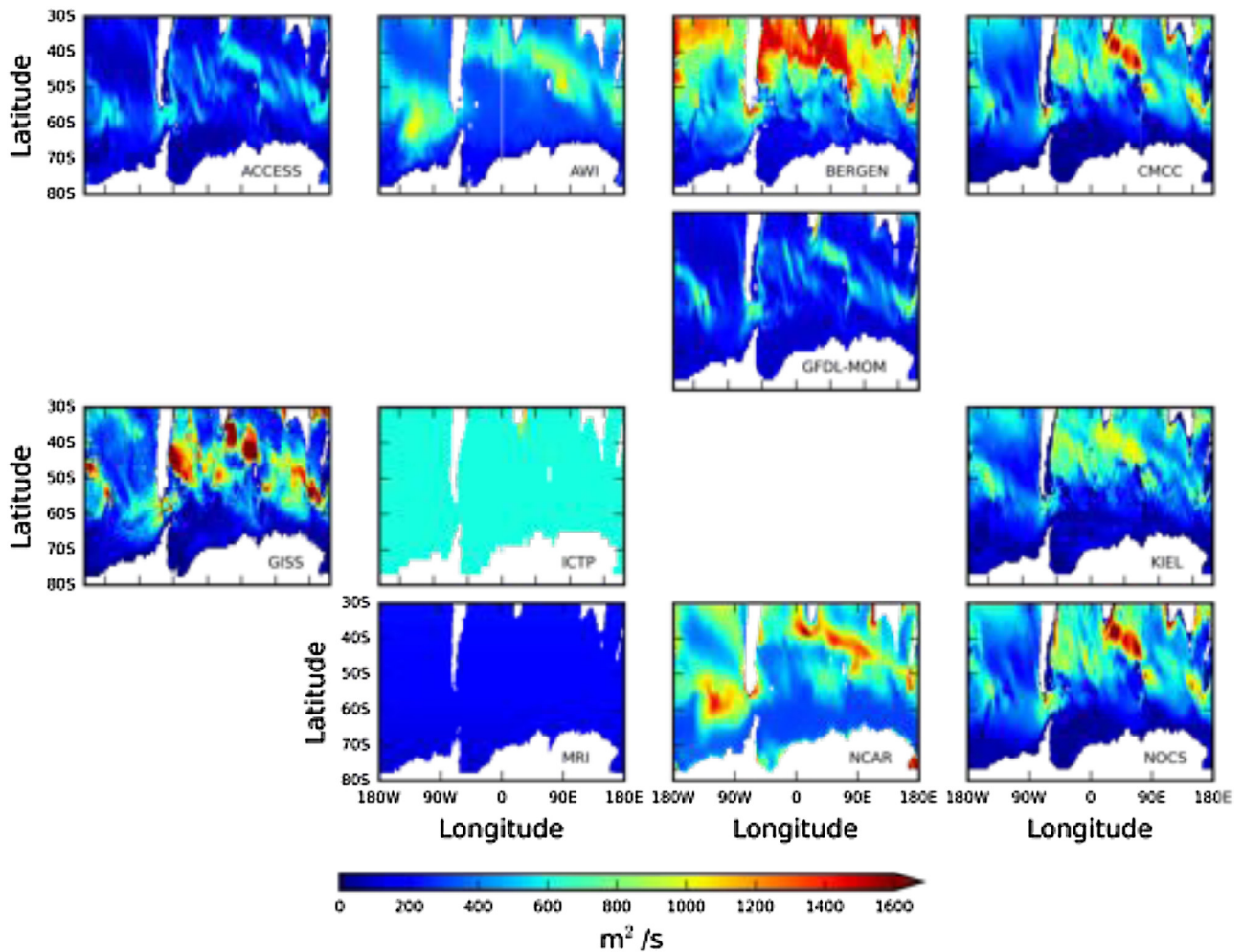
Fig. 20. The time-mean eddy-induced advection coefficient (κ, in m^2 s^{-1}). Shown is the climatological value computed as the time mean between years 1958 and 2007. For those models having a depth-dependent κ (AWI, BERGEN, GISS and NCAR), the value at 300 m depth is shown.

ize κ as a function of depth (AWI, BERGEN, GISS and NCAR). The depth of 300 m was chosen in order to be outside of at least the time-mean surface diabatic layer, where both NCAR and AWI do not use κ, and Ψ^* linearly goes to zero. κ is spatially and temporally constant in MRI and absent in the eddy-permitting models GFDL-MOM025 and KIEL025. Modelled time-mean values are enhanced in regions of large baroclinic instabilities and eddy kinetic energy (EKE), with larger values in the Agulhas region, western boundary currents and along the ACC path (Abernathey and Marshall, 2013; Eden, 2006; Marshall et al., 2006; Sallée et al., 2008). The dependency of Ψ^* on κ is illustrated in Fig. 21 where the time-mean averaged strength of Ψ^* in density space is plotted against the time-mean averaged value of κ. Fig. 21 shows a strong linear correlation between Ψ^* and κ, with Ψ^* increasing from the fixed κ formulation in MRI (black symbol) to the time-dependent two-dimensional κ formulations (blue symbols) and finally attaining the largest values with time and depth-dependent κ implementations (red symbols). The only outlier is ICTP, possibly because its lower bound on κ is set to the largest value across the models but produces only a modest Ψ^*.

How to determine and prescribe the depth dependence of mesoscale eddy diffusivity remains an open science question; the small number of parameterizations that do have a vertical dependent κ thus vary greatly. Following Ferreira et al. (2005), NCAR has proposed a buoyancy frequency (N) dependent diffusivity (Danabasoglu and Marshall, 2007), and the same approach has been adopted here by AWI. GISS is instead using a diffusivity that decays with depth pro-

portionally to the mesoscale kinetic energy (Canuto and Dubovikov, 2006). Finally, κ in BERGEN is dependent on eddy length and time scales related to the EKE, implemented according to Eden and Greatbatch (2008).

The time-mean and zonally-averaged κ of AWI, BERGEN, GISS and NCAR are shown in Fig. 22. In all four models κ is higher at the surface with values between 600 and 1200 m^2 s^{-1}, rapidly decaying with depth to values around 400 m^2 s^{-1} at 1500 m depth. The surface value is around the canonical one used in global ocean models. However, as most models so far have considered a depth-independent κ, it is clear that subsurface values differ substantially in those including a z-dependency. Not only depth dependent κ formulations have been shown to provide a more accurate representation of local eddy fluxes throughout the water column, but they also have been associated with improvements in the representation of some oceanographic features and in the response to variable surface forcings (Bryan et al., 2014; Danabasoglu and Marshall, 2007; Eden et al., 2009; Gent and Danabasoglu, 2011; Hofmann and Maqueda, 2011). Fig. 21 also suggests a clear influence of depth varying formulations on the strength of Ψ^*. However, we only present results from four models employing a three-dimensional κ and the climatological value of Ψ^* also depends on the limits imposed when using a two-dimensional κ (as shown by the blue symbols in Fig. 21).

In partial agreement with recent observations and numerical estimates of surface diffusivities (Eden, 2006; Marshall et al., 2006), κ attains larger values in the northward flank of the ACC and weaker
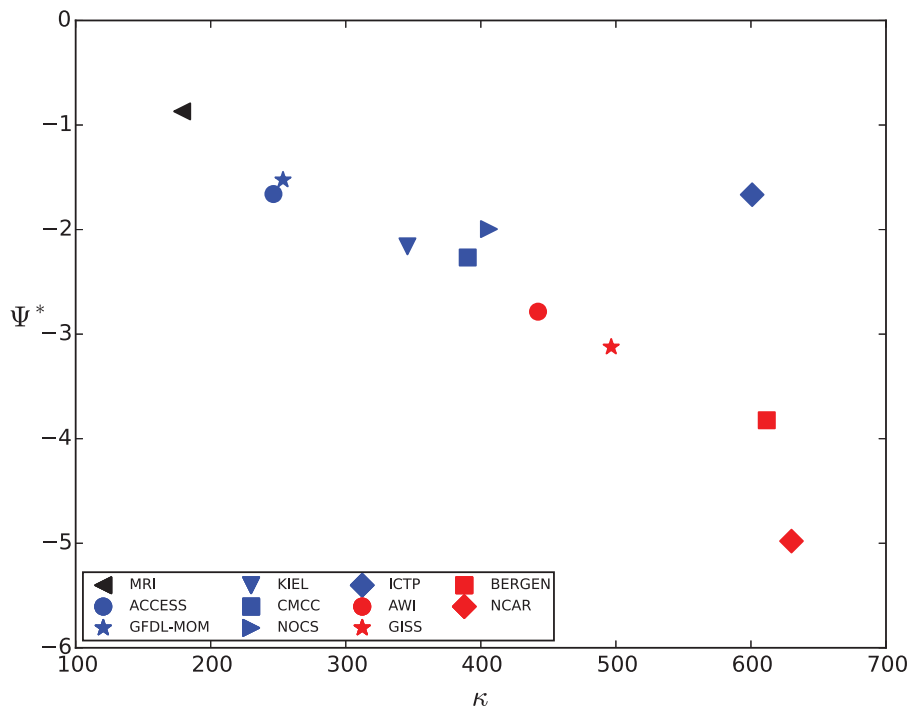
Fig. 21. The averaged strength of the eddy-induced component of the meridional overturning circulation in density space (Ψ^*, in Sv; averaged latitudinally between 70°S and 35°S and over the densities 34.5–37.5 kg/m^3) against the averaged eddy-induced advection coefficient (κ, in m^2/s; averaged latitudinally between 70°S and 35°S). Red symbols: models having a time and depth-dependent κ (AWI, BERGEN, GISS and NCAR; values computed at 300 m depth); blue symbols: time-dependent but vertically independent κ; black symbol: fixed κ. (For interpretation of the references to colour in this figure legend, the reader is referred to the web version of this article.)
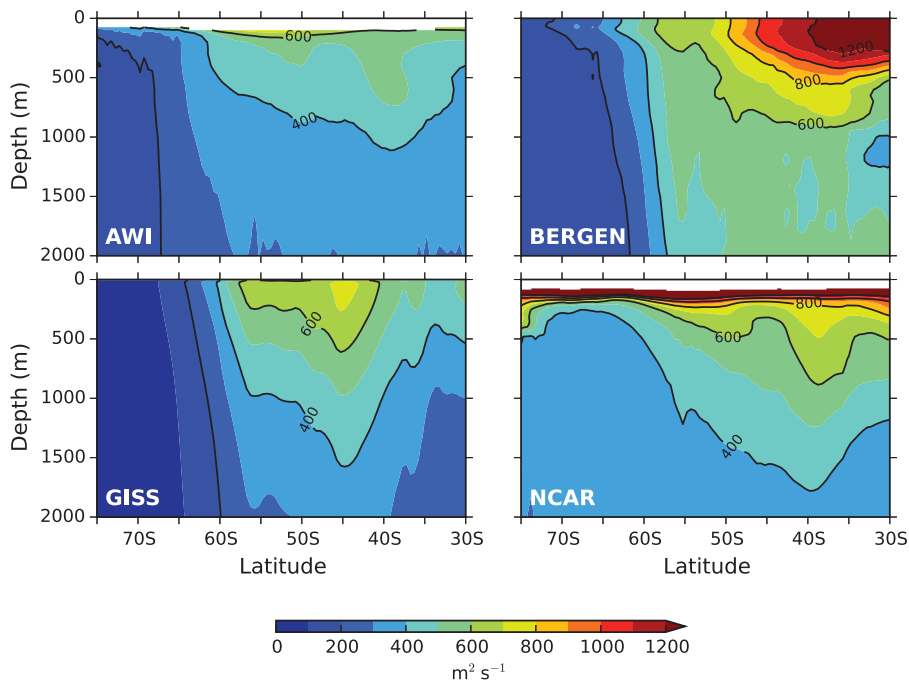

Fig. 22. The time-mean zonally averaged eddy-induced advection coefficient (κ, in m^2 s^{-1}) for those models where κ is depth-dependent. Shown is the climatological value computed as the time mean between years 1958 and 2007. Contour interval is 200 m^2 s^{-1}. In AWI and NCAR, κ values at depths shallower than the mean diabatic layer thickness are masked as only interior values are used for the calculation of the eddy-induced stream function.

values poleward of the polar front, as seen in the zonally averaged profile at 300 m depth shown in Fig. 23. All models have $\kappa \approx 100$–400 m^2 s^{-1} poleward of 60 °S, κ increases to 400–700 m^2 s^{-1} within the ACC core and reaches the largest values of 600–900 m^2 s^{-1} equatorward of the ACC. The general meridional structure is thus well captured by these models, although peak values seem too

weak compared to the literature that suggests values as high as 2000 m^2 s^{-1} (Eden, 2006; Marshall et al., 2006). Arguably, even though progress has been made with a depth dependent formulation, even the choice of parameter values within the same parameterization can result in non-trivial differences (compare AWI and NCAR in Fig. 23).
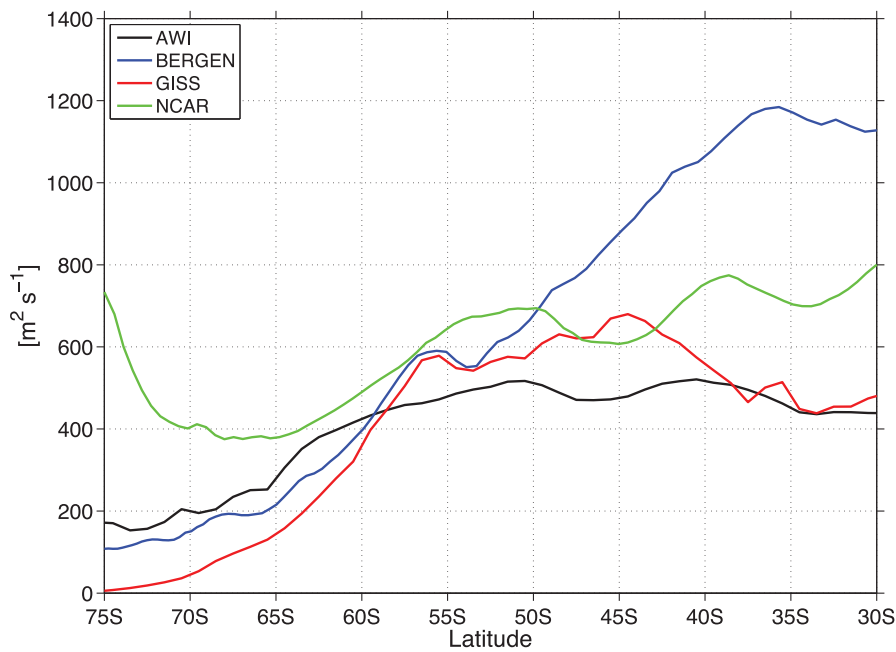
Fig. 23. The time-mean (1958–2007) zonally averaged eddy-induced advection coefficient κ (m^2 s^{-1}) at 300 m depth for models including a depth dependent κ.

4.3. Trends over years 1958–2007

There are no observations of the MOC in the Southern Ocean, which contrasts to the North Atlantic MOC (AMOC), which now has roughly ten years of measurements at 26.5 °N from the RAPID array (Johns et al., 2011). Therefore, producing an observation-based index of the Southern Ocean MOC is not possible. Nonetheless, model-model comparisons are of use to determine how CORE-II simulations simulate the evolution of the Southern Ocean MOC during the period 1958–2007.

Fig. 24 shows the decadal trends of the residual MOC in density space. All models reveal strengthening trends for the Upper Cell, but with different magnitudes. Larger trends are found for FSU2, MRI, ICTP and GFDL-MOM attaining values up to 3 Sv/decade in FSU2 and ICTP, and we note that these models have already been identified as having crude mesoscale parameterizations. Eddy-permitting models or those employing a time-varying three-dimensional formulation for κ such as AWI, BERGEN, GFDL-MOM025, KIEL025 and NCAR have the weakest Upper Cell averaged trends, between 0.5 and 1.5 Sv/decade. GFDL-GOLD, although using a depth-independent κ, also presents weak trends. Many models also exhibit considerable trends towards an intensification of the Sub-polar Cell, this being a surface wind-driven cell, as shown by ACCESS, AWI, CMCC, GFDL-MOM, GISS, MRI and NCAR. This behavior should not be misinterpreted as a strengthening of the Lower Cell, which is not experiencing a significant trend in any of the models. Rather, the trend represents an intensification of a local Southern Ocean recirculation, as clearly no 'deep' trends are observed equatorward of the ACC. In any case, the representation of the Lower Cell in CORE-II simulations is not sufficiently accurate as to draw any conclusion on its evolution (see also Downes et al., 2015).

Trends in the eddy-induced overturning Ψ^* largely explain the differences found in the residual trends, and they are shown in Fig. 25. Here, it is evident that models participating in CORE-II respond differently to changes in surface forcing (mostly a strengthening of surface zonal winds, as seen in Fig. 2). The two eddy-permitting models have large Ψ^* trends (0.5 Sv/decade), encompassing the whole Upper Cell latitudinal and density range (GFDL-MOM025 and KIEL025 in Fig. 25). BERGEN and NCAR also show large Ψ^* trends, but more

confined in latitude within densities of the Upper Cell. Both AWI and GISS have less spatially coherent changes in Ψ^*, consistent with the modelled trends in their residual circulations. The remaining CORE-II simulations show very modest eddy-induced circulation sensitivities, resulting in significant residual Upper Cell trends (see Table 3).

The inter-model differences in evolution of eddy induced streamfunction can be ascribed to both the choice of closure and parameters limiting the growth of the eddy-induced transport. A clear example is given by AWI and NCAR that, using the same mesoscale closure, results in very different Ψ^* because of different responses in their κ. This behavior is illustrated in Fig. 26, where decadal trends in thickness diffusivity are shown. AWI, although behaving similarly to NCAR and showing κ strengthening along the northern flank of the ACC, has considerably weaker trends. Indeed AWI, although using a relatively large value for the maximum slope S_{max}, has adopted a lower upper bound for κ than NCAR (see Appendix B and Table 1 for the actual values). This restriction on the AWI implementation of the mesoscale eddy parameterization reduces the degree to which its parameterized eddy-induced circulation, Ψ^*, can respond to changes in baroclinicity.

The choice of parameter values also affects the depth penetration of the trends (Fig. 27), with NCAR showing significant trends down to 2000 m whereas trends in AWI only reach 1000 m depth. BERGEN and GISS also have large areas of significant κ trends (Fig. 26), but they differ in the vertical (Fig. 27) where they both relate κ to the local buoyancy frequency N but with rather different approaches (again, see Appendix B). We note that BERGEN and NCAR are not employing the largest range in κ values, as the cap is placed at 1500 (3000) m^2 s^{-1} for BERGEN (NCAR), when other models can in principle reach up to 5000 m^2 s^{-1} (CMCC and NOCS; see Table 1). It is the large subsurface κ values (Fig. 22) and trends (Fig. 27) that are consistent with and responsible for the Ψ^* trends seen in Fig. 25, and their subsequent relatively modest trends in Ψ_{res}. It is unfortunate that GFDL-GOLD did not produce the Ψ^* and κ diagnostics, but given its weak trends in Ψ_{res} we can only speculate that the same argument is true for GFDL-GOLD. Although to a smaller extent, the depth-dependence in the κ formulation is also crucial for the behavior of AWI and GISS.
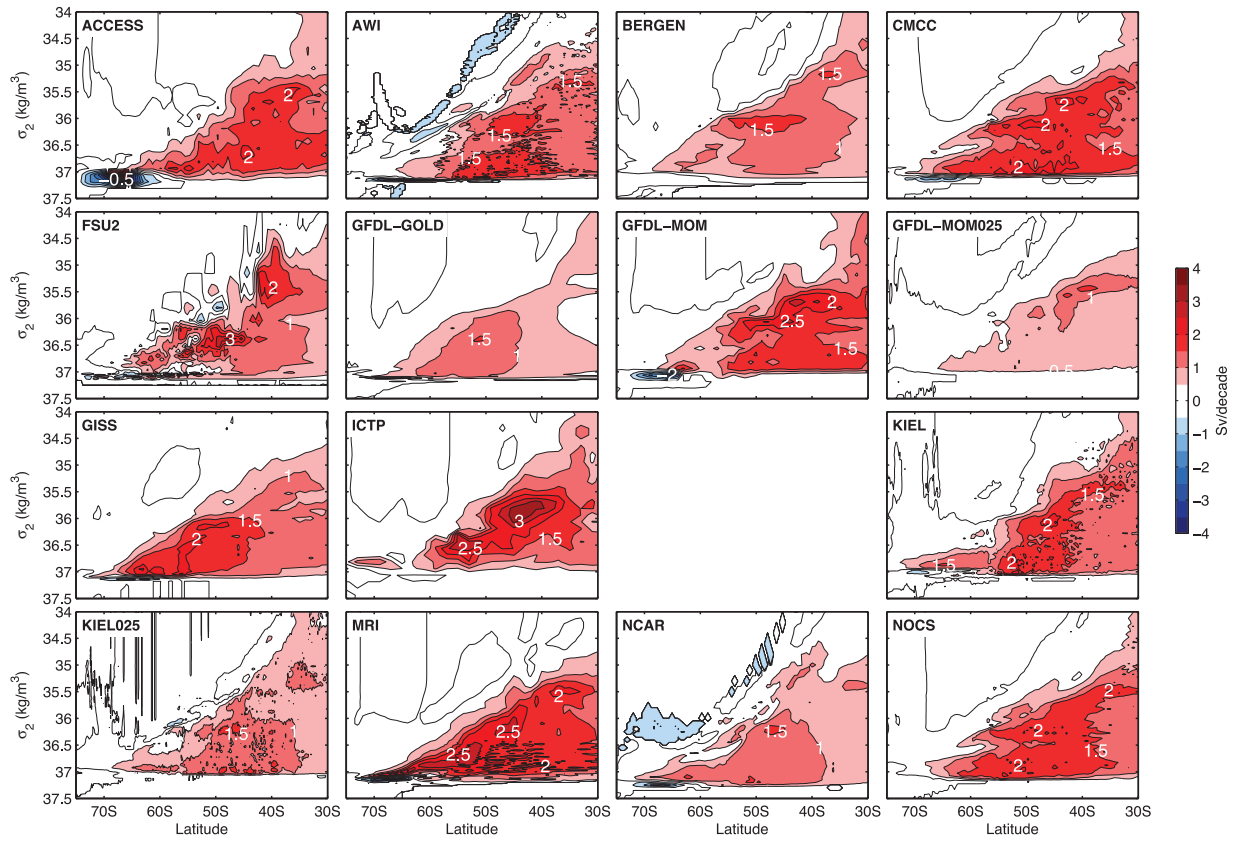
Fig. 24. Linear decadal trend (Sv decade^{-1}) of the zonally-averaged residual meridional overturning circulation (Ψ_{res}) for the years 1958–2007. Contour interval is 0.5 Sv decade^{-1}.
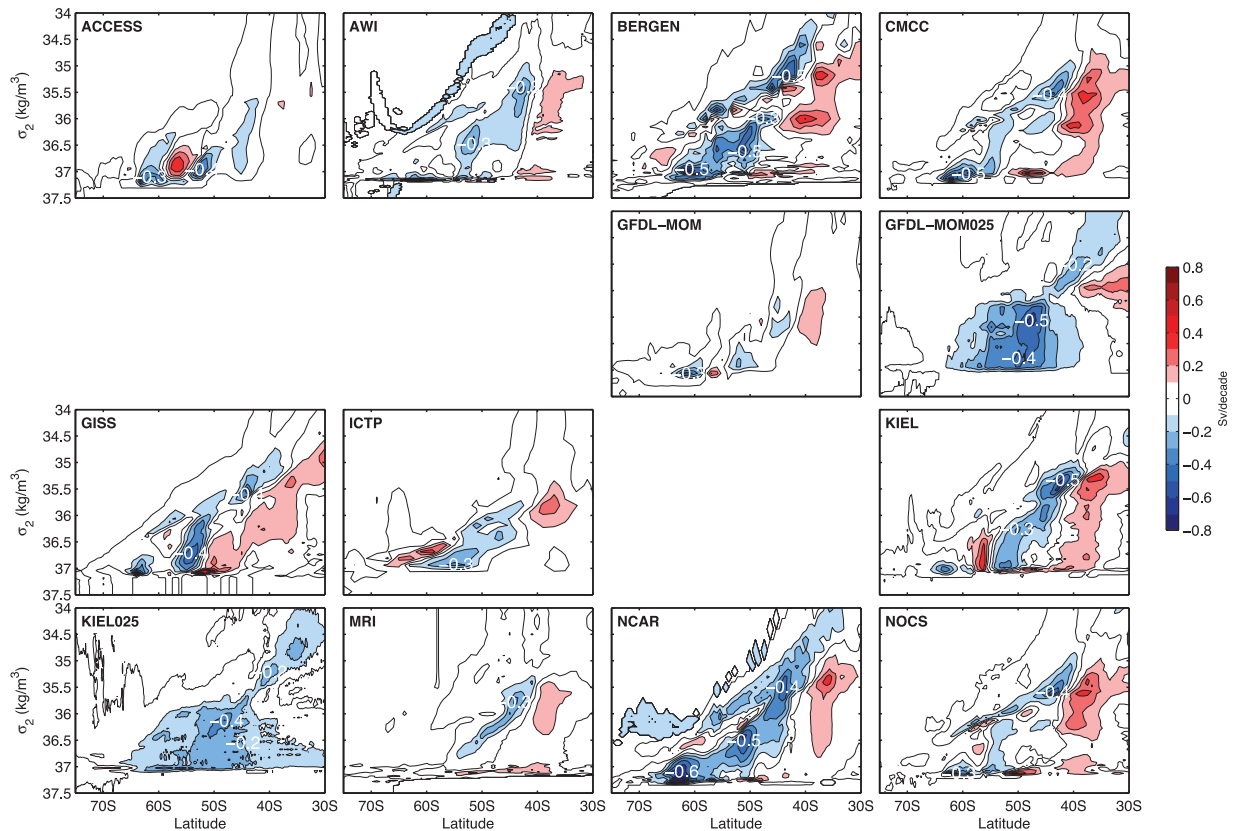

Fig. 25. Linear decadal trend (Sv decade^{-1}) of the zonally-averaged eddy-induced meridional overturning circulation (Ψ^*) for the years 1958–2007. Contour interval is 0.1 Sv decade^{-1}.
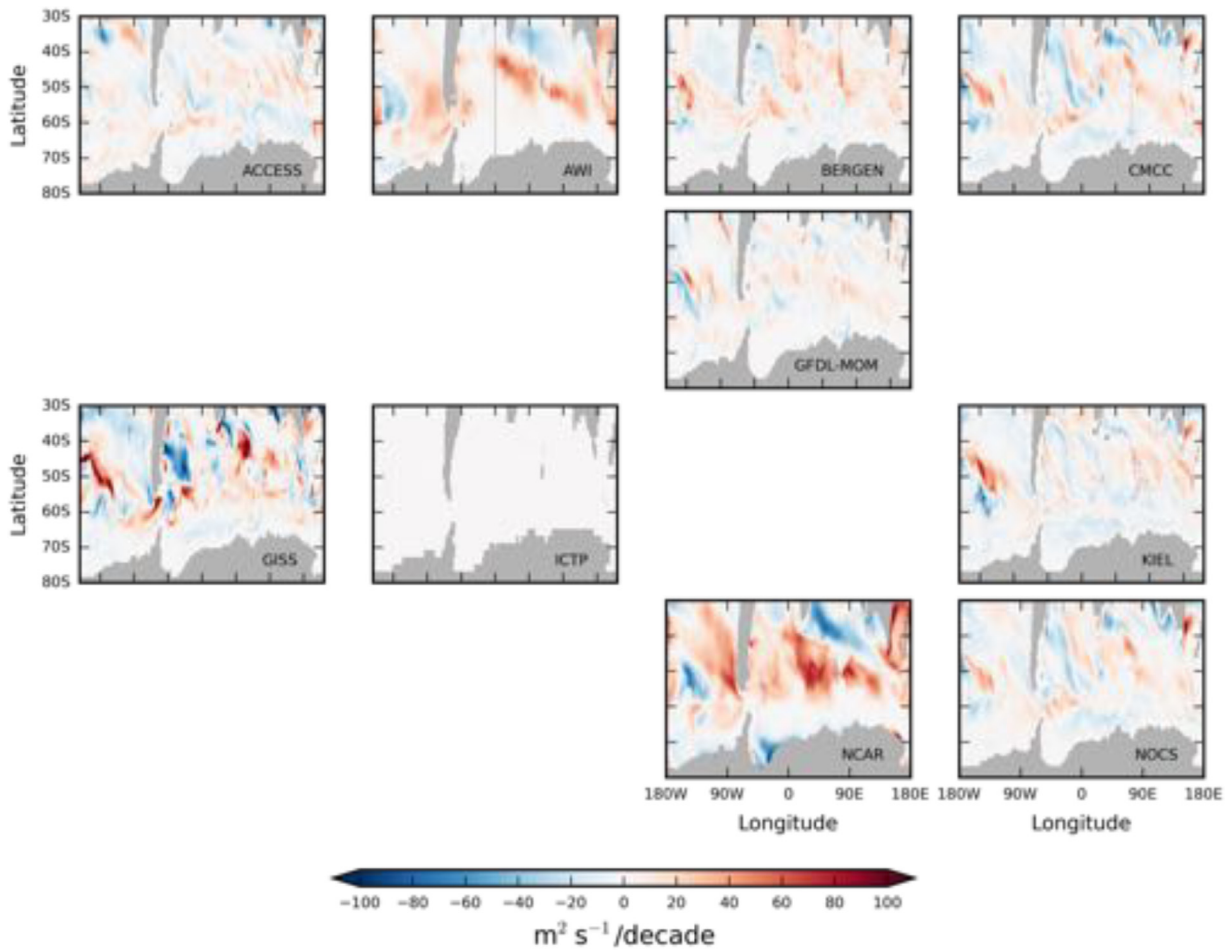
Fig. 26. Eddy-induced advection coefficient κ linear decadal trend (m^2 s^{-1}/decade) for the years 1958–2007. For those models having a depth-dependent κ (AWI, BERGEN, GISS and NCAR), the value at 300 m depth is shown.
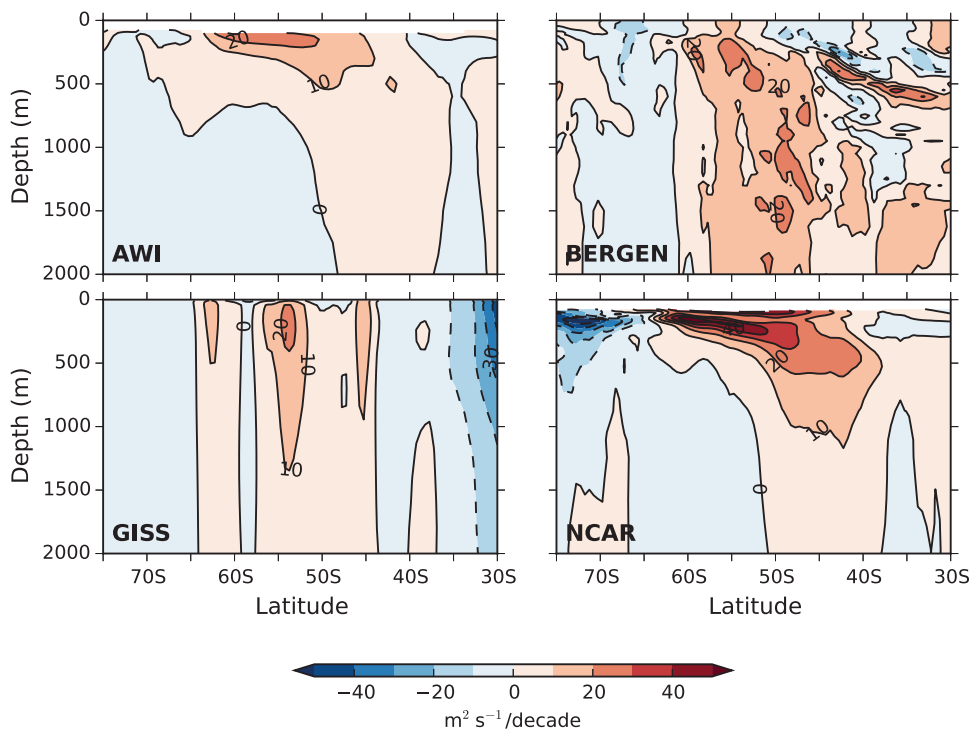

Fig. 27. Linear decadal trend (m^2 s^{-1}/decade) of the zonally-averaged eddy-induced advection coefficient (κ) for the years 1958–2007 and for those models where κ is depth-dependent.
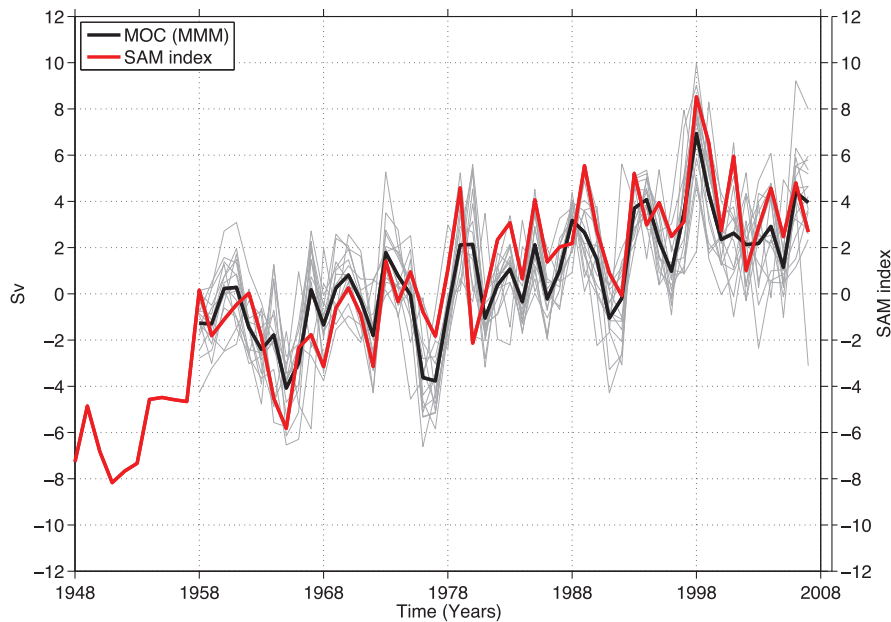
Fig. 28. The multi-model-mean (MMM) residual MOC transport anomalies (with respect to the 1958–2007 mean; in Sv) are shown by the black line, gray lines refer to individual models transport anomalies, and the SAM index is shown by the red line. The MMM-SAM correlation is 0.67. (For interpretation of the references to colour in this figure legend, the reader is referred to the web version of this article.)

4.4. The MOC and the SAM

As in Fig. 14, we plot the SAM index against the maximum residual Upper Cell transport annual-mean anomalies computed in density space, and show individual time series and their MMM in Fig. 28. Treguier et al. (2010) find that the Eulerian-mean MOC is highly correlated ($r = 0.79$) with the SAM, and that the residual MOC Ψ_{res} is also highly correlated with $\overline{\Psi}$, showing similar trends for the period 1972–2001. Within the analyzed CORE-II period, from 1958 to 2007, the MMM correlation with the SAM is 0.67, with individual members ranging from 0.94 (MRI) to 0.44 (AWI and NCAR). A comprehensive list of correlation coefficients is given in Table 3. Here, as in Treguier et al. (2010), CORE-II simulations are found to be highly correlated with the SAM at interannual time scales, both with their mean and residual circulations, but with some remarkable differences. Correlations are found to be weaker for those models with more responsive eddy fluxes (AWI, BERGEN, GFDL-GOLD, GFDL-MOM025, GISS, KIEL025 and NCAR; for this subset of models the correlation is only 0.56). Conversely, models whose Ψ^* is not sufficiently sensitive to changes in surface forcing have higher correlations ($r = 0.82$ when considering only ACCESS, CMCC, GFDL-MOM, ICTP, KIEL, MRI and NOCS).

As in Treguier et al. (2010), and although the eddy contribution to the MOC does show a considerable trend in some of the CORE-II simulations, we found no significant correlations between Ψ^* and the SAM. Finally, we can conclude that wind forcing, and the SAM in particular, largely determines the evolution of the MOC Upper Cell on interannual time scales in CORE-II simulations, as previously suggested in similar modeling studies (Dufour et al., 2012; Treguier et al., 2010).

5. Summary and discussion

In this paper, and its companion (Downes et al., 2015), we have presented an analysis of the representation of Southern Ocean properties from seventeen global ocean-sea ice models participating in the CORE-II intercomparison project. In Downes et al. (2015), a focus was placed on mixed layer depth, sea ice and water mass properties during the period 1988–2007. Here, we have instead considered the representation of the Antarctic Circumpolar Current (ACC) and Southern Ocean Meridional Overturning Circulation (MOC) by the participating models, and their evolution during the 1958–2007 period.

Although the large majority of models showed quasi-equilibrated ACC transports, with a good reproducibility between the fourth and fifth forcing cycles, some other models presented drifts that compromised the ACC evolution during the cycle. Generally, modelled ACC transports were too strong compared to recent observations, but within values from CMIP multimodel means. The too-strong Drake Passage transport could be due to model parameters and biases, overly strong CORE-II winds, or both. Modest decadal trends were also found, with transports strengthening < 9% whereas westerlies increased about 30% during the same period.

Despite the general agreement, simulations clustered into two main groups. Models with constant or two-dimensional eddy-induced coefficient κ responded strongly to surface forcing changes (the mean trend for these models is 3.0 Sv/decade), whereas eddy-permitting models or models with a three-dimensional κ showed weaker transport and isopycnal slope trends (2.4 Sv/decade mean ACC trend; see also Table 2), suggesting a greater eddy saturation. The clustering can also be visualized in Fig. 13 where eddy-permitting models and models with a three-dimensional κ are plotted with black filled symbols and they show the weakest trends in ACC and $\Delta\rho$. KIEL and ICTP also show weak decadal trends but, as previously discussed, their behavior is characterized by a drift in ACC transport.

Hallberg and Gnanadesikan (2001) suggested that the ACC transport is linearly related to wind stress in the weak wind forcing case (the buoyancy-dominated regime), whereas in the strong wind forcing case (the eddy-dominated regime) mesoscale eddy activity is excited and, as a result, the ACC is largely insensitive to wind changes (i.e. eddy saturated). Westerlies have indeed strengthened and shifted polewards during the second half of the 20th century. However, changes in both magnitude and latitude of winds have not been as dramatic here as previous idealized cases seeking the response of coarse- and finer-resolution models, possibly explaining the relatively small differences between CORE-II simulations in terms of eddy saturation.

There is a high interannual correlation between CORE-II ACC transports and the SAM. Conversely, results indicate that the ACC

is not exhibiting a significant decadal trend in most CORE-II simulations, as suggested in modeling (Treguier et al., 2010; Yang et al., 2007) and observational (Böning et al., 2008) studies. Correlations with individual models were found to be higher than previous modelled estimates (Treguier et al., 2010; Yang et al., 2007). The larger SAM trend present in the CORE-II winds used in this study might be responsible for the higher MMM interannual correlation and the overall ACC trends. CORE-II winds presenting substantial momentum forcing changes and trends serves us as an ideal test for the sensitivity of the Southern Ocean during the simulated period in the CORE-II simulations. It is useful to recall that forcing data sets in CORE-II include surface buoyancy changes, so that the evolution of the ACC and the whole Southern Ocean during the period 1958–2007 could also be partly guided by changes in surface heat and freshwater fluxes and, as a result, the correlation with the SAM index would be modified. This is the case, for example, in coupled climate model simulations of the 21st century, where the linear relationship between ACC transport and SAM index is not present in all models (Wang et al., 2011), suggesting that other factors are also playing a role in decadal ACC trends (see also Sen Gupta et al., 2009; Meijers et al., 2012).

Our results are consistent with Dufour et al. (2012), where only a marginal difference in ACC transport sensitivity to SAM anomalies was found between models of 0.5° (56 km at 60 °S) and 0.25° (28 km at 60 °S) horizontal resolution. The response of fully eddy-resolving global models is not yet known. However, idealized studies have shown that the sensitivity of finer-resolution models (ranging from 1/4° to 1/16°) to the strength of wind forcing approaches the fully saturated state (Morrison and Hogg, 2013; Munday et al., 2013), with increases in ACC transport of ~10–20% for a doubling of wind stress, consistent with eddy-permitting model results (Farneti et al., 2010; Hallberg and Gnanadesikan, 2006). Significant differences do exist between models participating in CORE-II, ranging from coarse to eddy-permitting, when the long-term trends are considered, with some models responding more readily to decadal trends in both momentum and buoyancy forcing, as seen in Table 2.

Variability in ACC strength is mostly governed by zonal momentum balance, its associated sloping isopycnals and baroclinic thermal wind transport. CORE-II simulations seem to support the dominance of a baroclinic mode in the low-frequency variability of the ACC (Fig. 13). However, Hughes et al. (1999) proposed the existence of a barotropic, free-mode mechanism for ACC transport variability, whereby wind stress fluctuations along closed f/H contours (where f is the Coriolis parameter and H the ocean depth) around Antarctica can force accelerations in transport. More recently, eddy-permitting ocean–sea ice simulations showed that the free-mode mechanism is indeed capable of driving significant changes in ACC transport (Langlais et al., 2015; Zika et al., 2013b). An assessment of the relative role of 'along-ACC' and 'along-f/H' wind stress variability in setting the ACC transport, and the consequences for eddy-saturation, is left for a future study.

Eddy saturation relates the sensitivity of the ACC transport to changes in wind stress only, and therefore does not apply to surface buoyancy anomalies. It is not easy to predict the way surface heat and freshwater fluxes will contribute to upper-ocean stratification changes – and their link with momentum forcing through the turbulent fluxes – as the solution is dependent on the meridional structure of the surface anomaly and, unfortunately, on the model used. Buoyancy forcing might be as important as, if not dominate over, momentum trends in 21st century simulations (Downes and Hogg, 2013), and certainly plays an important role in setting the mean transport (Hogg, 2010).

We can try to roughly estimate the relative role of momentum and buoyancy fluxes by forcing our models with only momentum flux anomalies (experiment WIND; where only wind components vary interannually), or with buoyancy flux anomalies only (experiment BUOY; where all forcing vary interannually, except for winds

that are kept at their climatological state). This approach suppresses the variability in the momentum or buoyancy forcings, but not their influence on the surface fluxes. In fact, all of the turbulent fluxes depend on the wind speed, since differences between the atmospheric and oceanic state are taken into account by the bulk formulae when computing surface fluxes, including heat and freshwater. Hence, wind anomalies will impact buoyancy fluxes. More appropriate flux perturbation experiments have been performed by Yeager and Danabasoglu (2014), where climatological or interannual winds are used in the bulk formulae for heat and freshwater fluxes, depending on the experiment, so properly isolating the momentum-forced and buoyancy-forced interannual variability. Another possible approach would be to isolate the wind impact by just modifying the wind stress felt by the ocean as in Farneti et al. (2010). Keeping in mind these caveats, we use the ICTP model to run a WIND and a BUOY sensitivity experiment, and repeat the integrations for five repeating cycles of the 60-year forcing (300 years). Fig. 30 shows the ACC evolution under standard CORE-II (FULL), WIND and BUOY surface forcings. As expected, all of the interannual variability and trend in the transport is governed by the momentum forcing, with buoyancy forcing mainly responsible for a long term downward drift and a flattening of the isopycnals (not shown) leading to a reduction in transport. Insofar as the ICTP coarse-resolution model and the simple approach adopted here for the forcing separation can convey a proper characterization of the Southern Ocean response to forcing variability, our results strengthen the idea of a dominant role of momentum flux variability over the ACC trend during the 1958–2007 period.

The second focus of this paper was on the representation of the Southern Ocean MOC in CORE-II simulations. Both time-mean and linear trends were examined for the period 1958–2007. Particular attention was given to the eddy component of the overturning circulation. Models that parameterize mesoscale eddies were analyzed not only in terms of their transports, Ψ^*, but also based on their parameterization, which is most easily classified in terms of the eddy-induced advection coefficient κ.

For a proper representation of the net transport of water masses we computed the MOC in potential density space. Similarly to the ACC, a wealth of different transports was simulated and differences were attributed to the eddy-induced circulation Ψ^* that, in the case of models employing a mesoscale parameterization, is largely controlled by the formulation of κ. The time-mean Ψ^* varies greatly in terms of magnitude and spatial extent. Models including a three-dimensional formulation of the diffusivity κ were found to have larger eddy-induced transports, and a spatial structure more consistent with results from eddy-permitting simulations. Models also showed a large spread in terms of trends in the MOC, whereby models with constant or two-dimensional (depth independent) eddy-induced coefficient κ experienced large increases in their transport (from 60% up to more than 100% strengthening over the last five decades), whereas eddy-permitting models or models with a three-dimensional κ showed weaker positive trends (between 30% and 50%). These results suggest that a larger compensation by the eddy-induced transport is achieved when a three-dimensional eddy diffusivity is implemented. Consistently, trends in Ψ^* were found to be considerably larger in eddy-permitting models or models with a three-dimensional κ, partially compensating for the increase in Eulerian-mean transport.

It might seem surprising that the sensitivity of the MOC to surface forcing in eddy-permitting models compares with coarse-resolution models. The answer is probably in the forcing itself, as wind stress changes are about 30–40% during the last five decades whereas previous idealized studies have considered the response to a doubling of winds or more, extending well beyond the anomalies considered here. Using different resolutions from coarse to eddy-resolving, Munday et al. (2013) showed that a significantly distinguishable response is achieved when wind forcing is roughly doubled. We
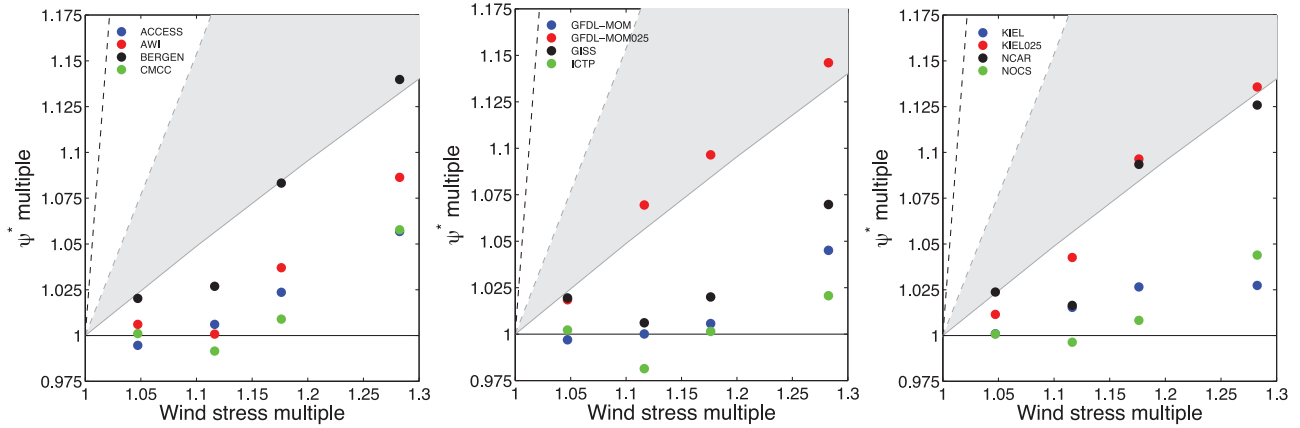
Fig. 29. Sensitivity of the zonally-averaged eddy-induced overturning streamfunction Ψ^* to wind stress changes. The area bounded by powers of $\tau^{1/2}$ and $\tau^{3/2}$ (solid and dotted gray lines, respectively) covers the region of predicted change in κ for a given change in wind stress according to the scaling of Meredith et al. (2012). The black lines show the limiting cases of no eddy compensation (solid) and complete eddy compensation (dashed). Both eddy-induced MOC, Ψ^*, and peak wind stress are decadal means relative to the second decade (1958–1967). Values for Ψ^* were computed as the spatial mean over the area [60–40°S ; 35.5 σ_2–37 σ_2], i.e. the area of larger decadal trends in the residual MOC (cf. Figs. 24 and 25).

conclude that, if the zonal wind stress shown in Fig. 2 will keep strengthening in the coming decades, we will expect models with a poor representation of eddy fluxes to continue intensifying their MOC, whereas eddy-permitting models or models with a depth dependent κ will saturate.

In the case of coarse-resolution models parameterizing eddy fluxes, allowing κ to vary with depth and to respond with a vertical structure to surface forcing changes was essential in producing a larger eddy compensation, as pointed out in previous studies (Danabasoglu and Marshall, 2007; Eden et al., 2009; Gent and Danabasoglu, 2011; Hofmann and Maqueda, 2011). It should be stressed, however, that the choice of parameters, such as the upper bound for κ or the maximum neutral slope S_{max}, remains a severe restriction to the parameterized eddy flux sensitivity, even if the maximum value of kappa is not necessarily relevant for NCAR. An ideal closure would be free of such parameters and tapering functions, as in Ferrari et al. (2010).

As for the ACC, the SAM was found to be highly correlated with the mean and residual MOC of the Southern Ocean, suggesting that wind anomalies are the main drivers of interannual variability in the Upper Cell. Nevertheless, models clustered again into two groups: models with constant or two-dimensional eddy-induced coefficient κ (with larger correlations with the SAM) and eddy-permitting models or models with a three-dimensional κ (with weaker correlations with the SAM). These results are suggestive of a general behavior, yet we are unable to make firm conclusions given that all of the models remain too coarse to fully resolve eddy processes.

We can estimate the relative role of wind and buoyancy variability on the Upper Cell of the MOC by looking at the sensitivity experiments WIND and BUOY performed with ICTP. Trends for both experiments are shown in Fig. 31. Most of the trend can be attributed to wind forcing (cf. Fig. 24), although appreciable changes in the uppermost branch are also present when buoyancy is the only forcing. With the recognition that the ICTP model fails to properly represent Southern Ocean eddy fluxes and variability, these results should be taken with care and similar experiments should be performed with better-performing models. Contrary to the relatively high degree of eddy saturation achieved by most models, the MOC seems to be strengthening considerably for all models, albeit with important differences among them. A distinctive degree of sensitivity for the zonal and meridional circulations comes as no surprise. In fact, the hypothesis that an eddy-saturated circumpolar transport does not imply complete eddy compensation of the overturning is gaining support.

Recently, Meredith et al. (2012) proposed a scaling theory in which, supported by observational and theoretical work (Ferrari and Nikurashin, 2010; Naveira Garabato et al., 2011), the eddy diffusivity coefficient was related to the EKE and the mean flow speed. Two limiting cases within which the scaling holds were identified: one for large EKE ($\kappa \propto EKE^{1/2}$) and one for small EKE ($\kappa \propto EKE^{3/2}$). At the eddy saturation limit, i.e. in the absence of significant changes in the ACC, EKE increases linearly with changes in wind stress (Hallberg and Gnanadesikan, 2006; Meredith and Hogg, 2006; Straub, 1993), and the equivalence between the two reduces the problem to assessing how κ responds to changes in wind forcing τ, ranging from a power of 1/2 to 3/2. Knowing the dependence of κ on τ is only partially satisfying, as a scaling for Ψ^* is necessary to make a statement on eddy compensation. Recalling that we are assuming eddy saturation of the ACC, as observed by Böning et al. (2008) and modelled here, we are also implying that stratification or equivalently potential vorticity has remained constant, so that the eddy-induced overturning ($\Psi^* = \kappa \mathbf{S}$, where $\mathbf{S} = -\nabla_h \rho / \partial_z \rho$) follows the same scaling as κ. The scaling proposed in Meredith et al. (2012) predicts only partial compensation, and many recent numerical studies corroborate the 'eddy saturation–partial eddy compensation' regime in eddy-resolving models (Abernathey et al., 2011; Morrison and Hogg, 2013; Munday et al., 2013; Viebahn and Eden, 2010).

We now apply the scaling of Meredith et al. (2012) to CORE-II simulations to characterize their MOC sensitivities to wind stress changes. Again, we disregard the first decade and changes in Ψ^* and zonal wind stress τ are computed as decadal means relative to the second decade and averaged between 60 °S and 40 °S and the potential density range of the Upper Cell (35.5–37 σ_2). Results are presented in Fig. 29, where the predicted area of possible changes in Ψ^* is bounded by the two limiting cases $\Psi^* \sim \tau^{1/2}$ (solid gray line) and $\Psi^* \sim \tau^{3/2}$ (dashed gray line). Only four models fall within the region of predicted changes (BERGEN, GFDL-MOM025, KIEL025 and NCAR), and only for the largest changes experienced during the last two decades. These four models stay close to the lower bound given by the $\Psi^* \sim \tau^{1/2}$ scaling, similar to the sensitivity obtained with finer resolution models in Morrison and Hogg (2013). It remains to be seen whether these models will stay in the predicted area of compensation for larger wind stress changes. As expected, AWI and GISS show signs of compensation but too weak according to this diagnostic; the remaining models fall short in reproducing a significant eddy-induced circulation response. Reasons for the insensitivity shown by most models have been discussed throughout the previous sections and can be traced to the depth independence and too low upper limit
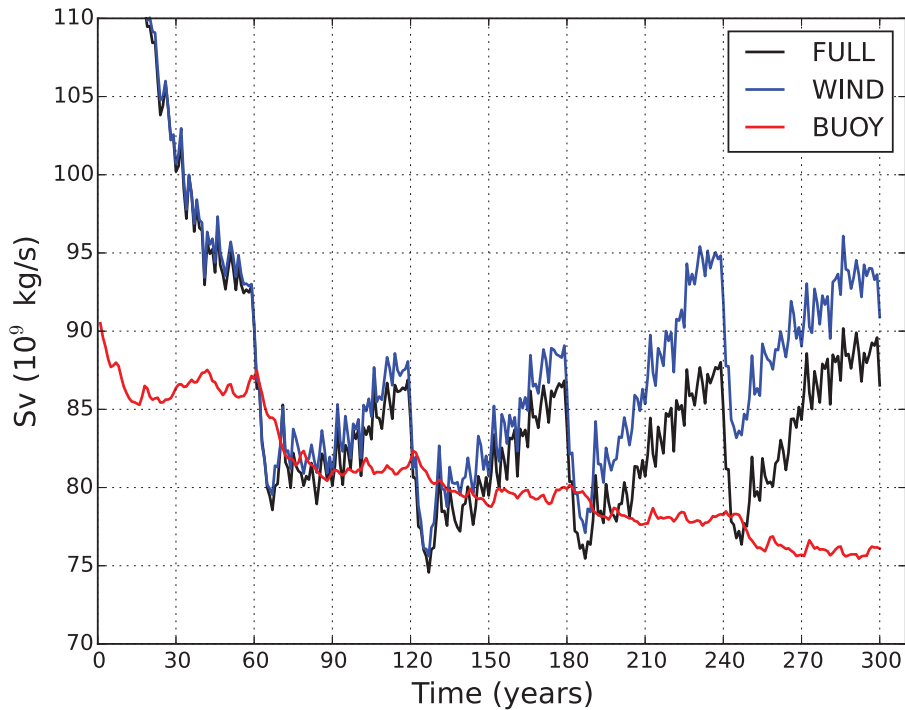
Fig. 30. Time series for the annual-mean vertically integrated mass transport (in Sv) through the Drake Passage for the entire length of the simulation (300 years; five repeated cycles) for the ICTP model. FULL refers to the standard 'full-forcing' CORE-II simulation, where all forcing fields vary interannually. WIND uses interannual winds but the climatological state for all other forcing fields. Conversely, BUOY uses interannual variations in all forcing but the winds.
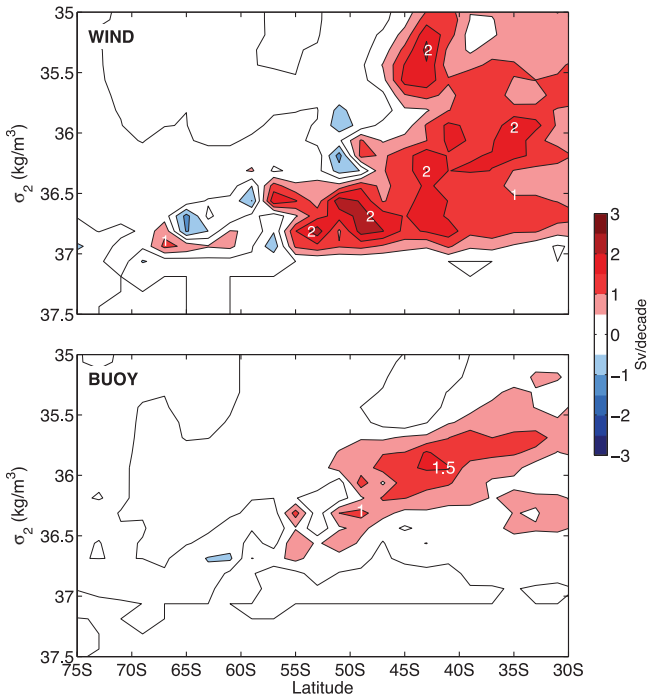

Fig. 31. The ICTP residual meridional overturning circulation, Ψ_{res}, linear decadal trend (Sv decade^{-1}) for the years 1958–2007 for the WIND and BUOY sensitivity experiments. WIND uses interannual winds but the climatological state for all other forcing fields. Conversely, BUOY uses interannual variations in all forcing but the winds. Contour interval is 0.5 Sv decade^{-1}.

of κ, as well as tapering functions with restrictive bounds on the local isopycnal slope **S**, all of which have already been proven to alter the simulation of the Southern Ocean and elsewhere (Danabasoglu and Marshall, 2007; Eden et al., 2009; Farneti and Gent, 2011; Gent and

Danabasoglu, 2011; Hofmann and Maqueda, 2011; Kuhlbrodt et al., 2012).

Our zonally-averaged decomposition of the MOC, as mentioned in Section 4, only separates the transient eddy-induced circulation Ψ^*, whereas the time mean $\overline{\Psi}(y, \sigma)$ accounts for both zonally averaged and standing eddy components. Recently, studies have highlighted the crucial role of standing eddy fluxes in compensating changes in wind-driven circulation as resolution increases (Abernathey and Cessi, 2014; Dufour et al., 2012; Zika et al., 2013a), so that our results might be underestimating the degree of eddy compensation in the models.

6. Conclusions

The main goal of this study was to assess the efficiency of mesoscale eddies, parameterized or permitted, in counteracting the observed forcing changes largely responsible for driving both ACC transport and MOC anomalies. In other words, we aimed at quantifying the degree of eddy saturation and eddy compensation in the models participating in CORE-II, and compared our results with available observations, previous fine-resolution numerical studies and theoretical constraints. Our main conclusions are:

(1) Most CORE-II simulations are close to the eddy saturation regime. Modest decadal trends were found in the simulated ACC transports that increase < 10% with a general strengthening of the driving winds of the order of ~30% during the last five decades (1958–2007). Models clustered into two groups. The first group – with constant or two-dimensional specification of the eddy-induced advection coefficient κ – showed somewhat larger steepening of isopycnals and larger ACC decadal trends (i.e. a weaker eddy saturation). The second group – made of eddy-permitting models or models with a three-dimensional κ – showed weaker changes in isopycnal slopes and associated ACC trends (i.e. a stronger eddy saturation). Consistent with previous studies (Danabasoglu and Marshall, 2007; Eden et al., 2009; Farneti and Gent, 2011; Gent

and Danabasoglu, 2011; Hofmann and Maqueda, 2011; Kuhlbrodt et al., 2012), a constant in time and/or space κ leads to a weak response of the parameterized eddy-induced transport to changes in surface forcing, and to large changes in the ACC transport (as measured at Drake Passage). In contrast, models with a flow-dependent three-dimensional eddy diffusivity, and models that more explicitly represent mesoscale eddies (though admittedly not fully resolved), exhibit a more eddy saturated state. On interannual time scales, all models correlated strongly with the Southern Annular Mode (SAM). The small spread among models in terms of their ACC transport response to the interannual forcing is probably due to the equally small spread in resolution and relatively small forcing changes. Finer resolution models (eddy-resolving) are expected to attain more complete saturations, for both stronger and weaker winds (Munday et al., 2013).

(2) The majority of CORE-II simulations were far from showing signs of eddy compensation, strengthening the MOC from 60% to more than 100% during the 1958–2007 period. Few models (eddy-permitting models or models with a three-dimensional κ) exhibited a stronger eddy compensation, but also manifested considerable decadal trends (around 30–50% increase in MOC during 1958–2007). The reason for this trend was attributed to the relatively small changes in wind forcing as compared to previous idealized studies where wind stress was (more than) doubled (Abernathey et al., 2011; Dufour et al., 2012; Farneti et al., 2010; Gent and Danabasoglu, 2011; Hofmann and Maqueda, 2011; Meredith et al., 2012; Morrison and Hogg, 2013; Munday et al., 2013; Viebahn and Eden, 2010). In a regime of total eddy saturation, a complete eddy compensation state is not to be expected – even at higher resolutions – as eddy saturation and eddy compensation are controlled by different mechanisms of eddy dynamics (Abernathey et al., 2011; Morrison and Hogg, 2013; Munday et al., 2013). When compared with the scaling proposed by Meredith et al. (2012), the eddy permitting and some of the models with a three-dimensional κ lay close to the predicted scaling of $\Psi^* \sim \tau^{1/2}$. As standing eddy fluxes were not considered in this study, our results might be underestimating the degree of eddy compensation. Also, it remains to be seen whether this relationship will stand for larger wind anomalies, finer resolutions and equilibrated responses.

We have focused our analysis on the effect of strengthening winds and the role of the SAM because, in the period analyzed, mechanical forcing has strengthened much more than buoyancy forcing, and its effects on the Southern Ocean have been larger so far. Eddy saturation and compensation relate to the insensitivity of the ACC and MOC to the wind forcing, but the response to buoyancy forcing is certainly present and is likely to alter the oceanic adjustment. It is difficult to disentangle the relative contribution from momentum and buoyancy fluxes in the CORE-II experiments, and the question warrants further investigation.

The design of targeted process studies can help in elucidating and furthering our understanding on the functioning and likely evolution of the Southern Ocean. A possibility would be to envisage flux perturbation experiments that isolate the momentum-forced and buoyancy-forced interannual variability as proposed in Yeager and Danabasoglu (2014), where momentum and buoyancy interannual anomalies are selectively turned off in all surface turbulent flux calculations. A simpler attempt was made here by turning off the variability in the momentum or buoyancy forcing, yet just with a single model. A next phase of CORE experiments should include the quantification of the individual role of momentum and buoyancy forcing on the ACC and MOC, and an analysis of the role of standing eddy fluxes on eddy compensation. Necessary ingredients will be a suite of models (ranging from coarse to eddy-resolving), a variety of mesoscale parameterizations, realistic and synthetic forcing anoma-

lies of different strengths and spatial patterns, and longer integrations to explore the baroclinic adjustment of the Southern Ocean on multidecadal-to-centennial time scales.

Appendix A. The meridional overturning streamfunction in depth and density space

Residual-mean theory applied to the Southern Ocean states that the Upper Cell of the Southern Ocean MOC results from a force balance between two circulations: a wind-driven (Eulerian-mean) overturning $\overline{\Psi}$ and an eddy-driven overturning Ψ^*. In a streamwise-averaged framework, the Eulerian and eddy-induced circulations set a residual circulation Ψ_{res}, which is the result of the approximate balance between the two components (Andrews and McIntyre, 1976; Marshall and Radko, 2003; McIntosh and McDougall, 1996)

$$\Psi_{\text{res}} = \overline{\Psi} + \Psi^*. \tag{1}$$

We thus express the residual meridional velocity as the sum of an Eulerian-mean velocity $\overline{v}$ and an eddy-induced velocity v^*

$$v_{res} = \overline{v} + v^*, \tag{2}$$

where $\overline{v} = -\partial_z \overline{\Psi}$ and $v^* = -\partial_z \Psi^*$, and an overbar represents zonal and time average. Similarly, the residual meridional velocity in an

isopycnal framework is given by

$$\nu_{res} = \overline{\nu} + \frac{\overline{\nu' h'}}{\overline{h}}, \tag{3}$$

where primes represent deviations about the average and h is the isopycnal thickness. The second term in Eq. (3) is the bolus velocity ν^* and $\overline{\nu' h'}$ the eddy transport, often parameterized as a down-grading thickness flux (McDougall and McIntosh, 2001).

The Eulerian-mean overturning can be expressed as (Marshall and Radko, 2003)

$$\overline{\Psi} = -\frac{\overline{\tau}}{f}, \tag{4}$$

where τ is the surface wind stress, f the Coriolis parameter, and Eq. (1) reduces to $\Psi_{res} = -\overline{\tau}/f + \Psi^*$. $\overline{\Psi}$ consists of a clock-wise cell (when looking to the west with Antarctica to the left) with an equatorward surface branch within the Ekman layer and a compensating geostrophic poleward transport below the topographic sill in the Drake Passage latitudes. The wind-driven overturning $\overline{\Psi}$ acts to steepen the isopycnals generating a store of available potential energy in the ACC region. The potential energy is then released by baroclinic instability, spawning transient mesoscale eddies, which eventually flatten the isopycnals. Thus, in the Southern Ocean, $\overline{\Psi}$ and Ψ^* oppose each other: the stronger the Eulerian-mean circulation, the steeper the isopycnals and the more energetic the eddy-induced transport that will flatten them.

Due to the general coarse resolution of global ocean models, eddy fluxes have to be parameterized, and the parameterization proposed by Gent and McWilliams (1990) (hereafter GM), based on the local isopycnal slope, is still the most commonly used. The eddy streamfunction Ψ^* is parameterized as a function of κ, the eddy-induced advection coefficient, and $\mathbf{S}$, the mean neutral isopycnal slope ($\mathbf{S} = -\nabla_h \rho / \partial_z \rho$, where ρ is the locally referenced potential density and $\nabla_h = (\partial_x, \partial_y, 0)$) so that $\Psi^* = \kappa \mathbf{S}$. $\mathbf{S}$ is usually capped by a maximum slope S_{max}, preventing numerical instabilities generated by the mixing when the slope becomes excessively steep. However, the use of an S_{max} produces spurious diapycnal diffusion when slopes get steeper than the maximum value. To overcome this problem, ocean models often use a slope tapering technique for the GM parameterization, tapering Ψ^* to zero and producing a constant eddy-induced transport velocity when $|\mathbf{S}| > S_{max}$. Introducing a tapering function that smoothly brings κ to zero eliminates any spurious diapycnal diffusion (for more details, the reader is referred to Danabasoglu and McWilliams, 1995; Large et al., 1997).

CORE-II simulations differ substantially in their implementation of the mesoscale eddy parameterization as the specification of κ, the value of S_{max} and the along isopycnal diffusion coefficient A_I vary greatly within models participating in CORE-II. A summary of the main parameters and implementations for the eddy-induced transport parameterization is given in Table 1. Previous studies have shown how details of the GM parameterization can influence the mean stratification and ACC strength, and alter the Southern Ocean response to surface forcing (Eden et al., 2009; Farneti and Gent, 2011; Kuhlbrodt et al., 2012), in particular through the specification of a vertically-dependent κ (Bryan et al., 2014; Gent and Danabasoglu, 2011; Hofmann and Maqueda, 2011; Viebahn and Eden, 2010). We expand on the details of the parameterization for mesoscale and submesoscale eddy fluxes in CORE models, where present, in Appendix B.

The residual meridional overturning streamfunction can be computed by

$$\Psi_{res}(y, z, t) = -\oint \int_{-H}^{z} (\nu + \nu^*) \, dz' \, dx, \tag{5}$$

where the flow is integrated first vertically from the ocean bottom H to a depth z and then zonally. In geopotential coordinate models using

a GM-like parameterization, ν^* is determined by (Gent et al., 1995)

$$\nu^* = -\partial_z(\kappa S_y), \tag{6}$$

where $S_y = -\partial_y \rho / \partial_z \rho$ is the meridional neutral slope and κ the eddy-induced advection coefficient. Computing the eddy-induced streamfunction Ψ^* from a model that parameterizes the effects of mesoscale eddy-induced transport simply reduces to integrating the eddy-induced velocities diagnosed from the model. Similarly to Ψ^*, a submesoscale mixed layer eddy streamfunction Ψ^*_{mle} can be computed from the additional parameterized transport, when present. Ψ^*_{mle} is then added to the Eulerian mean and mesoscale contributions to obtain the model's residual meridional overturning streamfunction Ψ_{res}.

The Southern Ocean MOC is often computed in density space, as in this study, and horizontal volume transports are classified according to potential density classes. When no parameterization of meridional eddy-induced velocity is used, the Southern Ocean MOC in density-space is given by the streamfunction in isopycnal layers

$$\Psi_{res}(y, \sigma, t) = -\oint \int_{-H}^{z(x,y,\sigma,t)} \nu(x, y, z', t) \, dz' dx, \tag{7}$$

where $z(x, y, \sigma, t)$ is the time-varying depth of the isopycnal. It is apparent from the density-space formulation how important it is to produce high-frequency outputs, in both time and space, for properly reproducing the correlation between isopycnals and meridional velocities. Ballarotta et al. (2013) showed that monthly diagnostics are sufficient for extracting the transient eddy contribution to the Southern Ocean overturning, although higher frequencies are certainly desirable (for example 5-day averages as in Farneti et al., 2010; Ballarotta et al., 2013). The two eddy-permitting models GFDL-MOM025 and KIEL025 both used monthly diagnostics. In this study, we chose a potential density coordinate referenced to 2000 m (σ_2) to better characterize the interior water masses. The σ_2 vertical coordinate also enables a proper comparison with the isopycnal models FSU2, GFDL-GOLD, and BERGEN, each of which use σ_2 as their vertical coordinate. When binning transports, a large number of potential density levels are recommended, usually between 80 and 100, encompassing all Southern Ocean σ_2 layers (from 1028 kg m^{-3} to 1038 kg m^{-3}).

The time-mean overturning streamfunction is obtained by first time averaging the meridional velocities and then integrating them zonally along the time averaged isopycnals σ:

$$\overline{\Psi}(y, \sigma) = -\oint \int_{-H}^{\overline{z}(x,y,\sigma)} \overline{\nu}(x, y, z') \, dz' dx. \tag{8}$$

When the zonal integration is performed along latitude circles, as in this paper, $\overline{\Psi}(y, \sigma)$ includes opposing contributions from both the zonally averaged flow and standing eddies arising from the meridional correlations between ν and σ (Dufour et al., 2012; Lee and Coward, 2003):

$$\overline{\Psi} = \langle \overline{\Psi} \rangle + \overline{\Psi}_{SE}, \tag{9}$$

where

$$\langle \overline{\Psi} \rangle(y, \sigma) = -\oint \int_{-H}^{\langle \overline{z} \rangle(y,\sigma)} \langle \overline{\nu} \rangle(y, z') \, dz' dx \tag{10}$$

is the mean wind-driven circulation and angle brackets indicate zonal averaging. In this paper, we have not attempted to decompose the standing eddy contribution $\overline{\Psi}_{SE}$ from the time-mean component. Performing a streamwise-averaged decomposition would eliminate $\overline{\Psi}_{SE}$ (Marshall et al., 1993; Viebahn and Eden, 2012).

The transient eddy-induced component is obtained by subtracting the time-mean from the residual (e.g., Treguier et al., 2007; Farneti
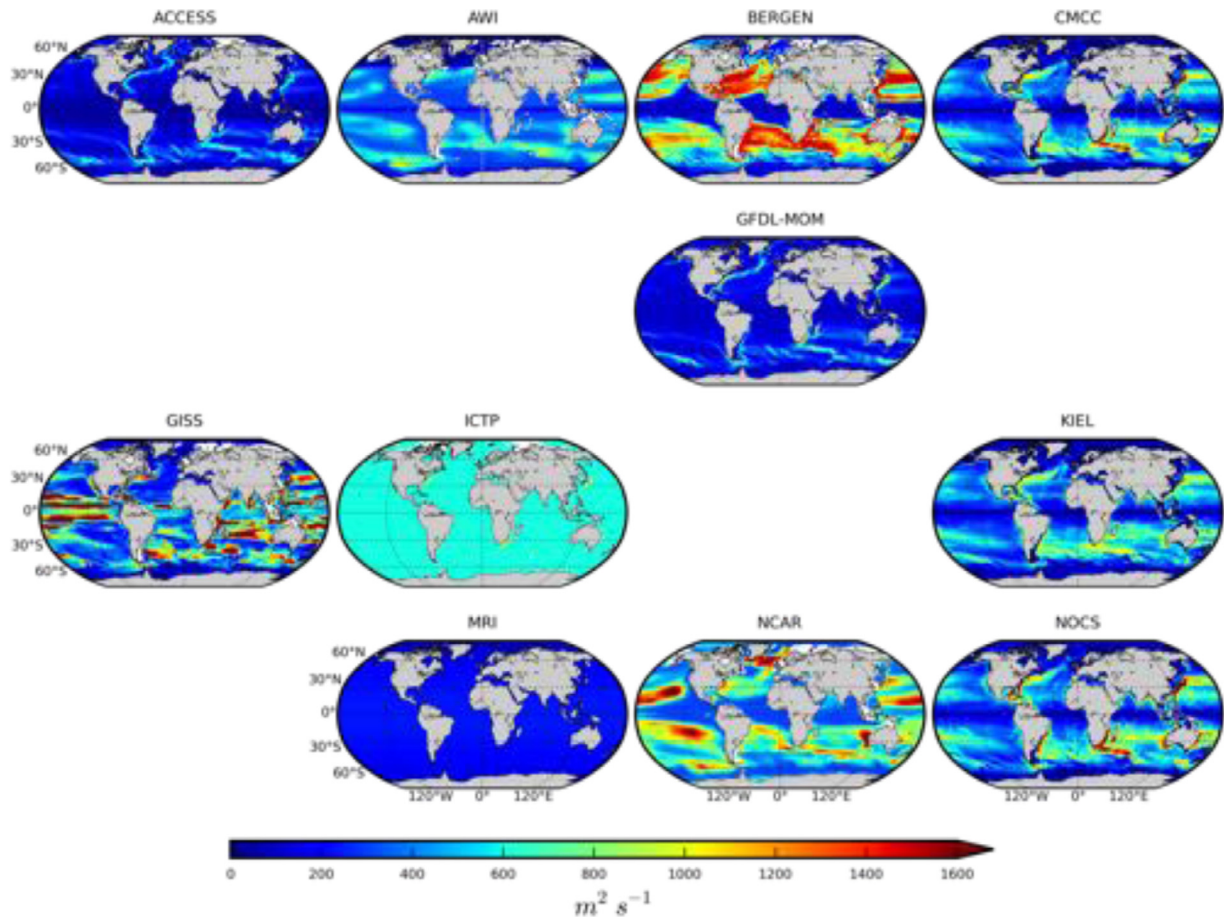
Fig. 32. The time-mean eddy-induced advection coefficient (κ, in m² s⁻¹), as in Fig. 20, but for the global ocean. Shown is the climatological value computed as the time mean between years 1958 and 2007. For those models having a depth-dependent κ (AWI, BERGEN, GISS and NCAR), the value at 300 m depth is shown.

et al., 2010; Ballarotta et al., 2013)

$$\Psi^* = \Psi_{\text{res}} - \overline{\Psi}. \tag{11}$$

In models including a GM-like parameterization, Ψ^* is first mapped onto potential density classes and then added to $\overline{\Psi}$ to define the total circulation Ψ_{res}.

Appendix B. Parameterization of mesoscale and submesoscale eddy fluxes in the contributing models (in alphabetical order)

A comprehensive description of the ocean and sea-ice characteristics of all contributing models can be found in Danabasoglu et al. (2014), and interested readers should refer to Table 1, Table 2 and Appendix A of Danabasoglu et al. (2014) for a summary of physics and parameterizations present in the models. We summarize here the details of the parameterization of eddy fluxes, where present. Most of the models include some flavor of the eddy parameterization scheme developed by Gent and McWilliams (1990, hereafter GM) and Gent et al. (1995). The eddy-induced coefficient κ is plotted in Fig. 32, as in Fig. 20, but now global values are given for completeness.

A few models also include a parameterization for submesoscale eddies (ACCESS, GFDL-GOLD, GFDL-MOM, GFDL-MOM025 and NCAR), whereas a model does not include any parameterization of eddy fluxes at all (INMOM). We note that none of the models included in this study can be considered to be eddy-resolving and hence all models would require, in principle, some sort of parameterization for subgridscale unresolved flows. Values and space-time characteristics for κ, the along-isopycnal neutral diffusion coefficient

A_I and the maximum neutral slope used for tapering off the neutral physics fluxes $S_{\max}$ are given in Table 1.

B1. ACCESS

ACCESS-OM (Bi et al., 2013b) is the ocean and sea-ice component of the Australian Community Climate and Earth System Simulator Coupled Model (ACCESS-CM; Bi et al., 2013a). ACCESS-OM is based on the NOAA/GFDL MOM4p1 ocean code (Griffies, 2007). ACCESS-OM uses the following subgrid scale physics: isoneutral diffusion following Redi (1982) and Griffies et al. (1998); a modified GM scheme following Ferrari et al. (2010) with baroclinic closure of the thickness diffusivity; and a submesoscale mixed layer restratification scheme following Fox-Kemper et al. (2011). More details are given in Section B.8.

B2. AWI

The Finite Element Sea-ice Ocean Model (FESOM, Wang et al., 2014) is the ocean–sea-ice component of the coupled climate model which has been developed at the Alfred Wegener Institute for Polar and Marine Research (Sidorenko et al., 2014). FESOM uses a GM-like thickness diffusivity that is proportional to the squared buoyancy frequency, as used in Danabasoglu and Marshall (2007) and detailed in Appendix B.16. The reference diffusivity is set to 1500 m² s⁻¹ at horizontal resolution coarser than 50 km; it is linearly reduced to 50 m² s⁻¹ from 50 km resolution to 25 km resolution. The lower bound of diffusivity is 0.2 times the local reference diffusivity. The neutral diffusivity is set the same as the thickness diffusivity. Within

the surface diabatic boundary layer (taken as the surface mixed layer as defined in Large et al., 1997), the streamfunction of eddy transport is linearly tapered from the value at the base of the surface boundary layer to zero at the ocean surface, that is, the horizontal eddy velocity is vertically constant in the surface boundary layer. This implementation is effectively the same as the case with vanishing transition layers in Danabasoglu et al. (2008). To avoid numerical instability, the critical neutral slope, S_{max}, is set to 0.05. The critical value does not impact the calculation of surface boundary layer depth as it is defined as the surface mixed layer depth. In the surface boundary layer the neutral diffusion is rotated to horizontal diffusion and the diffusivity is set to the local reference diffusivity value.

B3. BERGEN

NorESM-O is the ocean–sea-ice component of the Norwegian Earth System Model (NorESM; Bentsen et al., 2013). The model system is based on the CESM version 1.0.4 and the application of atmospheric forcing is identical to that of CESM. NorESM-O implements a GM like parameterization by Laplacian diffusion of the interfaces of isopycnic layers. Consistent with this interface smoothing, eddy induced lateral mass fluxes are constructed. The eddy-induced advection coefficient κ is dependent on an eddy length and time scale proposed by Eden and Greatbatch (2008) and implemented according to Eden et al. (2009). The depth-dependent κ is thus given by

$$\kappa = c L^2 \sigma. \tag{12}$$

In Eq. (12), σ is the local Eady growth rate given by $\sigma = f Ri^{-1/2}$, with f the Coriolis parameter and Ri the Richardson number, L is the minimum between the Rossby radius L_r and the Rhines scale $L_{Rhi} = \sqrt{EKE^{1/2} \beta^{-1}}$ (where EKE denotes eddy kinetic energy and $\beta = \partial_y f$), and c a tuning parameter. The Rossby radius is computed as $L_r = \min\left(\frac{c_r}{|f|}, \sqrt{\frac{c_r}{2\beta}}\right)$, where c_r is the first baroclinic Rossby wave speed. The Eady growth rate σ has a singularity as $N \to 0$, with N the local buoyancy frequency. To prevent this, σ is set to $f(Ri + \gamma)^{-1/2}$, with $\gamma = 200$ and being effectively an upper limit for σ. The low value of the non-dimensional scaling for the diffusivity is used ($c = 2$) and upper and lower bound of the diffusivity is set to 100 m^2 s^{-1} and 1500 m^2 s^{-1}, respectively. The isopycnal eddy diffusivity is set equal to the thickness diffusivity. The lateral eddy diffusivity in the mixed layer uses the mean thickness diffusivity of the upper 100 m of the isopycnic interior of the model. The thickness diffusion is implemented as Laplacian diffusion of layer interfaces.

B4. CMCC

The CMCC-NEMO ocean–sea-ice model is based on the Nucleus for European Modeling of the Ocean (NEMO) framework version 3.3 (Madec, 2008). The version used in this study is the ORCA1, which has a one degree nominal resolution with a meridional refinement in the latitudinal band 20 °S–20 °N up to 1/3 ° at the Equator (360×291 grid points). Lateral diffusivity is parameterized by an isoneutral Laplacian operator. The eddy diffusivity coefficient is 1000 m^2 s^{-1} at the Equator and decreases with the reduction of the grid spacing with latitude, becoming < 500 m^2 s^{-1} poleward of 60° latitude. An additional eddy-induced velocity is applied on temperature and salinity using a spatially and temporally varying coefficient (Gent and McWilliams, 1990). The eddy-induced advection coefficient is time and space varying, but depth independent, following Treguier et al. (1997). It is based on the local growth rate of baroclinic instabilities and it decreases linearly in the latitudinal band 20 °S–20 °N vanishing at the Equator. The global annual mean value is 380 m^2 s^{-1} and actual values can range from 0 to 5000 m^2 s^{-1}.

B5. FSU

The FSU contribution uses a modified Community Climate System Model version 3 (CCSM3) framework where the HYbrid Coordinate Ocean Model (HYCOM; Halliwell, 2004) version 2.2 is employed as the ocean component. Interface height smoothing – corresponding to GM – is applied through a biharmonic operator, with a mixing coefficient determined by the grid spacing (in m) cubed times a constant velocity scale of 0.05 m s^{-1}. For regions where the coordinate surfaces are aligned with constant pressure (mostly in the upper ocean mixed layer), GM is not implemented, and lateral diffusion is oriented along pressure surfaces rather than rotated to neutral directions.

The FSU HYCOM used here and in Danabasoglu et al. (2014) is based on an earlier version of HYCOM which advects density and salinity (instead of temperature T and salinity S) and therefore does not conserve heat (see Griffies et al., 2014 for a discussion of its impact on sea level). For this study, one new CORE-II simulation (FSU2) has been performed with HYCOM using the formulation that advects T and S. We give a brief summary of its configuration below.

B6. FSU2

FSU2 is a global configuration of HYCOM (Bleck, 2002; Chassignet et al., 2003; Halliwell, 2004). Interface pressure smoothing (corresponding to the GM parameterization) is applied through a biharmonic operator, with a mixing coefficient determined by the grid spacing (in m) times a velocity scale of 0.02 m s^{-1} everywhere except in the Pacific and Atlantic north of 40 °N where a Laplacian operator with a velocity scale of 0.01 m s^{-1} is used. For regions where the model has coordinate surfaces aligned with constant pressure (mostly in the upper ocean mixed layer), GM is not implemented, and lateral diffusion is oriented along pressure surfaces rather than rotated to neutral directions. No parameterization has been implemented for abyssal overflows.

B7. GFDL-GOLD

The ocean component of the GFDL-GOLD configuration employs the Generalized Ocean Layer Dynamics (GOLD) isopycnal code and the configuration is identical to the one described in Dunne et al. (2012). GFDL-GOLD uses an interface height diffusion, which is equivalent to the GM eddy parameterization, where eddy fluxes, $\overline{v'h'}$, are proportional to the thickness gradient, $\frac{\partial \bar{h}}{\partial y}$, times a two-dimensional time-varying thickness diffusivity κ:

$$\overline{v'h'} = -\kappa \frac{\partial \bar{h}}{\partial y}. \tag{13}$$

GFDL-GOLD uses a thickness diffusion parameterization motivated by Griffies et al. (2005) as used in Dunne et al. (2012), with a local slope-dependent coefficient varying between 10 m^2 s^{-1} and 900 m^2 s^{-1}. GFDL-GOLD also makes use of the Fox-Kemper et al. (2011); 2008) submesoscale eddy parameterization, with details for the GFDL-GOLD implementation provided in Fox-Kemper et al. (2011).

B8. GFDL-MOM

The ocean component of the GFDL-MOM configuration employs the Modular Ocean Model (MOM) code from Griffies et al. (2011). For the parameterized mesoscale eddy-induced transport, GFDL-MOM uses the stream function approach given by Ferrari et al. (2010). The one-dimensional boundary-value problem (BVP) takes the form

$$\left(c^2 \frac{d}{dz^2} - N^2\right) \Upsilon = (g/\rho_o) \kappa \nabla_z \rho \tag{14}$$

$$\Upsilon(\eta) = \Upsilon(-H) = 0, \tag{15}$$

where c is a depth independent speed to be specified (here defined as $c = c_2$ the second baroclinic phase speed), N^2 the squared buoyancy frequency, $\mathbf{Y}$ the parameterized eddy-induced transport and ρ_o is a constant reference density. The closure imposes Dirichlet boundary conditions on the eddy-induced transport (Eq. (15)). GFDL-MOM uses a constant value for the isopycnal diffusivity A_I set to 600 m^2 s^{-1} throughout the ocean. The eddy-induced advection coefficient κ is flow-dependent, and is set to be proportional to the vertically averaged horizontal density gradient (Griffies et al., 2005)

$$\kappa = \alpha \overline{\langle \nabla_z \rho \rangle}^z \left(\frac{L^2 g}{\rho_o N_o} \right). \tag{16}$$

Here, α is a dimensionless tuning constant set to 0.07, L is a constant length scale set to 50 km, N_o is a constant buoyancy frequency set to 0.004 s^{-1}, $g = 9.8$ m s^{-1} is the acceleration of gravity, $\rho_o = 1035$ kg m^{-3} is the reference density for the Boussinesq approximation, and $\overline{\langle \nabla_z \rho \rangle}^z$ is the average of the horizontal gradient of the locally referenced potential density taken over the depth range 100–2000 m. In GFDL-MOM, minimum and maximum values of κ are set to 100 and 600 m^2 s^{-1}, respectively. Near the surface boundary layer, the neutral slope can become very large. It is common to taper the parameterized eddy-induced streamfunction to reduce the occurrence of unphysical values in the eddy-induced velocity field. However, the method of Ferrari et al. (2010) dispenses with the need for such tapering, as their scheme produces a physically sensible streamfunction even when the vertical stratification vanishes. For the neutral diffusion scheme, however, the GFDL-MOM simulations taper the diffusivity according to Danabasoglu and McWilliams (1995) for neutral slopes larger than $S_{max} = 1/200$.

To avoid unphysical values in the velocity field, the streamfunction is tapered to the surface when the neutral slope, S, reaches a critical value defined by the maximum slope S_{max}. In GFDL-MOM, S_{max} is set to 1/200.

GFDL-MOM also includes a parameterization for mixed-layer eddies (MLE) as proposed in Fox-Kemper et al. (2008) and Fox-Kemper et al. (2011). The MLE restratification scheme for a coarse-resolution model is given by

$$\Psi^*_{mle} = C_e \frac{\Delta s\, H^2 \nabla \overline{b}^z \times \hat{\mathbf{z}}}{L_f \sqrt{f^2 + T^{-2}}} \mu(z), \tag{17}$$

where the vertical structure $\mu(z)$ is a function of the mixed layer depth H, $C_e = 0.07$ is a dimensionless number, Δs is the coarse grid horizontal grid spacing, $L_f = 5000$ m is the local width of mixed layer fronts, b is buoyancy, f is the Coriolis parameter, $T = 1$ day the time scale needed to mix momentum across the mixed layer.

B9. GFDL-MOM025

The fine-resolution GFDL model, MOM025, is the ocean-ice component from the CM2.5 coupled model that is documented in Delworth et al. (2012). The ocean model is based on MOM5 (Griffies, 2012) and uses a squared isotropic grid, where d$x \cong$dy at all latitudes. The oceanic resolution is 1/4° (or 27.75 km) at the equator and progressively increases towards the poles reaching 13.8 km at 60° and 9 km at 70°. GFDL-MOM025 does not use a parameterization of mesoscale eddy-induced transport.

The submesoscale mixed layer restratification scheme of Fox-Kemper et al. (2011), described in GFDL-MOM (Section B.8), is also implemented in GFDL-MOM025 but with some changes. Not only some of the parameters have changed ($C_e = 0.05$ and the number of iterations on the smoothing of the streamfunction has increased), but also some of its numerical implementation. The depth-independent portion of Eq. (17) is computed with the necessary smoothing and limiting. Then, the depth-independent portion is projected vertically by multiplying by the vertical structure function $\mu(z)$. This was not the case in the original version used in GFDL-MOM, where smoothers and limiters were applied to the three dimensional streamfunction, originating numerical problems that grew with resolution. For more details, the interested reader is referred to Chapter 24 of the MOM manual (Griffies, 2012).

B10. GISS

The GISS model is the ocean component of the coupled NASA GISS model (Liu et al., 2003). Mesoscale eddies are represented by the GM scheme coded with the skew flux formulation (Griffies, 1998) with a new three-dimensionally varying surface-enhanced mesoscale diffusivity based on a theoretical prediction of the surface eddy kinetic energy (Canuto and Dubovikov, 2006). The eddy-induced advection coefficient κ has a three-dimensional structure, with the vertical profile depending on both baroclinic and barotropic modes. κ exhibits a surface enhancement and is proportional to the square root of the eddy kinetic energy. The parameterization is thus locally-dependent both in the horizontal and in the vertical:

$$\kappa = 1.7 s^{1/2}\, r_d\, K(z)^{1/2} \tag{18}$$

where r_d is the Rossby radius, s a filling factor and K is the mesoscale kinetic energy $K(z) = K_t \Gamma(z)$ with K_t being the surface eddy kinetic energy and $\Gamma(z)$ a dimensionless function. More details and the full derivation of the scheme can be found in Canuto and Dubovikov (2006).

B11. ICTP

The ICTP-MOM ocean–sea-ice model is a coarse 2° resolution version of the GFDL-MOM model. As in GFDL-MOM, mesoscale eddy-induced transports are parameterized following the boundary-value problem approach of Ferrari et al. (2010), in which the variable eddy-induced advection coefficient is bounded between 600 and 1400 m^2 s^{-1}. Neutral diffusivity (Redi, 1982) has a value of 800 m^2 s^{-1}. The parameterization for submesoscale eddies of Fox-Kemper et al. (2011) is not included.

B12. INMOM

The Institute of Numerical Mathematics (INM) Ocean Model (INMOM) is the ocean-ice component of the INM Earth Climate Model (INMCM4.0; Volodin et al., 2010; Gusev and Diansky, 2014). The tracer equations use isopycnal diffusion with a constant mixing coefficient of 100 m^2 s^{-1} but no additional parameterization for mesoscale eddies is used.

It should also be noted that this model has used different bulk formulae than the ones recommended by the CORE-II experimental protocol. As stated in Danabasoglu et al. (2014), the forcing data sets have been developed using the formulae described in Large and Yeager (2009), and participating modeling groups were requested to use the same bulk transfer coefficients. Instead, INMOM has opted for the bulk formulae given by the Arctic Ocean Model Intercomparison Project (AOMIP; http://www.whoi.edu/projects/AOMIP/). In particular, for the case of open ocean momentum transfer, surface stresses are a function of air density, wind speed magnitude and wind speed vector, and are given by $\vec{\tau}_{ao} = \rho_a D_{ao} |\vec{W}_s| \vec{W}_s$, where ρ_a is the air density, D_{ao} is the air-ocean drag coefficient and W_s is the surface wind. The drag coefficient is defined as $D_{ao} = (1.10 + 0.04\, \vec{W}_s) \times 10^{-3}$. Moreover, for reasons related to the simulation of sea-ice, a value of 1 m s^{-1} was added to the CORE-II wind speeds prior to the wind stress calculation. As a result, INMOM computed wind stress is larger than any other CORE-II model, as evidenced in Fig. 3, with the biggest differences to be found in the tropical regions and the Southern Ocean.

B13. KIEL

The Kiel ocean model configuration ORCA05 is based on the NEMO code (version 3.1.1; Madec, 2008). To parameterize mesoscale eddies, the GM scheme is used with variable mixing coefficient related to the growth of baroclinic instabilities (Treguier et al., 1997). Values for the eddy-induced advection coefficient κ vary form 0 m^2 s^{-1} to 1000 m^2 s^{-1}. Isoneutral diffusivity has a nominal value of 600 m^2 s^{-1} and it is scaled according to the grid spacing.

B14. KIEL025

The KIEL025 model is a finer resolution of KIEL, using the NEMO 3.4.1 code. With a tripolar grid of nominal 1/4° resolution, typical grid sizes are in the range 9–14 km between 70 °S and 60 °S. Surface salinity restoring in KIEL025 is 300 days, five times stronger than in ORCA05. KIEL025 does not use a parameterization of the eddy-induced advective transport but the neutral diffusion scheme is active in its simulations. The isoneutral Laplacian operator is set to 300 m^2 s^{-1} at the Equator decreasing with the reduction of the grid spacing with latitude.

B15. MRI

MRI.COM is the ocean–sea-ice component of MRI-CGCM3 (MRI Coupled General Circulation Model version 3; Yukimoto et al., 2012) and is based on the MRI.COM version 3 (Tsujino et al., 2011).

Mixing along neutral surfaces caused by eddy stirring is parameterized using isoneutral mixing (Redi, 1982) with a constant coefficient of 1000 m^2 s^{-1}. MRI also uses the GM parameterization with a fixed in time coefficient that depends on the grid area ranging from 100 m^2 s^{-1} to 235 m^2 s^{-1}. The maximum allowed slope of isoneutral surfaces is set to 1/1000.

B16. NCAR

NCAR contribution uses the Parallel Ocean Program version 2 (POP2; Smith et al., 2010), which is the ocean component of the Community Climate System Model version 4 (CCSM4; Gent et al., 2011). The model details are described in Danabasoglu et al. (2012). The model tracer equations use the GM isopycnal transport parameterization in its skew-flux form (Griffies, 1998). The effects of diabatic mesoscale fluxes within the surface diabatic layer are included via a simplified version of the near-boundary eddy flux parameterization of Ferrari et al. (2008), as implemented by Danabasoglu et al. (2008). Both the thickness and isopycnal diffusivity coefficients vary identically in the vertical, following Ferreira et al. (2005) and Danabasoglu and Marshall (2007)

$$\kappa = \kappa_0 \left(\frac{N^2}{N_{\text{ref}}^2} \right), \tag{19}$$

where κ_0 is the initial/reference thickness diffusivity, N is the buoyancy frequency and N_{ref} its reference value.

In the upper ocean, NCAR uses enhanced diffusivity values which can be as large as 3000 m^2 s^{-1}. Diffusivity values diminish to 300 m^2 s^{-1} by a depth of about 2000 m. In the surface diabatic layer, the horizontal diffusivity coefficient is set also to 3000 m^2 s^{-1}. The restratification effects of the finite-amplitude, submesoscale mixed layer eddies are included, using the mixed layer eddy parameterization of Fox-Kemper et al. (2008) and Fox-Kemper et al. (2011) as given in Eq. (17). NCAR uses the same parameter settings as in the GFDL model, namely $C_e = 0.07$, $L_f = 5000$ m and $T = 1$ day.

B17. NOCS

NOCS-ORCA1 is the 1° model configuration of version 3.4 of the NEMO framework being used at the National Oceanography Centre Southampton (NOCS).

Lateral diffusivity is parameterized by an isoneutral Laplacian operator with an eddy diffusivity coefficient of 1000 m^2 s^{-1} at the Equator decreasing with the reduction of the grid spacing with the latitude—it becomes < 500 m^2 s^{-1} poleward of 60° latitude. Isoneutral diffusion and the GM eddy advection are both implemented with a triad formalism (Griffies, 1998; Griffies et al., 1998). Within the surface mixed-layer lateral diffusion is along slopes linearly decreasing with depth from the isoneutral slope immediately below the mixed layer to zero (flat) at the surface. These linearly varying slopes are also used to calculate the GM skew-fluxes: this is equivalent to a GM eddy-induced velocity that is uniform through the mixed layer (Treguier et al., 1997). This approach, used in OPA since 1999 (Madec, personal communication), is a simplified version of the approach recommended by Danabasoglu et al. (2008). Values for the eddy-induced advection coefficient κ vary from 0 m^2 s^{-1} to 5000 m^2 s^{-1}.

References

Abernathey, R., Cessi, P., 2014. Topographic enhancement of eddy efficiency in baroclinic equilibration. J. Phys. Oceanogr. 44, 2107–2126.

Abernathey, R., Marshall, J., Ferreira, D., 2011. The dependence of Southern Ocean meridional overturning on wind stress. J. Phys. Oceanogr. 41, 2261–2278.

Abernathey, R.P., Marshall, J., 2013. Global surface eddy diffusivities derived from satellite altimetry. J. Geophys. Res. 118, 901–916.

Allison, L.C., Johnson, H.L., Marshall, D.P., Munday, D.R., 2010. Where do winds drive the Antarctic Circumpolar Current? Geophys. Res. Lett. 37 (L12605). doi:10.1029/2010GL043355.

Allison, L.C., Johnson, H.L., Marshall, D.P., Munday, D.R., 2011. Spin-up and adjustment of the Antarctic Circumpolar Current and global pycnocline. J. Mar. Res. 69, 167–189.

Andrews, D.G., McIntyre, M.E., 1976. Planetary waves in horizontal and vertical shear: the generalized Eliassen-Palm relation and the mean zonal acceleration. J. Atmos. Sci. 33, 2031–2048.

Ballarotta, M., Drijfhout, S., Kuhlbrodt, T., Döös, K., 2013. The residual circulation of the Southern Ocean: which spatio-temporal scales are needed? Ocean Model. 64, 46–55.

Bentsen, M., Bethke, I., Debernard, J.B., Iversen, T., Kirkevag, A., Seland, O., Drange, H., Roelandt, C., Seierstad, I.A., Hoose, C., Kristjansson, J.E., 2013. The Norwegian Earth System Model, NorESM1-M. Part 1: Description and basic evaluation of the physical climate. Geosci. Model Dev. 6, 687–720.

Bi, D., Dix, M., Marsland, S.J., O'Farrell, S., Rashid, H., Uotila, P., Hirst, A.C., Kowalczyk, E., Golebiewski, M., Sullivan, A., Yan, H., Hannah, N., Franklin, C., Sun, Z., Vohralik, P., Watterson, I., Zhou, X., Fiedler, R., Collier, M., Ma, Y., Noonan, J., Stevens, L., Uhe, P., Zhu, H., Hill, R., Harris, C., Griffies, S.M., Puri, K., 2013a. The ACCESS Coupled Model: description, control climate and preliminary validation. Aust. Meteorol. Oceanogr. J. 63, 41–64.

Bi, D., Marsland, S.J., Uotila, P., O'Farrell, S., Fiedler, R., Sullivan, A., Griffies, S.M., Zhou, X., Hirst, A.C., 2013b. ACCESS-OM: the ocean and sea-ice core of the ACCESS coupled model. Aust. Meteorol. Oceanogr. J. 63, 213–232.

Bintanja, R., van Oldenborgh, G.J., Drijfhout, S.S., Wouters, B., Katsman, C.A., 2013. Important role for ocean warming and increased ice-shelf melt in Antarctic sea-ice expansion. Nat. Geosci. 6, 1–4.

Bleck, R., 2002. An oceanic general circulation model framed in hybrid isopycnic-Cartesian coordinates. Ocean Model. 4, 55–88.

Böning, C.W., Dispert, A., Visbeck, M., Rintoul, S.R., Schwarzkopf, F.U., 2008. The response of the Antarctic Circumpolar Current to recent climate change. Nat. Geosci. 1 (12), 864–869.

Bryan, F.O., Gent, P.R., Tomas, R., 2014. Can Southern Ocean eddy effects be parameterized in climate models? J. Climate 27 (1), 411–425.

Bryden, H.L., Cunningham, S.A., 2003. How wind-forcing and air-sea heat exchange determine the meridional temperature gradient and stratification for the Antarctic Circumpolar Current. J. Geophys. Res. 108 (C8), 3275. doi:10.1029/2001JC001296.

Canuto, V.M., Dubovikov, M.S., 2006. Dynamical model of mesoscales in z-coordinates. Ocean Model. 11 (1–2), 123–166.

Cerovecki, I., Talley, L.D., Mazloff, M.R., 2011. A comparison of Southern Ocean air-sea buoyancy flux from an ocean state estimate with five other products. J. Climate 24, 6283–6306.

Cessi, P., 2008. An energy-constrained parameterization of eddy buoyancy flux. J. Phys. Oceanogr. 38, 1807–1819.

Chassignet, E.P., Smith, L.T., Halliwell, G.T., Bleck, R., 2003. North Atlantic simulations with the Hybrid Coordinate Ocean Model (HYCOM): impact of the vertical coordinate choice, reference pressure, and thermobaricity. J. Phys. Oceanogr. 33, 2504–2526.

Chidichimo, M.P., Donohue, K.A., Watts, D.R., Tracey, K.L., 2014. Baroclinic transport time series of the Antarctic Circumpolar Current measured in Drake Passage. J. Phys. Oceanogr. 44, 1829–1853.

Cunningham, S.A., Alderson, S.G., King, B.A., Brandon, M.A., 2003. Transport and variability of the Antarctic Circumpolar Current in the Drake Passage. J. Geophys. Res. 108 (C5), 8084. doi:10.1029/2001JC001147.

Curry, R., Dickson, B., Yashayaev, I., 2003. A change in the freshawater balance pf the Atlantic Ocean over the past four decades. Nature 426, 826–829.

Danabasoglu, G., Bates, S.C., Briegleb, B.P., Jayne, S.R., Jochum, M., Large, W.G., Peacock, S., Yeager, S.G., 2012. The CCSM4 ocean component. J. Climate 25, 1361–1389.

Danabasoglu, G., Ferrari, R., McWilliams, J.C., 2008. Sensitivity of an ocean general circulation model to a parameterization of near-surface eddy fluxes. J. Climate 21, 1192–1208.

Danabasoglu, G., Marshall, J., 2007. Effects of vertical variations of thickness diffusivity in an ocean general circulation model. Ocean Model. 18, 122–141.

Danabasoglu, G., McWilliams, J.C., 1995. Sensitivity of the global ocean circulation to parameterizations of mesoscale tracer transports. J. Climate 8, 2967–2987.

Danabasoglu, G., Yeager, S.G., Bailey, D., Behrens, E., Bentsen, M., Bi, D., Biastoch, A., Böning, C., Bozec, A., Canuto, V.M., Cassou, C., Chassignet, E., Coward, A.C., Danilov, S., Diansky, N., Drange, H., Farneti, R., Fernandez, E., Fogli, P.G., Forget, G., Fujii, Y., Griffies, S.M., Gusev, A., Heimbach, P., Howard, A., Jung, T., Kelley, M., Large, W.G., Leboissetier, A., Lu, J., Madec, G., Marsland, S.J., Masina, S., Navarra, A., Nurser, A.J.G., Pirani, A., Salas y Mélia, D., Samuels, B.L., Scheinert, M., Sidorenko, D., Treguier, A.-M., Tsujino, H., Uotila, P., Valcke, S., Voldoire, A., Wang, Q., 2014. North Atlantic simulations in Coordinated Ocean-ice Reference Experiments phase II (CORE-II). Part I: mean states. Ocean Model. 73, 76–107.

Delworth, T.L., Rosati, A., Anderson, W., Adcroft, A.J., Balaji, V., Delworth, R.B.L., Rosati, A., Anderson, W., Adcroft, A.J., Balaji, V., Benson, R., Dixon, K., Griffies, S.M., Lee, H.-C., Pacanowski, R.C., Vecchi, G.A., Wittenberg, A.T., Zeng, F., Zhang, R., 2012. Simulated climate and climate change in the GFDL CM2.5 high-resolution coupled climate model. J. Climate 25, 2755–2781.

Döös, K., Webb, D., 1994. The Deacon cell and the other meridional cells in the Southern Ocean. J. Phys. Oceanogr. 24, 429–442.

Downes, S.M., Budnick, A.S., Sarmiento, J.L., Farneti, R., 2011a. Impacts of wind stress on the antarctic circumpolar current fronts and associated subduction. Geophys. Res. Lett. 38 (L11605). doi:10.1029/2011GL047668.

Downes, S.M., Farneti, R., Uotila, P., Griffies, S.M., Marsland, S.J., Bailey, D., Behrens, E., Bentsen, M., Bi, D., Biastoch, A., Böning, C., Bozec, A., Canuto, V.M., Chassignet, E., Danabasoglu, G., Danilov, S., Diansky, N., Drange, H., Fogli, P.G., Gusev, A., Howard, A., Kelley, M., Ilicak, M., Jung, T., Kelley, M., Large, W.G., Leboissetier, A., Long, M., Lu, J., Masina, S., Mishra, A., Navarra, A., Nurser, A.J.G., Patara, L., Samuels, B.L., Sidorenko, D., Spence, P., Tsujino, H., Wang, Q., Yeager, S.G., 2015. An assesment of Southern Ocean water masses and sea ice during 1988–2007 in a suite of interannual CORE-II simulations. Ocean Model. in press.

Downes, S.M., Gnanadesikan, A., Griffies, S.M., Sarmiento, J.L., 2011b. Water mass exchange in the Southern Ocean in coupled climate models. J. Phys. Oceanogr. 41 (9), 1756–1771.

Downes, S.M., Hogg, A.M., 2013. Southern ocean circulation and eddy compensation in CMIP5 models. J. Climate 26 (18), 7198–7220.

Dufour, C.O., Sommer, J.L., Zika, J.D., Gehlen, M., Orr, J.C., Mathiot, P., Barnier, B., 2012. Standing and transient eddies in the response of the Southern Ocean meridional overturning to the Southern Annular Mode. J. Climate 25, 6958–6974.

Dunne, J.P., John, J.G., Adcroft, A.J., Griffies, S.M., Hallberg, R.W., Shevliakova, E., Stouffer, R.J., Cooke, W., Dunne, K.A., Harrison, M.J., Krasting, J.P., Malyshev, S.L., Milly, P.C.D., Phillips, P.J., Sentman, L.T., Samuels, B.L., Spelamn, M.J., Winton, M., Wittenberg, A.T., Zadeh, N., 2012. GFDL's ESM2 global coupled climate-carbon Earth System Models Part I: Physical formulation and baseline simulation characteristics. J. Climate 25, 6646–6665.

Eden, C., 2006. Thickness diffusivity in the southern ocean. Geophys. Res. Lett. 33 (11). doi:10.1029/2006GL026157.

Eden, C., Greatbatch, R., 2008. Towards a mesoscale eddy closure. Ocean Model. 20, 223–239.

Eden, C., Jochum, M., Danabasoglu, G., 2009. Effects of different closures for thickness diffusivity. Ocean Model. 26, 47–59.

Farneti, R., Delworth, T.L., Rosati, A.J., Griffies, S.M., Zeng, F., 2010. The role of mesoscale eddies in the rectification of the Southern Ocean response to climate change. J. Phys. Oceanogr. 40 (7), 1539–1557.

Farneti, R., Gent, P., 2011. The effects of the eddy-induced advection coefficient in a coarse-resolution coupled climate model. Ocean Model. 39 (1–2), 135–145.

Ferrari, R., Griffies, S.M., Nurser, A.J.G., Vallis, G.K., 2010. A boundary-value problem for the parameterized mesoscale eddy transport. Ocean Model. 32 (3–4), 143–156.

Ferrari, R., McWilliams, J.C., Canuto, V., Dubovikov, D., 2008. Parameterization of eddy fluxes at the ocean boundaries. J. Climate 31, 2770–2789.

Ferrari, R., Nikurashin, M., 2010. Suppression of eddy mixing across jets in the Southern Ocean. J. Phys. Oceanogr. 40, 1501–1519.

Ferreira, D., Marshall, J., Heimbach, P., 2005. Estimating eddy stresses by fitting dynamics to observations using a residual-mean ocean circulation model and its adjoint. J. Phys. Oceanogr. 35, 1891–1910.

Fox-Kemper, B., Danabasoglu, G., Ferrari, R., Griffies, S.M., Hallberg, R.W., Holland, M.M., Maltrud, M.E., Peacock, S., Samuels, B.L., 2011. Parameterization of mixed layer eddies. Part III: Implementation and impact in global ocean climate simulations. Ocean Model. 39, 61–78.

Fox-Kemper, B., Ferrari, R., Hallberg, R., 2008. Parameterization of mixed layer eddies. Part I: Theory and diagnosis. J. Phys. Oceanogr. 38, 1145–1165.

Frölicher, T.L., Sarmiento, J.L., Paynter, D.J., Dunne, J.P., Winton, M., 2015. Dominance of the Southern Ocean in anthropogenic carbon and heat uptake in CMIP5 models. J. Climate 28, 862–886.

Gent, P.R., Danabasoglu, G., 2011. Response to increasing Southern Hemisphere winds in CCSM4. J. Climate 24, 4992–4998.

Gent, P.R., Danabasoglu, G., Donner, L.J., Holland, M., Hunke, E.C., Jayne, S.R., Lawrence, D.M., Neale, R.B., Rasch, P.J., Vertenstein, M., Worley, P.H., Yang, Z.-L., Zhang, M., 2011. The Community Climate System Model version 4. J. Climate 24, 4973–4991.

Gent, P.R., McWilliams, J.C., 1990. Isopycnal mixing in ocean circulation models. J. Phys. Oceanogr. 20, 150–155.

Gent, P.R., Willebrand, J., McDougall, T.J., McWilliams, J.C., 1995. Parameterizing eddy-induced tracer transports in ocean circulation models. J. Phys. Oceanogr. 25, 463–474.

Gille, S.T., 2002. Warming of the Southern Ocean since the 1950s. Science 295, 1275–1277.

Gnanadesikan, A., Hallberg, R., 2000. On the relationship of the circumpolar current to Southern Hemisphere winds in coarse-resolution ocean models. J. Phys. Oceanogr. 30, 2013–2034.

Griesel, A., Mazloff, M.R., Gille, S.T., 2012. Mean dynamic topography in the Southern Ocean: evaluating Antarctic Circumpolar Current transport. J. Geophys. Res. 117 (C01020). doi:10.1029/2011JC007573.

Griffies, 1998. The Gent-McWilliams skew-flux. J. Phys. Oceanogr. 28, 831–841.

Griffies, S., Biastoch, A., Boning, C., Bryan, F., Danabasoglu, G., Chassignet, E., England, M., Gerdes, R., Haak, H., Hallberg, R., 2009. Coordinated ocean-ice reference experiments (COREs). Ocean Model. 26 (1–2), 1–46.

Griffies, S.M., 2007. Elements of MOM4p1, GFDL Ocean Group. Technical Report. No. 6, NOAA/Geophysical Fluid Dynamics Laboratory.

Griffies, S.M., 2012. Elements of the Modular Ocean Model (MOM) (2012 Release). GFDL Ocean Group Technical Report No. 7. NOAA/Geophysical Fluid Dynamics Laboratory, 618 + xiii pp.

Griffies, S.M., Gnanadesikan, A., Dixon, K.W., Dunne, J.P., Gerdes, R., Harrison, M.J., Rosati, A., Russell, J.L., Samuels, B.L., Spelman, M.J., Winton, M., Zhang, R., 2005. Formulation of an ocean model for global climate simulations. Ocean Sci. 1, 45–79.

Griffies, S.M., Gnanadesikan, A., Pacanowski, R.C., Larichev, V.D., Dukowicz, J.K., Smith, R.D., 1998. Isoneutral diffusion in a z-coordinate ocean model. J. Phys. Oceanogr. 28 (5), 805–830.

Griffies, S.M., Winton, M., Donner, L.J., Downes, S., Farneti, R., Gnanadesikan, A., Horowitz, L.W., Hurlin, W., Lee, H.-C., Palter, J.B., Samuels, B.L., Wittenberg, A., Wyman, B., Yin, J., 2011. GFDL's CM3 coupled climate model: characteristics of the ocean and sea ice simulations. J. Climate 24, 3520–3544.

Griffies, S.M., Yin, J., Durack, P.J., Goddard, P., Bates, S.C., Behrens, E., Bentsen, M., Bi, D., Biastoch, A., Böning, C., Bozec, A., Cassou, C., Chassignet, E., Danabasoglu, G., Danilov, S., Domingues, C., Drange, H., Farneti, R., Fernandez, E., Greatbatch, R.J., Holland, D.M., Ilicak, M., Lu, J., Marsland, S.J., Mishra, A., Lorbacher, K., Nurser, A.J.G., Salas y Mélia, D., Palter, J.B., Samuels, B.L., Schröter, J., Schwarzkopf, F.U., Sidorenko, D., Treguier, A.-M., Tseng, Y.-H., Tsujino, H., Uotila, P., Valcke, S., Voldoire, A., Wang, Q., Winton, M., Zhang, X., 2014. An assessment of global and regional sea level in a suite of interannual CORE-II simulations. Ocean Model. 78, 35–89.

Gusev, A.V., Diansky, N.A., 2014. Numerical simulation of the World ocean circulation and its climatic variability for 1948–2007 using the INMOM. Izv. Atmos. Ocean. Phys. 50 (1), 1–12.

Hallberg, R., Gnanadesikan, A., 2001. An exploration of the role of transient eddies in determining the transport of a zonally reentrant current. J. Phys. Oceanogr. 31, 3312–3330.

Hallberg, R., Gnanadesikan, A., 2006. The role of eddies in determining the structure and response of the wind-driven Southern Hemisphere overturning: results from the modeling eddies in the Southern Ocean (MESO) project. J. Phys. Oceanogr. 36, 2232–2252.

Halliwell, G.R., 2004. Evaluation of vertical coordinate and vertical mixing algorithms in the HYbrid-Coordinate Ocean Model. Ocean Model. 7, 285–322.

Heuzé, C., Heywood, K., Stevens, D., Ridley, J., 2013. Southern Ocean bottom water characteristics in CMIP5 models. Geophys. Res. Lett. 40, 1409–1414.

Hirabara, M., Tsujino, H., Nakano, H., Yamanaka, G., 2012. Formation mechanism of the weddel sea polynya and the impact on the global abyssal ocean. J. Oceanogr. 5, 771–796.

Hofmann, M., Maqueda, M.A.M., 2011. The response of Southern Ocean eddies to increased midlatitude westerlies: a non-eddy resolving model study. Geophys. Res. Lett. 38 (L03605). doi:10.1029/2010GL045972.

Hogg, A.M., 2010. An Antarctic Circumpolar Current driven by surface buoyancy forcing. Geophys. Res. Lett. 37 (23), L23601. doi:10.1029/2010GL044777.

Hughes, C.W., Meredith, M.P., Heywood, K.J., 1999. Wind-driven transport fluctuations through Drake Passage: a southern mode. J. Phys. Oceanogr. 29, 1971–1992.

IPCC, 2013. Climate Chane 2013: the physical science basis. In: Stocker, T.F., Qin, D., Plattner, G.-K., Tignor, M., Allen, S.K., Boschung, J., Nauels, A., Xia, Y., Bex, V., Midgley, P.M. (Eds.), Contribution of Working Group I to the fifth assessment report of the Intergovernmental Panel on Climate Change. Cambridge University Press, p. 1535pp.

Ito, T., Marshall, J., 2008. Control of lower-limb overturning circulation in the Southern Ocean by diapycnal mixing and mesoscale eddy transfer. J. Phys. Oceanogr. 38, 2832–2845.

Jansen, M.F., Held, I.M., 2014. Parameterizing subgrid-scale eddy effects using energetically consistent backscatter. Ocean Model. 80, 36–48.

Johns, W.E., Baringer, M.O., Beal, L.M., Cunningham, S.A., Kanzow, T., Bryden, H.L., Hirschi, J.J.M., Marotzke, J., Meinen, C.S., Shaw, B., Curry, R., 2011. Continuous, array-based estimates of Atlantic Ocean heat transport at 26.5 N. J. Climate 24, 2429–2449.

Jones, D.C., Ito, T., Lovenduski, N.S., 2011. The transient response of the Southern Ocean pycnocline to changing atmospheric winds. Geophys. Res. Lett. 38 (L15604). doi:10.1029/2011GL048145.

Koshlyakov, M.N., Lisina, I.I., Morozov, E.G., Tarakanov, R.Y., 2007. Absolute geostrophic currents in the Drake Passage based on observations in 2003 and 2005. Oceanology 47, 451–563.

Kuhlbrodt, T., Griesel, A., Montoya, M., Levermann, A., Hofmann, A., Rahmstorf, S., 2007. On the driving processes of the Atlantic meridional overturning circulation. Rev. Geophys. 45, RG2001. doi:10.1029/2004RG000166.

Kuhlbrodt, T., Smith, R.S., Wang, Z., Gregory, J.M., 2012. The influence of eddy parameterizations on the transport of the Antarctic Circumpolar Current in coupled climate models. Ocean Model. 52–53, 1–8.

Langlais, C.E., Rintoul, S.R., Zika, J.D., 2015. Sensitivity of Antarctic Circumpolar Current transport and eddy activity to wind patterns in the Southern Ocean. J. Phys. Oceanogr. 45, 1051–1067.

Large, W., Danabasoglu, G., Doney, S.C., McWilliams, J.C., 1997. Sensitivity to surface forcing and boundary layer mixing in a global ocean model: annual-mean climatology. J. Phys. Oceanogr. 27, 2418–2447.

Large, W.G., Yeager, S.G., 2009. The global climatology of an interannually varying air-sea flux data set. Climate Dyn. 33, 341–364.

Lee, M.-M., Coward, A., 2003. Eddy mass transport for the Southern Ocean in an eddy-permitting global ocean model. Ocean Model. 5, 249–266.

Liu, J., Schmidt, G.A., Martinson, D.G., Rind, D., Russell, G.L., Yuan, X., 2003. Sensitivity of sea ice to physical parameterizations in the GISS global climate model. J. Geophys. Res. 108 (C2). doi:10.1029/2001JC001167.

Madec, G., 2008. NEMO ocean engine. Technical Report 27, 1288-1619. Institute Pierre-Simon Laplace (IPSL).

Marshall, D.P., Adcroft, A., 2010. Parameterization of ocean eddies: vorticity mixing, energetics and Arnold's first stability theorem. Ocean Model. 32, 188–204.

Marshall, G.J., 2003a. Trends in the Southern Annular Mode from observations and re-analyses. J. Climate 16, 4134–4143.

Marshall, G.J., 2003b. Trends of the Southern Ocean CO$_2$ sink due to recent climate change. J. Climate 16, 1734–1738.

Marshall, J., Olbers, D., Ross, H., Wolf-Gladrow, D., 1993. Potential vorticity constraints on the dynamics and hydrography of the Southern Ocean. J. Phys. Oceanogr. 23, 465–487.

Marshall, J., Radko, T., 2003. Residual-mean solutions for the Antarctic Circumpolar Current and its associated overturnig circulation. J. Phys. Oceanogr. 33, 2341–2354.

Marshall, J., Radko, T., 2006. A model of the upper branch of the meridional overturning of the southern ocean. Progr. Oceanogr. 70, 331–345.

Marshall, J., Shuckburgh, E., Jones, H., Hill, C., 2006. Estimates and implications of surface eddy diffusivity in the Southern Ocean derived from tracer transport. J. Phys. Oceanogr. 36, 1806–1821.

Marshall, J., Speer, K., 2012. Closure of the meridional overturning circulation through Southern Ocean upwelling. Nat. Geosci. 5 (3), 171–180.

Marsland, S.J., Wolff, J.-O., 2001. On th sensitivity of Southern Ocean sea ice to the surface fresh water flux: a model study. J. Geophys. Res. 106.

Mazloff, M., Heimbach, P., Wunsch, C., 2010. An eddy-permitting Southern Ocean state estimates. J. Phys. Oceanogr. 40 (5), 880–899.

McDougall, T.J., McIntosh, P.C., 2001. The temporal residual-mean velocity. Part II: Isopycnal interpretation and the tracer and momentum equations. J. Phys. Oceanogr. 31, 1222–1246.

McIntosh, P., McDougall, T., 1996. Isopycnal averaging and the residual mean circulation. J. Phys. Oceanogr. 26, 1655–1660.

Meijers, A.J.S., Shuckburgh, E., Bruneau, N., Sallée, J.-B., Bracegirdle, T.J., Wang, Z., 2012. Representation of the Antarctic Circumpolar Current in the CMIP5 climate models and future changes under warming scenarios. J. Geophys. Res. 117 (C12008). doi:10.1029/2012JC008412.

Meredith, M.P., Hogg, A.M., 2006. Circumpolar responses of the Southern Ocean eddy activity to a change in the Southern Annular Mode. Geophys. Res. Lett. 33, L16608. doi:10.1029/2006GL026499.

Meredith, M.P., Naveira-Garabato, A.C., Hogg, A.M., Farneti, R., 2012. Sensitivity of the overturning circulation in the Southern Ocean to decadal changes in wind forcing. J. Climate 25, 99–110.

Morrison, A.K., Hogg, A.M., 2013. On the relationship between Southern Ocean overturning and ACC transport. J. Phys. Oceanogr. 43, 140–148.

Morrison, A.K., Hogg, A.M., Ward, M.L., 2011. Sensitivity of the Southern Ocean overturning circulation to surface buoyancy forcing. Geophys. Res. Lett. 38 (14). doi:10.1029/2011GL048031.

Munday, D.R., Johnson, H.L., Marshall, D.P., 2013. Eddy saturation of equilibrated circumpolar currents. J. Phys. Oceanogr. 43 (3), 507–532.

Naveira Garabato, A.C., Ferrari, R., Polzin, K., 2011. Eddy stirring in the Southern Ocean. J. Geophys. Res. 116.C09019. doi: 10.1029/2010JC006818.

Olbers, D., Borowski, D., Völker, C., J.-O.Wölff, 2004. The dynamical balance, transport and circulation of the Antarctic Circumpolar Current. Ant. Sci. 16 (4), 439–470.

Olbers, D., Visbeck, M., 2005. A model of the zonally averaged stratification and overturning in the Southern Ocean. J. Phys. Oceanogr. 35 (7), 1190–1205.

Redi, M.H., 1982. Oceanic isopycnal mixing by coordinate rotation. J. Phys. Oceanogr. 12, 1154–1158.

Renault, A., Provost, C., Sennechael, N., Barré, N., Kartavtseff, A., 2011. Two full-depth velocity sections in the Drake Passage in 2006—transport estimates. Deep-Sea Res. 58, 2572–2591.

Rintoul, S.R., Naveira-Garabato, A.C., 2013. Dynamics of the Southern Ocean circulation. In: Siedler, G., Griffies, S.M., Gould, J., Church, J.A. (Eds.), Ocean Circulation and Climate: A 21st Century Perspective, 103. International Geophysical Series, Academic Press, pp. 471–492.

Russell, J.L., Dixon, K.W., Gnanadesikan, A., Stouffer, R.J., Toggweiler, J.R., 2006. The Southern Hemisphere westerlies in a warming world: propping open the door to the deep ocean. J. Climate 19 (24), 6382–6390.

Saenko, O.A., Gupta, A.S., Spence, P., 2012. On challenges in predicting bottom water transport in the Southern Ocean. J. Climate 25, 1349–1356.

Sallée, J.-B., Shuckburgh, E., Bruneau, N., Meijers, A.J.S., Bracegirdle, T.J., Wang, Z., Roy, T., 2013. Assessment of Southern Ocean water masses circulation and characteristics in CMIP5 models: historical bias and forcing response. J. Geophys. Res. 118 (4), 1830–1844.

Sallée, J.-B., Speer, K., Morrow, R., Lumpkin, R., 2008. An estimate of lagrangian eddy statistics and diffusion in the mixed layer of the Southern Ocean. J. Mar. Res. 66 (4), 441–463.

Sen Gupta, A., England, M.H., 2006. Coupled ocean–atmosphere–ice response to variations in the Southern Annular Mode. J. Climate 19 (18), 4457–4486.

Sen Gupta, A., Santoso, A., Taschetto, A.S., Ummenhofer, C.C., Trevena, J., England, M.H., 2009. Projected changes to the Southern Hemisphere ocean and sea ice in the IPCC AR4 climate models. J. Climate 22, 3047–3078.

Sidorenko, D., Rackow, T., Jung, T., Semmler, T., Barbi, D., Danilov, S., Dethloff, K., Dorn, W., Fieg, K., Gössling, H.F., Handorf, D., Harig, S., Hiller, W., Juricke, S., Losch, M., Schröter, J., Sein, D., Wang, Q., 2015. Towards multi-resolution global climate modeling with ECHAM6-FESOM. Part I: Model formulation and mean climate. Climate Dyn. 44 (3-4), 757–780.

Sijp, W.P., England, M.H., 2004. Effect of the Drake Passage throughflow on global climate. J. Phys. Oceanogr. 34, 1254–1266.

Sloyan, B.M., Rintoul, S.R., 2001. The Southern Ocean limb of the global deep overturning. J. Phys. Oceanogr. 31, 143–172.

Smith, R. D., Jones, P., Briegleb, B., Bryan, F., Danabasoglu, G., Dennis, J., Dukowicz, J., Eden, C., Fox-Kemper, B., Gent, P., Hecht, M., Jayne, S., Jochum, M., Large, W., Lindsay, K., Maltrud, M., Norton, N., Peacock, S., Vertenstein, M., Yeager, S., 2010. The Parallel Ocean Program reference manual, ocean component of the Community Climate System Model (CCSM): Los Alamos National Laboratory Tech. Rep. LAUR-10-01853. Los Alamos, NM.

Speer, K., Rintoul, S.R., Sloyan, B., 2000. The diabatic Deacon cell. J. Phys. Oceanogr. 30, 3212–3222.

Straub, D.N., 1993. On the transport and angular momentum balance of channel models of the Antarctic Circumpolar Current. J. Phys. Oceanogr. 23, 776–782.

Talley, L., 2008. Freshwater transport estimates and the global overturning circulation: shallow, deep and throughflow components. Progr. Oceanogr. 78, 257–303.

Thompson, D.W.J., Solomon, S., Kushner, P.J., an K. M. Grise, M.H.E., Karoly, D.J., 2011. Signatures of the Antarctic ozone hole in the Southern Hemisphere surface climate change. Nat. Geosci. 4, 741–749.

Thompson, D.W.L., Solomon, S., 2002. Interpretation of recent Southern Hemisphere climate change. Science 296, 895–899.

Toggweiler, J.R., Russell, J., 2008. Ocean circulation in a warming climate. Nature 451 (7176), 286–288.

Toggweiler, J.R., Russell, J.L., Carson, S.R., 2006. Midlatitude westerlies, atmospheric CO$_2$, and climate change during the ice ages. Paleoceanography 21 (2). doi:10.1029/2005PA001154.

Toggweiler, J.R., Samuels, B., 1995. Effect of Drake Passage on the global thermohaline circulation. Deep-Sea Res. 42, 477–500.

Treguier, A.M., England, M.H., Rintoul, S.R., Madec, G., Sommer, J.L., Molines, J.-M., 2007. Southern Ocean overturning across streamlines in an eddying simulation of the Antarctic Circumpolar Current. Ocean Sci. 3, 491–507.

Treguier, A.M., Held, I.M., Larichev, V.D., 1997. Parameterization of quasigeostrophic eddies in primitive equation ocean models. J. Phys. Oceanogr. 27 (4), 567–580.

Treguier, A.M., Sommer, J.L., Molines, J.M., de Cuevas, B., 2010. Response of the Southern Ocean to the Southern Annular Mode: interannual variability and multidecadal trend. J. Phys. Oceanogr. 40, 1659–1668.

Tsujino, H., Hirabara, M., Nakano, H., Yasuda, T., Motoi, T., Yamanaka, G., 2011. Simulating present climate of the global ocean-ice system using the Meteorological Research Institute Community Ocean Model (MRI.COM): simulation characteristics and variability in the Pacific sector. J. Oceanogr. 67, 449–479.

Viebahn, J., Eden, C., 2010. Towards the impact of eddies on the response of the Southern Ocean to climate change. Ocean Model. 34, 150–165.

Viebahn, J., Eden, C., 2012. Standing eddies in the meridional overturning circulation. J. Phys. Oceanogr. 42, 1486–1508.

Visbeck, M., 2009. A station-based Southern Annular Mode index from 1884 to 2005. J. Climate 22, 940–950.

Volkov, D.L., Fu, L.-L., Lee, T., 2010. Mechanisms of the meridional heat transport in the Southern Ocean. Ocean Dyn. 60, 791–801.

Volodin, E.M., Dianskii, N.A., Gusev, A.V., 2010. Simulating present-day climate with the INMCM4.0 coupled model of the atmospheric and oceanic general circulations. Izv. Atmos. Ocean. Phys. 46, 414–431.

Wang, Q., Danilov, S., Sidorenko, D., Timmermann, R., Wekerle, C., Wang, X., Jung, T., Schröter, J., 2014. The Finite Element Sea Ice-Ocean Model (FESOM) v.1.4: formulation of an ocean general circulation model. Geosci. Model Dev. 7 (2), 663–693.

Wang, Z., Kuhlbrodt, T., Meredith, M.P., 2011. On the response of the Antarctic Circumpolar Current transport to climate change in coupled climate models. J. Geophys. Res. 116 (C08011). doi:10.1029/2010JC006757.

Watson, A.J., Naveira-Garabato, A.C., 2006. The role of Southern Ocean mixing and upwelling in glacial-interglacial atmospheric CO$_2$ change. Tellus B 58, 73–87.

Yang, X.Y., Wang, D., Wang, J., Huang, R.X., 2007. Connection between the decadal variability in the Southern Ocean circulation anf the Southern Annular Mode. Geophys. Res. Lett. 34 (L16604). doi:10.1029/2007GL030526.

Yeager, S., Danabasoglu, G., 2014. The origins of late twentieth century variations in the large-scale North Atlantic circulation. J. Climate 27, 3222–3247.

Yukimoto, S., Adachi, Y., Hosaka, M., Sakami, T., Yoshimura, H., Hirabara, M., Tanaka, T.Y., Shindo, E., Tsujino, H., Deushi, M., Mizuta, R., Yabu, S., Obata, A., Nakano, H., Koshiro, T., Ose, T., Kitoh, A., 2012. A new gobal climate model of Meteorological Research Institute: MRI-CGCM3—model description and basic performance. J. Meteor. Soc. Jpn. 90A, 23–64.

Zika, J.D., Le Sommer, J., Dufour, C.O., Molines, J.-M., Barnier, B., Brasseur, P., Dussin, R., Penduff, T., Iudicone, D., Lenton, A., Madec, G., Mathiot, P., Orr, J., Shuckburgh, E., Vivier, F., 2013a. Vertical eddy fluxes in the Southern Ocean. J. Phys. Oceanogr. 43 (5), 941–955.

Zika, J.D., Sommer, J.L., Dufour, C.O., Naveira-Garabato, A.C., Blaker, A., 2013b. Acceleration of the Antarctic Circumpolar Current by wind stress along the coast of Antarctica. J. Phys. Oceanogr. 43, 2772–2784.